DISSERTATIONES
CHIMICAE
UNIVERSITATIS
TARTUENSIS
241

GULNARA YUSIBOVA

TAL MOF-Derived M-N-C Electrocatalysts for Oxygen Reduction and Evolution Reactions

DISSERTATIONES CHIMICAE UNIVERSITATIS TARTUENSIS
241

DISSERTATIONES CHIMICAE UNIVERSITATIS TARTUENSIS
241

GULNARA YUSIBOVA

TAL MOF-Derived M-N-C Electrocatalysts for Oxygen Reduction and Evolution Reactions

UNIVERSITY OF TARTU
Press
1632

Institute of Chemistry, Faculty of Science and Technology, University of Tartu, Estonia.

The dissertation is accepted for the commencement of the degree of *Doctor Philosophiae* in Chemistry on June 10, 2025 by the Council of Institute of Chemistry, Faculty of Science and Technology, University of Tartu.

Doctoral advisors:	Assoc. Prof. Nadezda Kongi Prof. Kaido Tammeveski Institute of Chemistry, University of Tartu
Opponent:	Assoc. Prof. Annukka Santasalo-Aarnio, Department of Mechanical Engineering School of Engineering, Aalto University, Finland
Commencement:	August 28, 2025 at 13:15 Ravila 14A-1020, Tartu (Chemicum) and Microsoft Teams (*online*)

This work has been partially supported by ASTRA project PER ASPERA Graduate School of Functional Materials and Technologies receiving funding from the European Regional Development Fund under project in University of Tartu, Estonia

ISSN 1406-0299 (print)
ISBN 978-9916-27-938-0 (print)
ISSN 2806-2159 (pdf)
ISBN 978-9916-27-939-7 (pdf)

University of Tartu Press
www.tyk.ee

TABLE OF CONTENTS

1. LIST OF ORIGINAL PUBLICATIONS

This thesis consists of three original articles listed below. The articles are referred to in the text by Roman numerals I–III.

I. **G. Yusibova**, K. Ping, M. Käärik, J. Leis, J. Aruväli, K. Šmits, T. Käämbre, V. Kisand, Y. Karpichev, K. Tammeveski, N. Kongi, Optimizing post-treatment strategies for enhanced oxygen reduction/evolution activity in Co–N–C electrocatalyst, *International Journal of Hydrogen Energy* 82 (2024) 398–406. https://doi.org/10.1016/j.ijhydene.2024.07.388.

II. **G. Yusibova**, J.-M. Assafrei, K. Ping, J. Aruväli, P. Paiste, M. Käärik, J. Leis, H.-M. Piirsoo, A. Tamm, A. Kikas, V. Kisand, P. Starkov, N. Kongi, Bimetallic metal-organic-framework-derived porous cobalt manganese oxide bifunctional oxygen electrocatalyst, *Journal of Electroanalytical Chemistry* 930 (2023) 117161. https://doi.org/10.1016/j.jelechem.2023.117161.

III. **G. Yusibova**, J.C. Douglin, I. Vetik, J. Pozdnjakova, K. Ping, J. Aruväli, A. Kikas, V. Kisand, M. Käärik, J. Leis, T. Kaljuvee, P. Paaver, S. Oras, Ł. Ciupiński, T. Plocinski, M. Konuhova, A.I. Popov, D.R. Dekel, V. Ivaništšev, N. Kongi, Pyrolytic Transformation of Zn-TAL Metal–Organic Framework into Hollow Zn–N–C Spheres for Improved Oxygen Reduction Reaction Catalysis, *ACS Omega* 10 (2025) 15280–15291. https://doi.org/10.1021/acsomega.4c11318.

Author's contribution

Article I The author was responsible for doing electrochemical experiments. The author was responsible for the interpretation of all testing results and data analysis and was primarily responsible for writing the manuscript.

Article II The author was responsible for doing electrochemical experiments. The author was responsible for the interpretation of all testing results and data analysis and was primarily responsible for writing the manuscript.

Article III The author was responsible for doing electrochemical experiments. The author was responsible for the interpretation of all testing results and data analysis and was primarily responsible for writing the manuscript.

2. ABBREVIATIONS AND SYMBOLS

AEM	adsorbate evolution mechanism
AEMFC	anion exchange membrane fuel cell
APS	average pore size
BET	Brunauer-Emmett-Teller
C_{dl}	double-layer capacitance
C_{sp}	specific capacity
CV	cyclic voltammetry
E^0	standard potential
$E_{1/2}$	half-wave potential
ΔE	potential gap
EDX	energy-dispersive X-ray spectroscopy
EES	electrochemical energy storage
$E_{j=10}$	potential at 10 mA cm^{-2}
E_{on}	onset potential
ESCA	electrochemically accessible surface area
FC	fuel cell
GC	glassy carbon
HAADF	high-angle annular dark field
j	current density
j_k	kinetic current density
j_d	diffusion-limited current density
K-L	Koutecky-Levich
LOM	lattice oxygen-mediated mechanism
LSV	linear sweep voltammetry
MAB	metal-air battery
M-N-C	metal-nitrogen-carbon
M-N_x	metal-coordinated to nitrogen
MOF	metal-organic framework
MP-AES	microwave plasma atomic emission spectroscopy
n	number of electrons transferred per O_2 molecule
η	overpotential
OCV	open circuit voltage
OER	oxygen evolution reaction
ORR	oxygen reduction reaction
PEM	proton exchange membrane
PGMs	platinum-group metals
P_{max}	peak power density
PSD	pore size distribution
PXRD	powder X-ray diffraction
RDE	rotating disk electrode
RHE	reversible hydrogen electrode
S_{BET}	BET surface area

S_{dft}	specific surface area
SEM	scanning electron microscopy
SHE	standard hydrogen electrode
s-NMR	solid-state nuclear magnetic resonance
STEM	scanning transmission electron microscopy
TAL	TalTech–UniTartu Alliance Laboratory
TGA	thermogravimetric analysis
TGA-DTA	thermogravimetric – differential thermal analysis
V_{μ}	micropore volume
V_{meso}	mesopore volume
V_{tot}	total pore volume
XPS	X-ray photoelectron spectroscopy
ZAB	zinc-air battery
ZIF	zeolitic imidazolate framework

3. INTRODUCTION

The development of renewable energy storage and conversion technologies has become increasingly important because of their environmental impact, the depletion of fossil fuels, and rising energy costs. According to the International Energy Agency, global energy consumption is growing by about 1% annually [1,2], with the transportation area appear as the largest consumer. Despite this, fossil fuels still dominate transportation energy use. Since renewables like solar and wind are intermittent, efficient energy storage systems are essential [3].

Fuel cells (FCs) and metal-air batteries (MABs) are leading alternatives due to their high efficiency and sustainability [4,5]. Storing excess renewable energy using hydrogen (H_2) as an energy carrier, later converted into electricity by FCs, is a promising approach. FCs also benefit from quick refueling compared to traditional batteries. Anion-exchange membrane fuel cells (AEMFCs) are especially attractive because of their ability to use non-precious metal catalysts, reducing costs compared to proton-exchange membrane counterparts that require platinum as a catalyst [4,6,7].

Zinc-air batteries (ZABs) offer high energy density (1086 Wh kg^{-1}), low cost, as well as improved safety over lithium-ion batteries [8]. Critical to FCs and ZABs are the oxygen reduction reaction (ORR) and oxygen evolution reaction (OER) [9], due to their slow kinetics and high overpotentials, which decreases efficiency [10,11]. While platinum-group metal (PGM) catalysts enhance these reactions [12,13], their high cost and limited availability pose challenges for widespread use.

Transition metal-nitrogen-carbon (M-N-C) materials are widely used as oxygen electrocatalysts due to their porous structure, high electrical conductivity and electrocatalytic activity [14,15]. High-performance M-N-C catalysts exhibit well-dispersed single-atom sites, various nitrogen moieties, and high specific surface area [10,16,17]. They are typically synthesized via pyrolysis of transition metal, nitrogen, and carbon precursors, followed by heat-treatment and acid leaching to enhance active site exposure and improve mass transport [8,18,19]. The M-N_x sites within the carbon matrix are considered as active sites for ORR, with the carbon aiding high surface area and electron transfer during ORR and OER [14,20,21]. Metal-organic frameworks (MOFs), with their tunable structure and high nitrogen content, serve as effective precursors for M-N-C catalysts [22–24].

In this work, we focus on a novel class of MOFs developed within our research group, known as TAL, which stands for TalTech–UniTartu Alliance Laboratory. These materials were specifically designed to serve as tunable and multifunctional precursors for the preparation of electrocatalysts. The TAL series of MOFs incorporate different metal centers and organic linkers, enabling precise control over their structural, electronic, and porosity characteristics. This thesis systematically investigates the synthesis routes, compositional variations, and post-synthetic modification strategies applied to TAL MOFs, with the goal of understanding how these parameters influence their transformation into active M-

N-C electrocatalysts. Special emphasis is placed on evaluating the electrocatalytic performance of TAL-derived catalyst materials in ORR and OER. We explore the impact of different metal centers (e.g., Co, Mn, Zn) and their combinations on the structure-activity relationship, and assess how pyrolysis temperature and post-synthetic treatment conditions affect the final catalyst morphology, porosity, and active site distribution. This work demonstrates that TAL MOFs provide a robust and versatile platform for designing high-performance, PGM-free electrocatalysts. Through careful optimization of synthesis and post-treatment conditions, several TAL-derived catalysts were found to exhibit competitive electrocatalytic activity and stability compared to commercial benchmarks. By integrating various physicochemical and electrochemical characterization techniques, this study provides insights into the structural evolution of TAL MOFs during pyrolysis and the mechanisms that drive their electrocatalytic behavior.

4. LITERATURE OVERVIEW

4.1 Clean energy technologies

The main issue of the modern world is how to meet the quickly rising global energy demands in a manner that is environmentally sustainable. As populations grow and economies develop, the global demand for energy continues to increase, putting lots of pressure on the existing energy technologies. Conventionally, this demand has been met mainly through the usage of fossil fuels such as oil, natural gas, and coal. Although these resources have played an important role in advancing industrialization and improving quality of life, their extraction and combustion have led to severe environmental consequences [25]. These include greenhouse gas emissions, air and water pollution, and ecological degradation, all of which contribute to climate change and public health risks.

There is a clear and urgent need to shift the global energy paradigm away from fossil fuels toward more sustainable and clean energy alternatives. Transitioning to renewable power sources such as hydropower, wind, and solar is essential to reduce our environmental footprint, while supporting long-term economic growth. One of the most promising approaches within this transition is the development of hydrogen-based energy systems. Hydrogen energy technologies, particularly hydrogen fuel cells and water electrolyzers, offer a clean and efficient way to generate power, as their only by-product is water [26]. These systems have the potential to play an important role in decarbonizing sectors such as industry, power generation, and transportation.

Together with hydrogen FCs, clean electrochemical energy storage technologies like metal-air batteries are also gaining attention. MABs rely on metal oxidation reactions with oxygen from the air and can offer high energy densities and long runtimes, making them suitable for grid storage and electric vehicles. FCs and MABs are promising in the pursuit of a sustainable energy future.

4.2 Oxygen electrocatalysis

The electrochemical reduction of oxygen is a vital reaction with broad importance [27]. In addition to its central role in energy production through zinc–air batteries and fuel cells, it also supports biological respiration, which is essential for life. Under alkaline conditions, the ORR can proceed via two different pathways. One of these is the direct 4-electron pathway [27]:

$$O_2 + 2H_2O + 4e^- \rightarrow 4OH^- \qquad E_0 = 0.401\ \text{V} \qquad (1)$$

or 2-electron pathway:

$$O_2 + H_2O + 2e^- \rightarrow HO_2^- + OH^- \qquad E_0 = -0.065\ \text{V} \qquad (2)$$

$$HO_2^- + H_2O + 2e^- \rightarrow 3OH^- \qquad E_0 = 0.867\ \text{V}, \qquad (3)$$

where all standard potential (E_0) values are referenced to the standard hydrogen electrode (SHE) at 25 °C.

The ORR is a key process in fuel cells, occurring at the cathode where oxygen reacts with protons and electrons to generate water (H_2O) [28]. The ORR efficiency greatly affects fuel cell performance, as faster kinetics help to maintain high voltage output [10]. However, sluggish ORR kinetics and the formation of hydroperoxide (HO_2^-) anions can cause voltage losses and reduce efficiency [29].

In alkaline media, adsorbed OH^- ions hinder O_2 chemisorption [30], often leading to an outer-sphere pathway where O_2 is reduced to superoxide (O_2^-) anion [31]. This allows for greater flexibility in catalyst design, enabling broader use of non-PGMs in alkaline systems compared to acidic ones [32,33]. Improving the ORR electrocatalytic activity remains essential for advancing fuel cell technologies toward cleaner and more sustainable applications.

The oxygen evolution reaction (OER) typically follows two pathways: the adsorbate evolution mechanism (AEM) and the lattice oxygen-mediated mechanism (LOM) [33], as shown in Figure 1a and b. In the AEM, the process starts with the adsorption of a water molecule onto a metal (M) site, forming OH^* through a one-electron oxidation [34]. This OH^* then undergoes proton-electron transfer to form O^*. Next, an O-O bond forms, producing HOO^*, which is oxidized in the final step, releasing O_2 and regenerating the metal site [33].

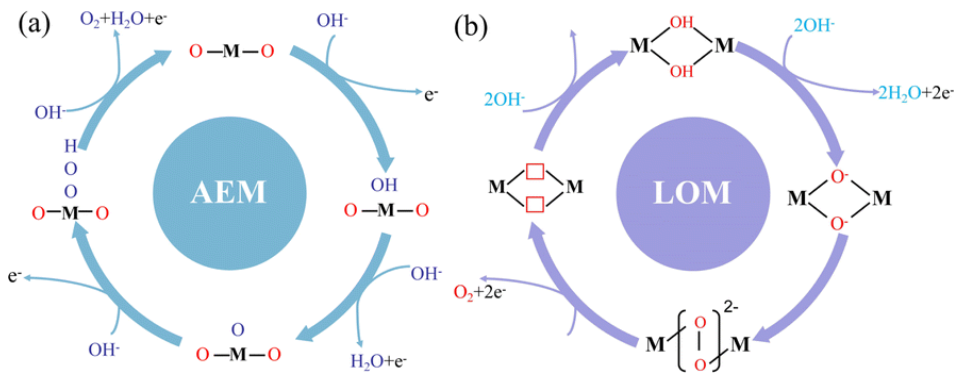

Figure 1. Oxygen evolution reaction mechanisms: (a) conventional adsorbate evolution mechanism, (b) lattice oxygen release mechanism [35].

The scaling relations of intermediates in the adsorbate evolution mechanism limits OER, with a theoretical overpotential of 0.37 V [33]. In contrast, the lattice-oxygen-mediated mechanism, where lattice oxygen participates directly, was first proposed by Damjanovic and Jovanovic in 1976 [36] and later expanded by Binninger et al. in 2015 [37]. In this pathway, O^* interacts with lattice oxygen to release O_2, creating an oxygen vacancy, which is refilled by OH^- ions from the solution. This mechanism avoids the scaling limitation seen in the adsorbate evolution pathway, as HOO^* does not form [37].

4.3 Fuel cells

A fuel cell is a device that directly converts the chemical energy stored in fuel into electrical energy. Various types of fuel cells exist, with particular emphasis on the H_2/O_2-fed FC due to its advantages, including low operating temperature and a high energy-to-weight ratio [38]. Among hydrogen fuel cells, the proton exchange membrane fuel cell (PEMFC) has been highly investigated for decades and is generally preferred over the AEMFC [39]. At present, PEMFC technology is well established, whereas AEMFCs still require further advancements [40–42]. The superior diffusivity of protons (H^+) compared to hydroxide ions (OH^-) grants PEMFCs an edge in achieving higher ionic conductivity [38]. However, despite utilizing noble metal-based catalysts, PEMFCs face durability challenges due to their acidic environment [43].

Conversely, AEMFCs function in an alkaline medium, which allows for the use of lower cost, non-noble metal and also metal-free catalysts [4,9]. Research has shown that catalyst deactivation, especially due to hydrogen peroxide (H_2O_2) formation, is more significant in acidic conditions than in alkaline ones [44]. Additionally, unlike proton exchange membranes (PEMs), anion exchange membranes can be prepared without relying on expensive and hazardous fluorinated compounds [45]. The ORR also benefits from more favorable electrochemical kinetics in alkaline conditions, reducing the necessity for high catalyst loading [46]. Also, the less corrosive nature of alkaline environments broadens the range of viable non-noble metal electrocatalysts [47,48]. These combined benefits position AEMFCs as an attractive alternative for different energy applications, offering an inexpensive, efficient, and green solution in the fuel cell technology [4,10,38,45].

In an AEMFC, hydrogen (H_2) is introduced at the anode, while oxygen (O_2) is supplied at the cathode. A schematic illustration of an AEMFC is shown in Figure 2. Electrochemical reactions take place at the triple-phase boundaries in fuel cells. In the presence of water, oxygen at the cathode undergoes reduction, generating hydroxide ions (OH^-), which migrate through the membrane to the anode, where they react with hydrogen to form water. This process results in water consumption at the cathode while simultaneously producing water at the anode. Consequently, effective water management is essential to prevent cathode dehydration and anode flooding [49].

During the redox reaction, electrons produced at the anode are collected by current collectors and transported to the cathode through external circuits. The membrane is specifically designed to facilitate the selective transport of OH^- ions. Although AEMFCs are now growing in popularity and hold promise for commercialization, this was not the case just a few years ago, as their performance was considerably inferior to that of PEMFCs. The significant enhancement in AEMFC performance can be attributed to several key factors: (i) the development of improved anion exchange membranes, (ii) modifications in operational strategies, and (iii) advancements in catalyst materials [50].

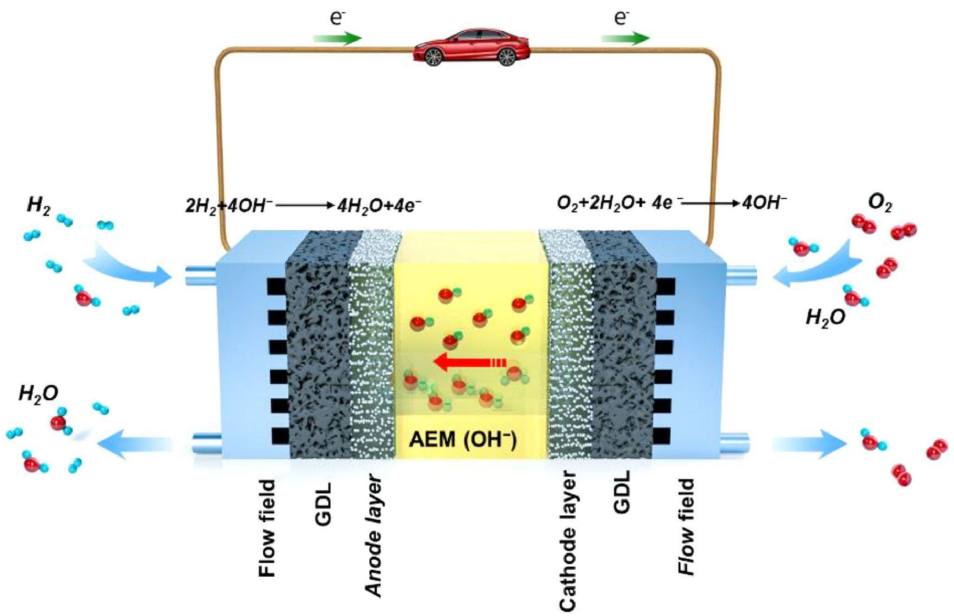

Figure 2. Diagram of the AEMFC along with a depiction of water movement [42].

4.4 Zinc-air batteries

Since the 19th century, metal-air batteries have seen significant advancements [51]. The Zn-air battery (ZAB) was commercialized soon after carbon-based gas diffusion electrodes were introduced [52], initially for hearing aids and later for energy storage applications [53]. Despite extensive research, ZABs still encounter low power density, limited stability, and low discharge voltage plateaus because of high overpotential at the air electrode, caused by sluggish ORR and OER kinetics [54]. Developing a low-cost bifunctional ORR/OER catalyst is important to improving ZAB performance [11], demanding active sites for both reactions. OER is constrained by HOO^* and O^* formation, while ORR is limited by OH^* and O_2 reduction steps [32].

Structurally, ZABs consist of an anode, electrolyte, and cathode (Figure 3). During discharge, O_2 diffuses to the cathode, at which proceeds the ORR (Eq. 4) generating OH^-. When charging, OER occurs (Eq. 5), supplying electrons for Zn^{2+} reduction. At the anode, Zn reacts with OH^-, forming zincate ions ($Zn(OH)_4^{2-}$) and releasing electrons (Eq. 6). $Zn(OH)_4^{2-}$ then decomposes into ZnO (Eq. 7), which is reduced back to Zn during charging (reverse of Eq. 8). Ion transport is facilitated by the electrolyte, while the ORR and OER kinetics at the cathode determine the ZAB efficiency and stability. Due to slow reaction kinetics, highly active and durable bifunctional electrocatalysts are essential to enhance performance, stability, and recyclability [55].

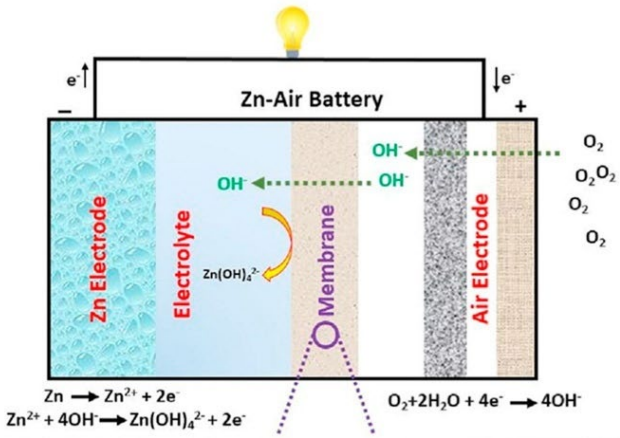

Figure 3. Schematic diagram of ZAB [56].

Cathode discharge:

$$O_2 + 2H_2O + 4e^- \rightarrow 4OH^- \quad (4)$$

Cathode charge:

$$4OH^- \rightarrow O_2 + 2H_2O + 4e^- \quad (5)$$

Anode:

$$Zn + 4OH^- \rightarrow Zn(OH)_4^{2-} + 2e^- \quad (6)$$

$$Zn(OH)_4^{2-} \rightarrow ZnO + H_2O + 2OH^- \quad (7)$$

Overall: $2Zn + O_2 \rightarrow 2ZnO$ (8)

In ZABs, Zn dendrite formation, cathode flooding, and electrolyte evaporation are key issues, but the primary challenge is the sluggish ORR and OER kinetics, affecting the ZAB efficiency and stability [57]. Understanding their pathways is crucial, as the ORR in alkaline conditions follows two distinct pathways [58].

4.5 Bifunctional M-N-C electrocatalysts for ZABs

Currently, state-of-the-art catalysts mainly rely on PGMs for high ORR and OER activity [59]. While effective, PGMs face challenges due to high cost, scarcity, and limited durability, restricting their large-scale use in energy storage and conversion systems. As alternatives, non-PGM catalysts have gained significant attention [60]. Among them, transition metal-nitrogen-doped carbon catalysts appear as distinctive, offering comparable ORR/OER performance and high electrochemical stability [61,62]. They are also more affordable, using abundant metal, nitrogen, and carbon sources [63] This versatility enables tailored design through careful selection of precursors, optimized synthesis method, and post-treatment to enhance performance [63].

The ORR activity of M-N-C catalysts originates from the synergy of different active sites, mainly (i) nitrogen-coordinated transition metal ($M\text{-}N_x$) centers [48,64,65] and (ii) nitrogen functional groups like pyridinic-N and pyrrolic-N [66,67]. $M\text{-}N_x$ sites enhance O–O bond cleavage through metal centers interacting with O_2's π^*-orbitals via empty dz^2 orbitals [68], with electrocatalytic activity following $Fe^{2+} > Co^{2+} > Mn^{2+} > Cu^{2+}$ [69].

4.6 M-N-C electrocatalysts for AEMFC

The ORR in alkaline media is more complex than in acidic conditions due to both inner- and outer-sphere electron transfer reactions [31]. However, this complexity allows a wider range of non-precious metal catalysts to effectively catalyze the ORR. M-N-C catalysts (M = Fe, Co, Mn, Cu) have demonstrated superior ORR activity in alkaline environments compared to acidic ones [9,70].

The peak power density (P_{max}) of AEMFCs using Fe-N-C cathode catalysts has significantly improved, increasing from 0.107 W cm^{-2} in 2015 to 1.44 W cm^{-2} in 2020 [4,71]. Ren et al. found that altering Fe-N-C cathode layer thickness affects P_{max}, ranging from 0.287 to 0.450 W cm^{-2} as catalyst loading increased from 1 to 2 mg cm^{-2}, respectively [72]. Khan et al. developed Cr and Mn-based catalysts, achieving a P_{max} of 309 mW cm^{-2} and a current density of 610 mA cm^{-2} in AEMFCs [73]. Lilloja et al. synthesized a CoFe-N-CDC/CNT catalyst, which reached an impressive P_{max} of 1120 mW cm^{-2} [74]. Woo et al. used a silica coating-mediated approach to create Fe and N co-doped carbon catalysts, with the Fe-S-Phen-CNT catalyst attaining a P_{max} of 635 mW cm^{-2} [75].

No single transition metal-based catalyst stands out as the best for AEMFCs; however, several bimetallic catalysts have demonstrated impressive fuel cell performance. It is important to consider that, in addition to choosing the anion exchange membrane, factors such as the preparation of the membrane-electrode assembly and different test conditions, like gas flow rates, backpressure, gas humidity, and fuel cell temperature, have a significant impact on the AEMFC performance [76].

4.7 MOF-derived M-N-C electrocatalysts

Various innovative methods for designing highly dispersed active site catalysts for bifunctional applications have been explored. Among these, MOF-derived M-N-C catalysts offer tunable functionalities, diverse morphologies, and promising chemical and mechanical stabilities [77–79]. MOFs serve as precursors for M-N-C catalysts, allowing for tailored pore structure and providing a higher density of active sites and improved mass transfer [80–82]. Recent simulations and experiments offer that introducing a secondary transition metal can improve bifunctional electrocatalytic performance by modifying the coordination environment of active centers on the catalyst surface [83–85]. However, achieving precise control over synthesis remains challenging due to complex chemical and morphological changes during MOF pyrolysis [15]. Latest investigations have begun exploring the relationship between pyrolysis temperature and catalyst properties. Huang et al. studied the evolution of ZIF-8 and ZIF-67 into catalyst materials, finding that metallic particle formation impacted active site density and electrocatalytic performance [86]. Xia et al. noted that carbon materials derived from ZIFs at high temperatures (≥900 °C) can retain significant Zn-N_x moieties [87]. Further research is needed to improve control and consistency in catalyst performance [63,88,89].

Compared to iron and cobalt, manganese-based electrocatalysts show lower ORR and OER activity [90], but manganese aids in the graphitization of carbon-based catalysts, enhancing stability and corrosion resistance [91–93], and it also alters dioxygen adsorption kinetics [94]. Manganese has several advantages, including low toxicity, environmental friendliness, low cost, and high abundance in natural ores [91,95]. To improve the ORR/OER kinetics on manganese, second transition metals can be used for doping or co-doping M-N-C catalysts [96–98]. Recently, Chen et al. showed that intercalating Co ions into the interlayer of d-MnO_2 significantly boosts bifunctional oxygen electrocatalytic activity and stability [96]. Lu and al. pyrolyzed a Co/Mn bimetallic MOF (Co/Mn-MIL-100), creating a synergetic heterostructure of MnO/Co/porous graphitic carbon with promising bifunctional oxygen electrocatalysis performance [99]. Liu et al. linked the high efficiency of cobalt–manganese mixed oxide-based bifunctional electrocatalysts to the synergistic effect between non-spinel CoO and MnO [100]. Sugawara et al. studied how metal coordination fashion influences ORR/OER activities among different Co-Mn bimetallic oxides, confirming that layer-type Co-Mn oxides show the highest ORR/OER-specific activities [101].

Additionally, Zn-based M-N-C electrocatalysts are notably resistant to Fenton-like reactions, which helps them maintain strong durability in challenging conditions [102]. Ye et al. synthesized nitrogen-doped carbon from Zn-MOF-74 pyrolyzed at 1000 °C, achieving an ORR onset potential of 1.02 V and a half-wave potential ($E_{1/2}$) value 0.90 V [103]. Furthermore, ZIF-8 has been utilized as a template for creating core-shell ZIF-8@ZIF-67 structures, resulting in the formation of cobalt nanoparticles, as reported by Pan and Liu [104,105].

5. AIM OF THE STUDY

The primary objective of this PhD thesis was to prepare and evaluate novel TAL-derived M-N-C electrocatalysts for their potential application as electrode materials in anion-exchange membrane fuel cells and zinc–air batteries. A key aim was to identify relationships between synthesis strategies, material structures, and electrocatalytic performance. The thesis is organized into five main sections:

1. Synthesis of a range of M-N-C materials, including cobalt, zinc, manganese and bimetallic cobalt-manganese materials, derived from TAL metal–organic framework precursors.
2. Thorough physicochemical and electrochemical characterization of the synthesized materials in order to study their structural, morphological, and electronic properties relevant to electrocatalysis.
3. Optimization of the pyrolysis and acid-leaching protocols, with the goal of enhancing the exposure of active sites and improving the overall performance of the catalysts.
4. Evaluation of the oxygen reduction reaction and oxygen evolution reaction activities of the developed materials in practical electrochemical energy systems, specifically in zinc-air battery and anion-exchange membrane fuel cell.
5. Establish clear structure-activity relationships that contribute to a deeper understanding of the factors influencing the electrocatalytic performance of the catalyst materials.

6. EXPERIMENTAL

6.1 Materials and equipment

The following reagents were used as received without further purification: cobalt(II) chloride hexahydrate ($CoCl_2 \cdot 6H_2O$), 1H-benzo[d]imidazole-5,6-diol, aqueous ammonia solution (NH_3), N,N-dimethylformamide (DMF), ethanol (EtOH), isopropanol (C_3H_7OH), zinc chloride ($ZnCl_2$), manganese(II) chloride tetrahydrate ($MnCl_2 \cdot 4H_2O$), nitric acid (HNO_3), sulfuric acid (H_2SO_4), hydrochloric acid (HCl), and a nitric–sulfuric acid mixture ($HNO_3 + H_2SO_4$). Ultrapure water (18.2 MΩ·cm), obtained from a Milli-Q purification system (Millipore, Inc.), was used in the preparation of all aqueous solutions. Where specified, deionized water was also used. A tubular furnace (Carbolite Gero EST 12/300B) was employed to carry out the post-synthetic pyrolysis of synthesized materials.

6.2 Synthesis

1H-Benzo[d]imidazole-5,6-diol ligand was synthesized following a previously reported method [106–108]. Specifically, 1H-benzo[d]imidazole-5,6-diol (7.79 g, 43.7 mmol, 1.0 equivalent) was added to 48% HBr solution (50 mL) and stirred at 120 °C. After 4 h, the reaction mixture was cooled to 0 °C, and the resulting precipitate was collected, washed with petroleum ether, and dried to yield a colorless solid (4.59 g, 30.6 mmol, 70%). (1 H NMR (400 MHz, dimethyl sulfoxide (DMSO)) δ 9.75 (s, 2H), 9.25 (s, 1H), 7.12 (s, 2H). 13C NMR (100 MHz, DMSO) δ 146.4, 136.9, 123.7, 98.4).

6.2.1 Synthesis of TAL-derived Co-N-C catalysts

Co-700Lx, Co-800Lx, Co-900Lx, and Co-1000Lx (x = 1 … 8): $CoCl_2 \cdot 6H_2O$ (3.96 g, 16.64 mmol, 1.0 equivalent) was added to a solution of 1H-benzo-[d]imidazole-5,6-diol (5.00 g, 33.30 mmol, 2.0 equivalents) in a solvent mixture containing 25% aqueous ammonia, dimethylformamide, ethanol, and water (4:10:10:15 volume ratio). The reaction mixture was stirred at room temperature for 24 h, then filtered and dried, yielding 6.28 g of TAL-2 precursor material. TAL-2 underwent post-synthetic modification via flash pyrolysis under a nitrogen atmosphere for 2 h at four different temperatures: 700, 800, 900, and 1000 °C. The resulting pyrolyzed samples (Co-700, Co-800, Co-900, and Co-1000) were then subjected to acid leaching using eight different protocols, all employing 0.5 M acid solutions. Specifically, the samples were treated with 0.5 M nitric acid, sulfuric acid, hydrochloric acid, or a combination of nitric and sulfuric acids. These suspensions were stirred under two sets of conditions: 5 h at 80 °C (L1-L4) and 8 h at 50 °C (L5-L8). After acid leaching, the samples were filtered and re-pyrolyzed under an inert atmosphere for 2 h at the same temperature. For comparison, control samples (Co-700, Co-800, Co-900, and Co-1000) were left

untreated. This post-treatment process generated 36 distinct Co–N–C catalyst samples, each exhibiting unique properties (Figure 4).

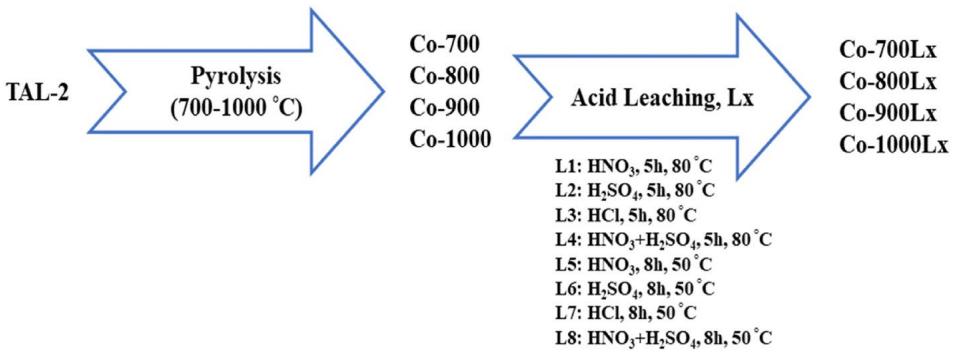

Figure 4. Preparation of TAL-2-derived Co-N-C catalyst materials [109].

6.2.2 Synthesis of TAL-derived CoMn-N-C catalysts

TAL-4, a manganese-based MOF, was synthesized by adding $MnCl_2 \cdot 4H_2O$ (20.2 mmol, 1.0 equivalent) to a solution of 1H-benzo[d]imidazole-5,6-diol (40.4 mmol, 2.0 equivalents) in a 25% aqueous mixture of NH_3, DMF, ethanol, and water (4:10:10:15; 50 mL). The mixture was stirred at room temperature for 24 h, then filtered, washed with ethanol, and dried overnight at 60 °C.

TAL-42, a mixed-metal Mn/Co-based MOF, was prepared by adding $MnCl_2 \cdot 4H_2O$ (10.1 mmol, 1.0 equivalent) and $CoCl_2 \cdot 6H_2O$ (10.1 mmol, 1.0 equivalent) to a similar solution containing 1H-benzo[d]imidazole-5,6-diol (41.4 mmol, 4.0 equivalents). The reaction mixture was stirred at room temperature for 24 h, followed by filtration, ethanol washing, and drying overnight at 60 °C.

TAL-4/TAL-2 was synthesized by mixing of TAL-4 with the previously reported cobalt-based MOF TAL-2 [108] and sonicated in isopropanol for 2 h. The resulting mixture was then dried overnight at 60 °C. All three MOFs (TAL-4, TAL-42, and TAL-4/TAL-2) were subjected to pyrolysis at 900 °C under a nitrogen atmosphere for 2 h, with rapid heating and cooling. The pyrolyzed materials were then acid-etched in 0.5 M H_2SO_4 by stirring for 8 h at 50 °C. After filtration, the samples underwent a second pyrolysis step at 900 °C under nitrogen for 2 h. The final catalyst powders were labeled as TAL-4-900, TAL-42-900, and TAL-4/TAL-2-900, respectively.

6.2.3 Synthesis of TAL-derived Zn-N-C catalysts

The Zn-TAL MOF was synthesized by dissolving $ZnCl_2$ (1.38 g, 10.1 mmol, 0.5 equivalent) in a solution of 1H-benzo[d]imidazole-5,6-diol (3.0 g, 20.2 mmol, 2.0 equivalents) in a solvent mixture of 25% aqueous NH_3, dimethylformamide (DMF), ethanol, and water (4:10:10:15; 50 mL). The mixture was stirred at room temperature for 24 h, after which the solid product was filtered, washed with

ethanol, and dried at 60 °C for 12 h. The dried Zn-TAL was then subjected to pyrolysis under a nitrogen atmosphere for 1 h at four different temperatures (700, 800, 900, and 1000 °C) with a heating rate of 20 °C min^{-1}. The pyrolyzed samples were subsequently acid etched using 3 M HCl for 12 h at room temperature to remove residual zinc and generate hollow, porous structures. However, acid treatment can introduce Cl^- ions and other residual species into the carbon matrix, potentially influencing catalyst stability and performance [109]. To eliminate these residues and further enhance material properties, the etched materials underwent a second pyrolysis step (re-pyrolysis). This additional treatment ensured complete acid removal, promoted structural reorganization, improved conductivity, optimized nitrogen coordination, and stabilized active sites [110,111]. Following this process, the acid-etched materials were filtered, washed with deionized water, and re-pyrolyzed. The final Zn-N-C catalyst powders were designated as Zn-TAL-700, Zn-TAL-800, Zn-TAL-900, and Zn-TAL-1000, corresponding to their respective pyrolysis temperatures.

6.3 Physical characterization

6.3.1 Nitrogen physisorption measurements

Low-temperature N_2 adsorption analysis was conducted using a NOVAtouch LX2 (Quantachrome Instruments) to evaluate the textural properties of the prepared materials, including BET surface area (S_{BET}), total pore volume (V_{tot}), specific surface area (S_{DFT}), micropore volume (V_{μ}), and pore size distribution (PSD). Before measurement, all samples were degassed under vacuum at 300 °C for 12 h.

6.3.2 Powder X-Ray Diffraction (PXRD) analysis

Powder X-ray diffraction (PXRD) analysis was conducted using a Bruker D8 Advance diffractometer equipped with a Ni-filtered Cu Kα radiation source and a LynxEye line detector. The catalysts were examined in a 2θ range of 3° to 93°, with a scanning step size of 0.013° 2θ and a counting time of 356 seconds per step.

6.3.3 X-Ray Photoelectron Spectroscopy (XPS)

X-ray photoelectron spectroscopy (XPS) analysis was performed using a PHI-TFA XPS spectrometer (Physical Electronics, Inc.), equipped with a monochromatic Al Kα X-ray source under high vacuum (10^{-9} mbar). Narrow multiplex scans of the peaks were acquired with a pass energy of 23.5 eV, a step size of 0.25 eV, and a take-off angle of 45° relative to the sample surface. To neutralize surface charge, a low-energy electron gun was utilized. The collected spectra were analyzed using Multipak v8.0 (Physical Electronics, Inc., Chanhassen, MN, USA).

6.3.4 Microwave Plasma Atomic Emission Spectroscopy (MP-AES)

Microwave plasma–atomic emission spectroscopy (MP-AES) analysis was conducted using an Agilent 4210 MP-AES. The analytical wavelengths were set to 371.993 nm for Fe and 340.512 nm for Co. Catalyst samples (10 mg) were digested in a microwave system (Anton Paar Multiwave PRO) using a mixture of 2 mL H_2O_2 and 4 mL HNO_3 in NXF100 vessels (PTFE/TFM liner) at 230 °C under pressures ranging from 45 to 50 bar. The digested samples were then diluted with 2% HNO_3 to achieve a metal concentration of 5 mg L^{-1}.

6.3.5 Scanning Transmission Electron Microscopy (STEM)

A double-corrected and monochromated Themis Z scanning transmission electron microscope (STEM) (ThermoFisher Scientific-TFS) was used for imaging, operating at 300 kV in high-angle annular dark-field (HAADF) STEM mode. The beam convergence angle was approximately 24.0 mrad, and a probe current of 50 pA was applied for STEM imaging. Energy-dispersive X-ray spectroscopy (STEM-EDS) mapping was performed using a Dual X EDS system (Bruker) with two large-area detectors, covering 1.76 steradians, and utilizing a probe current of 100 pA for over one hour. Data acquisition and analysis were carried out using Velox software.

6.3.6 Thermogravimetric analysis (TGA)

Thermogravimetric–Differential Thermal Analysis (TG-DTA) was performed using a Setaram Labsys Evo 1600 thermo-analyzer in an argon atmosphere. Samples (6.0–6.9 mg) were placed in a standard 100 µL crucible and subjected to thermal analysis under a gas flow rate of 20 mL min^{-1}. Initially, the temperature increased to 300 °C at a heating rate of 10 °C min^{-1} under non-isothermal conditions, followed by an isothermal hold at 300 °C for 1 h. Subsequently, the temperature was further raised to 800 °C at the same heating rate and maintained at 800 °C for an additional hour.

6.4 Electrochemical assessment

Catalyst ink preparation
Electrocatalyst inks were formulated by mixing 5 mg of catalyst powders with 495 µL of isopropanol and 5 µL of Nafion ionomer solution (5 wt.%, Sigma-Aldrich). To ensure uniform dispersion, the suspensions were sonicated for 10 min.

Electrode modification
The catalyst suspensions were applied to alumina-polished glassy carbon (GC) electrodes in five 2 µL increments (totaling 10 µL) to achieve a material loading of 0.5 mg cm^{-2}.

Electrochemical measurements

The electrocatalysts were evaluated using a standard three-electrode electrochemical cell system connected to an Autolab PGSTAT128N potentiostat/ galvanostat (Metrohm Autolab B.V., The Netherlands) and operated via Nova 2.1.4 software. A GC rotating disk electrode (5 mm in diameter) functioned as the working electrode, while the reference and counter electrodes were a silver-silver chloride (Ag/AgCl) electrode and a GC rod, respectively. The alkaline electrolyte solution was prepared by dissolving 2.8 g of KOH (purity ≥99.998%, Sigma-Aldrich) in 500 mL of Milli-Q water. Prior to use, the electrolyte was either saturated with pure O_2 (99.999%, Linde Gas) or purged with Ar gas (99.999%, Linde Gas) to remove oxygen. Cyclic voltammetry (CV) curves were recorded in an Ar-saturated electrolyte at scan rates of 50 mV s^{-1} and 10 mV s^{-1}. Additionally, the samples underwent potential cycling in an Ar-saturated solution to assess the electrochemical double-layer capacitance. The modified electrodes were subjected to cycling at scan rates of 10, 20, 30, 40, and 50 mV s^{-1}. Cathodic and anodic current density values were extracted from the measured data at non-Faradaic potentials. The ORR polarization curves were measured in an O_2-saturated 0.1 M KOH electrolyte at a scan rate of 10 mV s^{-1} across different electrode rotation speeds (360, 610, 960, 1600, 1900, and 3100 rpm). Subsequently, the OER activity was examined in an Ar-saturated 0.1 M KOH electrolyte with a scan rate of 10 mV s^{-1}. An 85% iR compensation was applied to all electrochemical data where necessary. Potentials were then converted to the reversible hydrogen electrode (RHE) scale using Eq. 9:

$$E_{Ag/AgCl} = E_{RHE} - 0.966\ (E_{RHE} = E_{Ag/AgCl} + 0.0591\ pH + E^{0}_{Ag/AgCl}\ (0.209)) \quad (9)$$

The key ORR kinetic parameters, including onset potential, half-wave potential, kinetic current density (j_k), diffusion-limited current density (j_d), the number of electrons transferred per O_2 molecule (n), and Tafel slope values, were derived from the rotating disk electrode (RDE) data. The RDE data was analyzed using the Koutecky-Levich (K-L) equation [112].

$$\frac{1}{j} = \frac{1}{j_k} + \frac{1}{j_d} = \frac{1}{nFkC^b_{O_2}} + \frac{1}{0.62nFC^b_{O_2}D^{2/3}_{O_2}\upsilon^{-1/6}\omega^{1/2}} \quad (10)$$

In the equation above, the current densities (in mA cm^{-2}) are defined as follows: j represents the measured current density, j_k denotes the kinetic current density, and j_d refers to the diffusion-limited current density. The remaining parameters are specified as follows: ω is the electrode rotation rate (rad s^{-1}), n is the number of electrons transferred per oxygen molecule, F is the Faraday constant (96,485 C mol^{-1}) [113], C^b is the oxygen concentration in 0.1 M KOH (1.2×10^{-6} mol cm^{-3}), D_{O2} is the diffusion coefficient of O_2 (1.9×10^{-5} cm^2 s^{-1} in 0.1 M KOH), and υ represents the kinematic viscosity of the solution (0.01 cm^2 s^{-1}) [114].

The overall oxygen electrode bifunctional activity was determined as the potential difference (ΔE) between the ORR half-wave potential and the OER potential at a current density of 10 mA cm^{-2} ($E_{j=10}$), given by:

$$\Delta E = E_{j=10} - E_{1/2} \quad (11)$$

Assembly of zinc-air battery

ZAB tests were performed using an in-house single-cell battery in a two-electrode setup, constructed with a stacked plate arrangement. The air cathode was made from a nickel mesh, which served as the current collector, and a carbon paper gas diffusion layer (Sigracet BB39). The catalyst ink was applied to the cathode layer via hand-brush coating, with a loading of 2 mg cm^{-2}. Zinc foil (99%) was used as the anode, and the electrolytes consisted of a 6 M KOH solution containing and 0.2 M $Zn(CH_3COO)_2$. The catalyst inks were formulated by mixing 7 mg of catalyst, 20 μL of 5% Nafion ionomer solution (Sigma-Aldrich), 0.2 mL of MilliQ water, and 0.6 mL of ethanol, and stirring for 1.5 h. Commercial PtRu/C (Pt – 50 wt.%, Ru – 25 wt.%) was used to prepare the benchmark PtRu catalyst ink. Galvanostatic tests were conducted using a potentiostat/galvanostat (Autolab PGSTAT204).

Anion exchange membrane fuel cell testing

To demonstrate the practical application in an anion exchange membrane fuel cell (AEMFC), the Zn-TAL-1000 electrocatalyst was prepared as a cathode using procedures similar to those outlined in previous publications [74,115,116]. The cathode and anode were loaded with 1 $mg_{Zn/TAL-1000}$ cm^{-2} and 0.6 mgPtRu cm^2, respectively, and a high-density polyethylene (HDPE)-based anion exchange membrane was employed. The AEMFC was tested in a Scribner Associates 850E test station at a cell temperature of 60 °C, with the anode humidifier set to 54 °C and the cathode humidifier at 56 °C. The gas flow rates for both hydrogen and oxygen were kept at 1 standard liter per minute (SLPM), with a back-pressure of 100 kPag. The polarization curve was measured by scanning from an open-circuit voltage (OCV) of approximately 1 V to 0.1 V at a scan rate of 10 mV s^{-1}.

7. RESULTS AND DISCUSSION

7.1 TAL-derived Co-N-C electrocatalysts

7.1.1 Morphology and composition of TAL-derived Co-N-C catalysts

The morphology of all 36 samples was initially examined using scanning transmission electron microscopy. Representative STEM images (Figure 5a) reveal that the synthesized Co-N-C samples consist mostly of cobalt nanoparticles uniformly dispersed within the carbon matrix. The average metal particle size for each sample, determined from the STEM images, is presented in Figure 5b. The smallest particle size (16 nm) was observed in sample Co-800L7, which was pyrolyzed at 800 °C and subsequently leached with HCl at 50 °C for 8 h. In contrast, the largest particle size (50 nm) was found in the non-leached sample Co-1000L8. A clear trend was observed in samples pyrolyzed at 700-900 °C, where acid leaching, particularly under the L7 conditions, resulted in the smallest particle sizes.

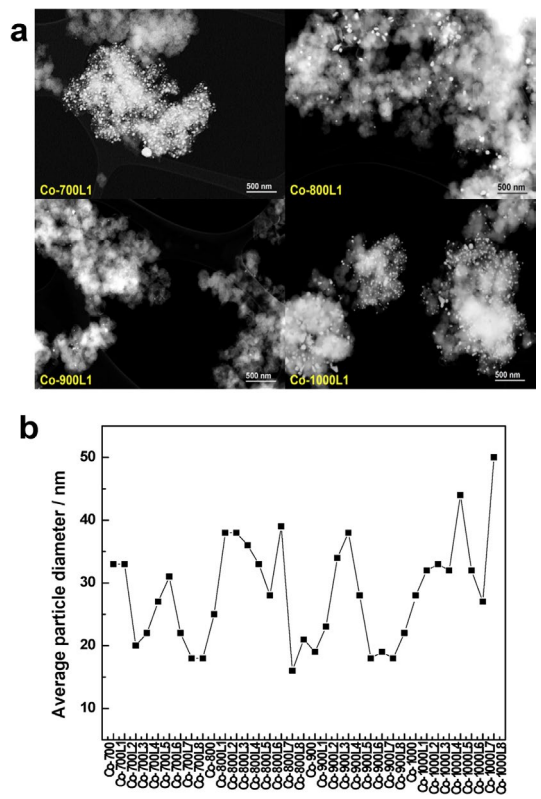

Figure 5. (a) Representative high-angle annular dark-field (HAADF) STEM images of selected samples; (b) an average cobalt particle size calculated from STEM images [109].

PXRD analysis was conducted to examine the crystallographic structure of TAL-2-derived materials, with patterns shown in Figure 6. The results confirmed the presence of graphitic carbon, metallic cobalt, and hexagonal cobalt. Co-700L2 and Co-700L4 contained cobalt sulfide (Co_9S_8), likely due to sulfuric acid in the leaching process, indicating that 700 °C was insufficient to remove acid impurities. Higher temperatures increased coarse graphite, metallic cobalt content, while reducing hexagonal cobalt. The 26° XRD peak (002 plane) suggested strong graphitization, supported by Raman spectroscopy (Figure 7). Peaks at 44.1°, 51.3°, and 75.7° correspond to metallic cobalt (PDF #15-0806) [117] (Figure 6). At high temperatures, cobalt ions catalyzed ligand transformation into graphitized carbon, enhancing electroconductivity [118].

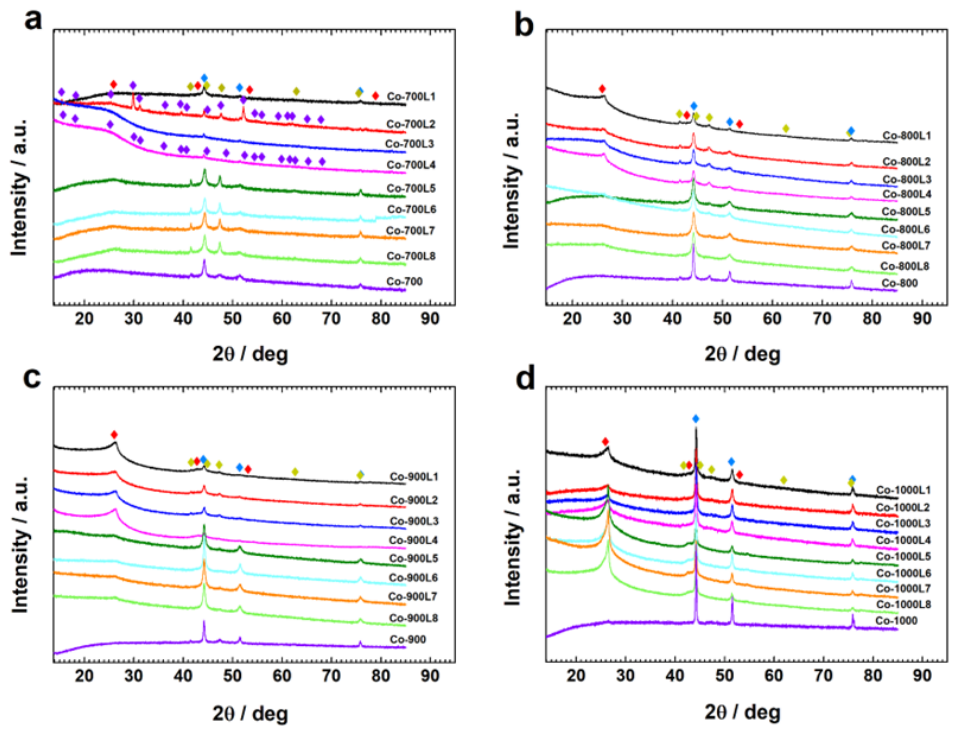

Figure 6. PXRD patterns of all TAL-2-derived catalysts: ♦ C Hexagonal (PDF 00_058_1638); ♦ Metallic Co (PDF 00_015_0806); ♦ Co Hexagonal (PDF 04_001_3273); ♦ Co_9S_8 Cubic (PDF 00_056_0002) [109].

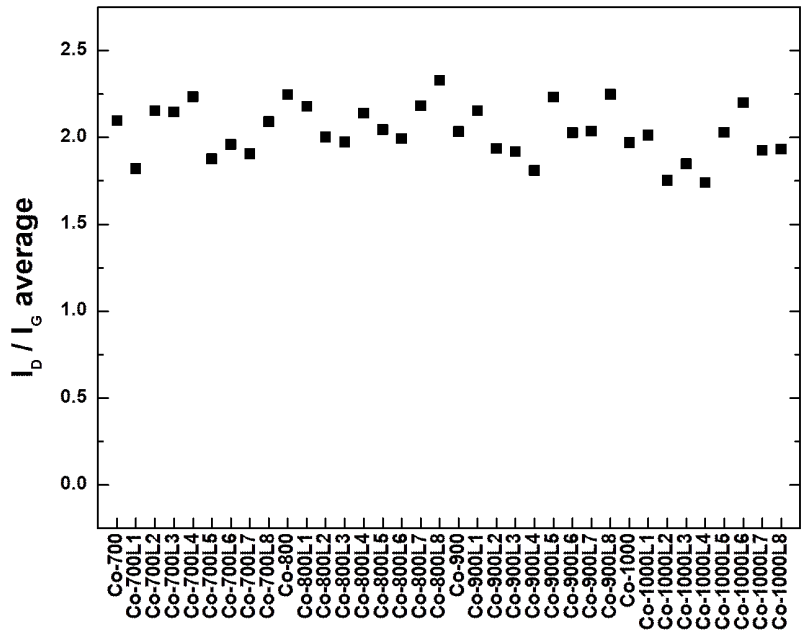

Figure 7. I_D/I_G ratios for various Co-N-C electrocatalyst materials obtained from Raman spectroscopy study [109].

Nitrogen physisorption analysis was performed to assess the textural properties of the prepared materials and the effects of post-treatment. The specific surface area and total pore volume varied across the Co–N–C catalysts (Figure 8). Non-leached samples (Co-700, Co-800, Co-900, and Co-1000) had the lowest surface area (300–500 m^2 g^{-1}) and pore volume (0.3–0.5 cm^3 g^{-1}). In contrast, samples leached in a nitric and sulfuric acid mixture for 5 h at 80 °C showed significantly higher surface areas, with Co-800L4 reaching 908 m^2 g^{-1}, the highest among them. This increase is attributed to impurity removal and additional pore formation, highlighting the effectiveness of pyrolysis at 800 °C combined with acid leaching.

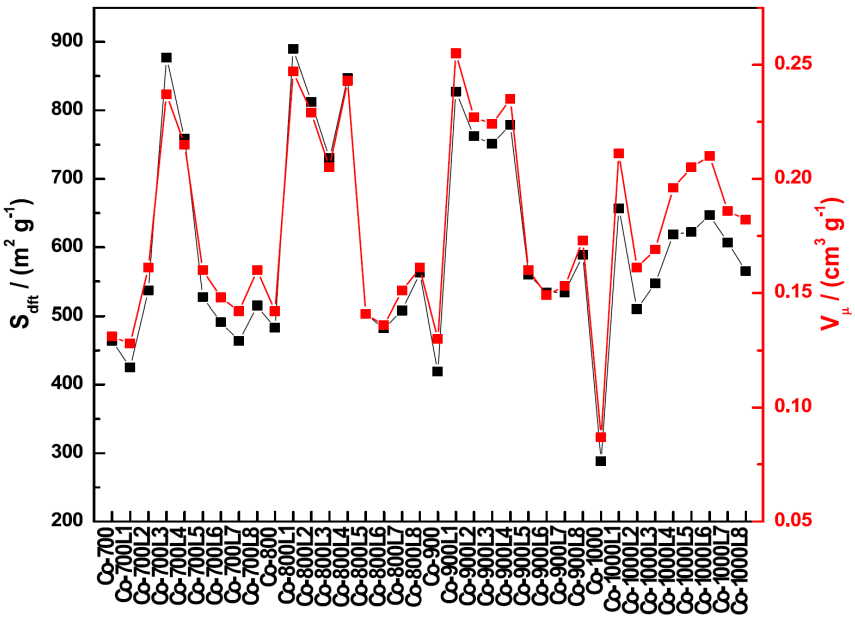

Figure 8. Specific surface area and volume of micropores obtained for Co-N-C samples post-treated at different conditions [109].

X-ray photoelectron spectroscopy (XPS) analyzed the chemical composition and surface states of all samples (Figure 9), confirming the presence of C, N, Co, and O. Carbon content increased with pyrolysis temperature, while surface nitrogen content decreased from 15 to 2.5 at.%. Bisen et al. reported that ~9 at.% N enhances Co-N-C electrocatalysts by improving ORR onset potential and exchange current density [119]. Samples L1-L4 had lower Co and O content than L5-L8, indicating more effective high-temperature leaching (Figure 9).

High-resolution XPS spectra (Figure 10) revealed sp^2 and sp^3 carbon (Figure 10a). Co-1000 (non-leached) had the highest sp^2 (79%) and lowest sp^3 (5%) carbon content. Higher pyrolysis temperatures favored the formation of carbon graphitic structures, disrupting π conjugation and enhancing ORR electrocatalysis [120]. The presence of sp^3 carbon improved ORR and OER activity [121].

Pyridinic and pyrrolic nitrogen content decreased with pyrolysis temperature (Figure 10b), shifting toward graphitic-N, which improves electrical conductivity and stability [122]. Figure 10c shows four oxygen species, with Co-700L2 having the highest COOH (5.01%).

Co3p XPS analysis (Figure 10d) confirmed Co^{2+}, Co^{3+}, and Co^0 in all samples. Higher-temperature leaching (L1-L4) reduced Co surface concentration to <0.1 at.%, enhancing active sites. The synergistic effect of cobalt oxides and metallic cobalt contributed to bifunctional electrocatalytic activity [78,123].

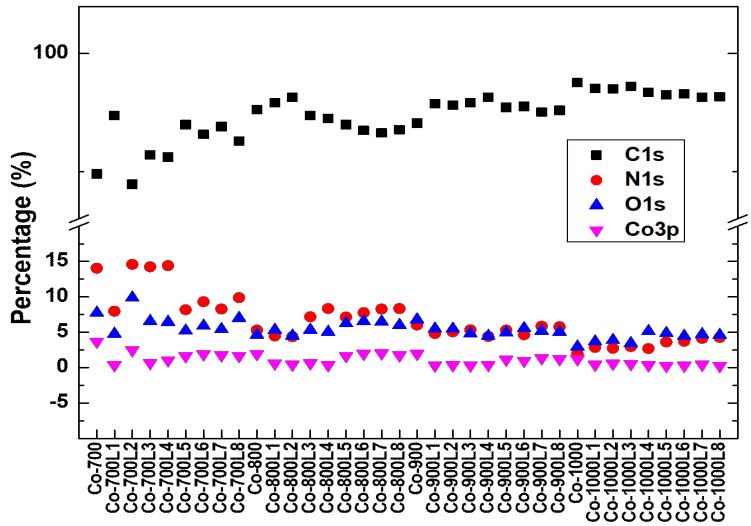

Figure 9. Surface elemental composition of Co-N-C electrocatalyst materials obtained from XPS analysis (at.%) [109].

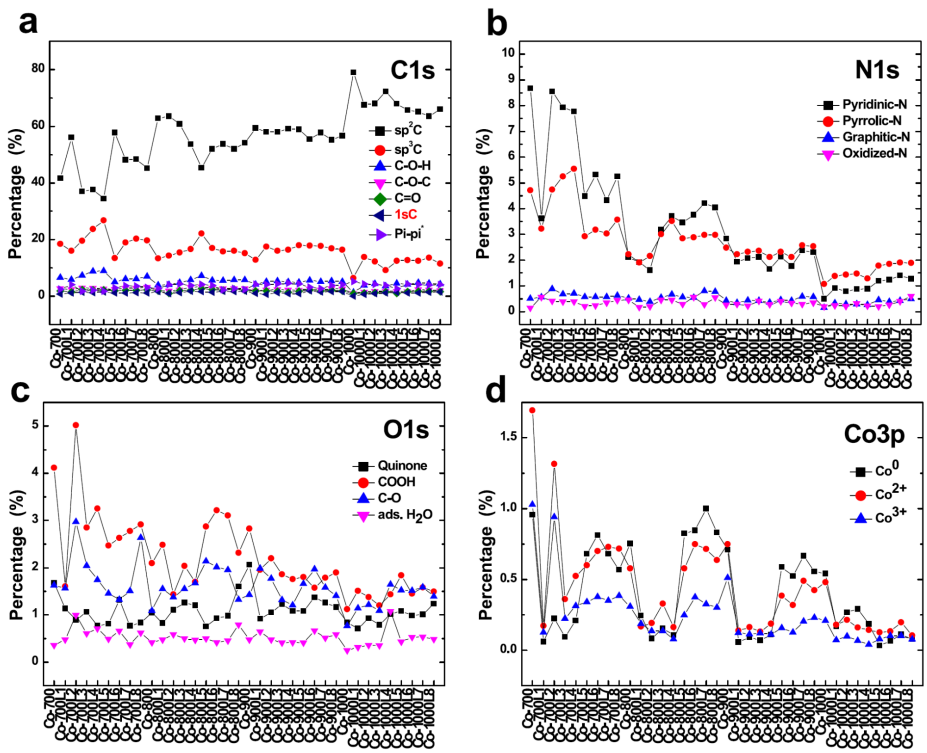

Figure 10. The relative surface concentration of (a) carbon, (b) nitrogen, (c) oxygen, and (d) cobalt species in Co-N-C samples obtained from XPS data [109].

7.1.2 Electrocatalytic activity of TAL-derived Co-N-C catalysts

The electrocatalytic activity of 36 Co-N-C samples was assessed for the ORR and OER in 0.1 M KOH solution. Using the rotating disk electrode (RDE) technique, the ORR polarization curves were recorded between -0.2 and 1.1 V vs. RHE. Among all catalysts, Co-900L3 showed the highest ORR activity (E_{on} = 0.97 V, $E_{1/2}$ = 0.85 V), comparable to Pt/C ($E_{1/2}$ = 0.85 V, E_{on} = 0.98 V) (Table 1) and superior to most Co-N-C catalysts [20,124,125]. Interestingly, its activity was not solely linked to morphology or nitrogen content, suggesting a synergistic effect of multiple factors rather than any single property (Figure 11a).

Tafel analysis (Figure 11b) showed that Co-900L6 had the lowest Tafel slope (-43 mV dec^{-1}), outperforming Co-700L5 (-46 mV dec^{-1}), Co-900L5 (-47 mV dec^{-1}), and Co-900L3 (-52 mV dec^{-1}), and surpassing previous materials such as 3D Co-N-C NN-800 (-83 mV dec^{-1}) [126] and Co_3O_4/HNCP-40 (-69 mV dec^{-1}) [127], indicating better ORR kinetics. Increased cathodic current at higher rotation speeds (360-3100 rpm) (Figure 11c) confirmed enhanced mass transport, with Co-900L3's high BET surface area (728 m^2 g^{-1}) improving catalytic site accessibility. Koutecky-Levich (K-L) analysis (Figure 11d) showed a four-electron reduction pathway.

For OER activity, catalysts were tested in Ar-saturated 0.1 M KOH (Figure 11e). Co-900L5 exhibited a current density of 10 mA cm^{-2} at 1.56 V ($E_{j=10}$), outperforming RuO_2 ($E_{j=10}$ = 1.69 V). Other samples also performed well, including Co-700L5 ($E_{j=10}$ = 1.58 V), Co-900L6 ($E_{j=10}$ = 1.61 V), and Co-900L3 ($E_{j=10}$ = 1.62 V). The high OER performance of Co-900L5 is attributed to its CoO and Co_3O_4 nanoparticles (~18 nm).

Tafel slope obtained for Co-900L5 (274 mV dec^{-1}) was comparable to RuO_2 (166 mV dec^{-1}) and lower than Co-700L5 (309 mV dec^{-1}), Co-900L6 (334 mV dec^{-1}), and Co-900L3 (343 mV dec^{-1}) (Figure 11f), confirming favorable OER kinetics. The bifunctional oxygen electrode activity ($\Delta E = E_{j=10} - E_{1/2}$) was lowest for Co-700L5 and Co-900L5 (0.74 V). This is attributed to their high porosity and the coexistence of Co, CoN_x, CoO, Co_3O_4, and pyridinic-N [78,128–131].

Table 1. Summary of electrochemical kinetic parameters of the ORR nad OER obtained for most active bifunctional electrocatalysts in 0.1 M KOH solution.

Electrocatalyst	$E_{1/2}$ (V)	E_{on} (V)	$E_{j=10}$(V)	ΔE (V)	n	η_{OER} (V)	Tafel slope ORR (mV dec^{-1})	Tafel slope OER (mV dec^{-1})
Co-700L5	0.84	0.93	1.58	0.74	4.0	0.35	-46	309
Co-900L5	0.82	0.91	1.56	0.74	3.9-4.0	0.33	-47	274
Co-900L6	0.86	0.93	1.61	0.75	3.9-4.0	0.38	-43	334
Co-900L3	0.85	0.97	1.62	0.77	4.0	0.39	-52	343
Pt/C+ RuO_2	0.85	0.98	1.69	0.84	4.0	0.46	-60	166

This study optimizes Co-N-C catalysts through post-synthetic treatments, adjusting pyrolysis temperatures and acid-leaching conditions. Structural and electrochemical analyses revealed that acid-leaching at 50 °C minimized particle size, while 80 °C increased surface area. XPS showed that pyrolysis at 700 °C enhanced pyridinic and pyrrolic nitrogen content. Co-700L5 and Co-900L5 exhibited superior bifunctional ORR/OER performance (ΔE = 0.74 V) due to their porous structure and rich cobalt-nitrogen species.

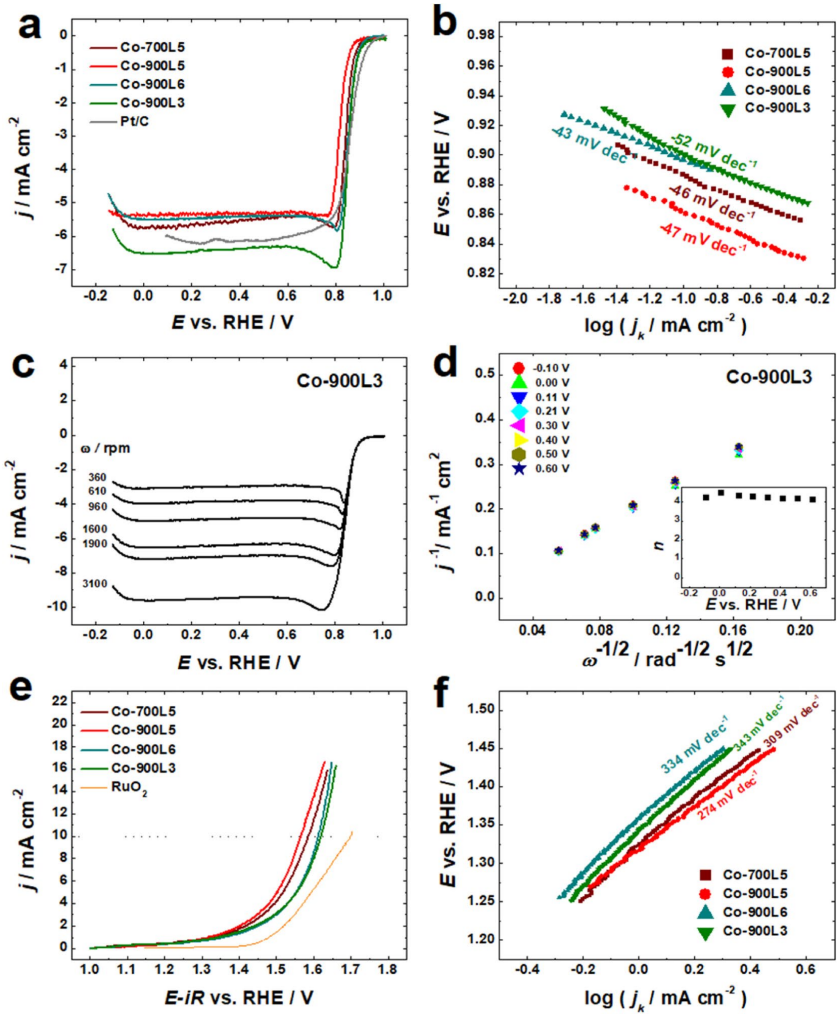

Figure 11. (a) ORR polarization curves recorded for Co-700L5, Co-900L5, Co-900L6, and Co-900L3 and Pt/C catalysts materials in O_2-saturated 0.1 M KOH at 1600 rpm and a scan rate of 10 mV s^{-1}; (b) Tafel plots for ORR obtained for Co-700L5, Co-900L5, Co-900L6, and Co-900L3 catalysts; (c) ORR polarization curves recorded for Co-900L3 at different rotation rates; (d) K–L plots for ORR obtained for Co-900L3 modified GC electrode (Inset: *n* as a function of potential); (e) OER polarization curves in Ar-saturated 0.1 M KOH; ν = 10 mV s^{-1}. (f) Tafel plots for OER [109].

7.2 TAL-derived CoMn-N-C electrocatalysts

7.2.1 Morphology and composition of TAL-derived CoMn-N-C catalysts

First, morphology of TAL-4-900, TAL-42-900, and TAL-4/TAL-2-900 powders was analyzed using STEM. Both bimetallic samples showed a uniform distribution of metallic nanoparticles in the carbon matrix (Figure 12a,d). HR-STEM revealed that TAL-42-900 contained larger clusters of metallic Co (200) and MnO (220) (Figure 12c), while TAL-4/TAL-2 featured metallic Co (111) particles (~18 nm) (Figure 12d). EDS elemental mapping confirmed the even distribution of cobalt, manganese, oxygen, and nitrogen (Figure 12g,h). The mapping images of TAL-4/TAL-2-900 suggest a chemical reaction between the TAL-2 and TAL-4 precursors due to the dispersion of those metals as distinct particles.

STEM results are consistent with XRD data (Figure 13a), confirming that both TAL-42-900 and TAL-4/TAL-2-900 samples primarily contain MnO (JCPDS No. 04-023-6798) and metallic Co (JCPDS No. 01-071-4651). Peaks at 44.2°, 51.5°, and 75.9° indicate metallic Co formation [132], while those at 34.9°, 40.6°, 58.7°, 70.2°, and 73.8° confirm the presence of manganese oxide.

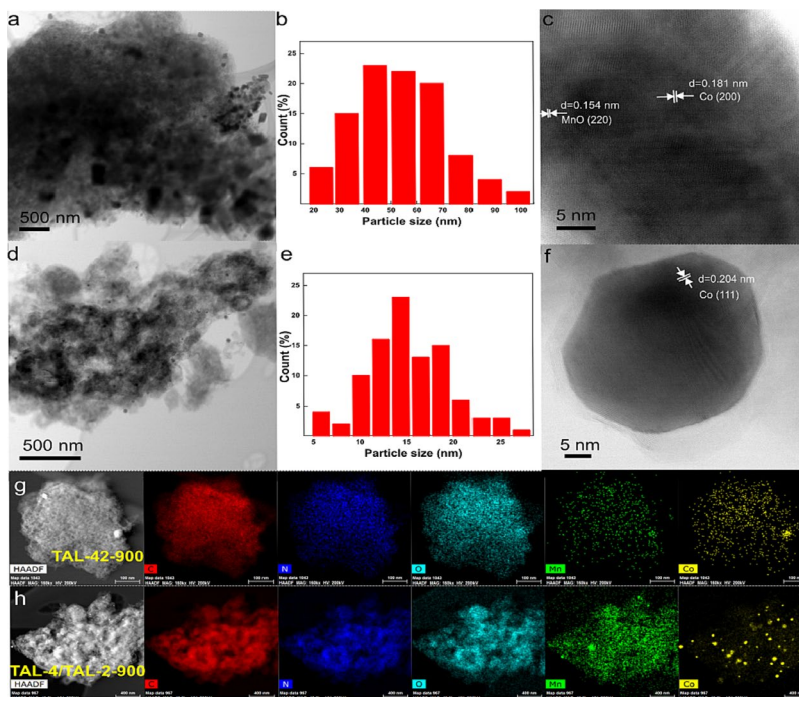

Figure 12. (a,d) Bright-field STEM micrographs of TAL-42-900 and TAL-4/TAL-2-900 electrocatalysts; (b,e) particle size distribution; (c,f) HR-STEM images and (g,h) HAADF-STEM images and EDX mapping of TAL-42-900, and TAL-4/TAL-2-900 samples [106].

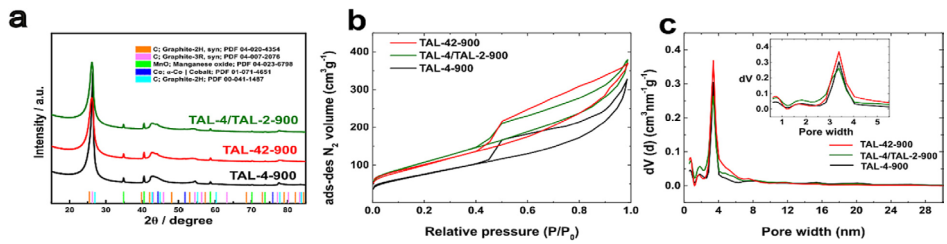

Figure 13. (a) XRD patterns, (b) N_2 physiosorption isotherms and (c) pore size distribution of TAL-4-derived samples [106].

N_2 physisorption analysis showed that all samples exhibited Type-IV isotherms with H4 hysteresis loops (Figure 13b), indicating dominant micro- and mesoporosity (Figure 13c), which supports efficient mass transport. The BET surface areas of TAL-4-900, TAL-42-900, and TAL-4/TAL-2-900 were 268, 354, and 382 $m^2\ g^{-1}$, respectively (Table 2).

Table 2. Textural properties of TAL-4-900, TAL-42-900, and TAL-4/TAL-2-900 [106].

Electrocatalyst	S_{BET} ($m^2\ g^{-1}$)	S_{DFT} ($m^2\ g^{-1}$)	V_{tot} ($cm^3\ g^{-1}$)	V_{μ} ($cm^3\ g^{-1}$)
TAL-4-900	268	252	0.43	0.05
TAL-42-900	354	351	0.53	0.06
TAL-4/TAL-2-900	382	348	0.51	0.08

XPS analysis (Figure 14a) confirmed the presence of Mn, Co, C, N, and O in both bimetallic catalysts. Both TAL-42-900 and TAL-4/TAL-2-900 materials had 1.1 at% nitrogen (Table 3), with N 1s spectra showing graphitic, pyrrolic, and pyridinic nitrogen species (Figure 14d). Notably, TAL-42-900 also exhibited M-N_x (399.2 eV) and oxidized-N (404.5 eV) species (Figure 14e), suggesting atomically dispersed active sites [133–135].

Co 2p XPS spectra (Figure 14b) revealed metallic Co and Co-O-Mn species [99,136], supported by STEM-EDX analysis (Figure 12g-h). Mn 2p spectra indicated Mn^{2+} and Mn^{3+} states (Figure 14c), with strong MnO/Co interfaces enhancing the ORR/OER activity [99]. TAL-42–900 had the highest Mn surface content (0.3 at%) and lower bulk Co content (0.369 wt%) compared to TAL-4/TAL-2-900 (0.641 wt%).

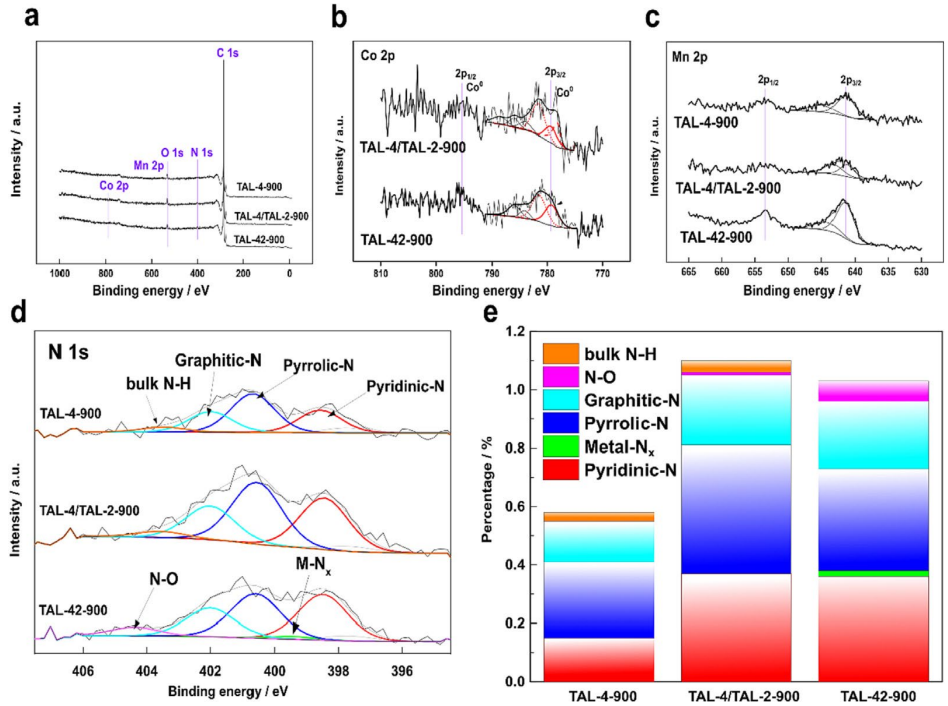

Figure 14. (a) XPS survey spectra; (b, c, d) deconvoluted high-resolution spectra of Co 2p, Mn 2p, and N 1s for TAL-4-900, TAL-42-900, and TAL-4/TAL-2-900; (e) distribution of various nitrogen species on the catalyst surfaces [106].

Table 3. The elemental composition of TAL-4-900, TAL-42-900, and TAL-4/TAL-2-900 catalysts, analyzed using XPS, and the bulk metal content determined via MP-AES [106].

Electrocatalyst	**Surface elemental composition (at%)**						**Bulk metal composition (wt%)**	
	C	O	N	Mn	Co	Si	Co	Mn
TAL-4-900	96.4	2.3	0.6	0.2	0	0.4	0	1.101
TAL-42-900	95.9	2.2	1.1	0.3	0.1	0.5	0.369	1.202
TAL-4/TAL-2-900	95.7	2.5	1.1	0.1	0.1	0.5	0.641	0.835

7.2.2 Electrocatalytic activity of TAL-derived CoMn-N-C catalysts

The electrocatalytic performance of TAL-4-900, TAL-42-900, and TAL-4/TAL-2-900 catalysts was evaluated as bifunctional ORR and OER activity, alongside with commercial Pt/C and RuO_2 benchmarks. Cyclic voltammetry (CV) in Ar- and O_2-saturated 0.1 M KOH (scan rate: 10 mV s^{-1}) revealed clear ORR peaks around 0.80 V vs. RHE for all three catalysts (Figure 15). Electrochemical impedance spectroscopy showed that the material TAL-42-900 had a lower charge-transfer resistance (48 Ω) compared to TAL-4/TAL-2-900 (66 Ω), indicating improved conductivity.

ORR polarization curves (-0.2 to 1.1 V vs RHE, Figure 16a) recorded at 1600 rpm showed that TAL-42-900 had the highest ORR onset (0.93 V vs. RHE) and half-wave potential ($E_{1/2}$ = 0.84 V vs. RHE), only 10 mV below commercial Pt/C (0.85 V vs. RHE). This superior ORR performance is attributed to a heterogeneous MnO/Co surface and the presence of pyridinic and M-N_x active sites [135,137,138].

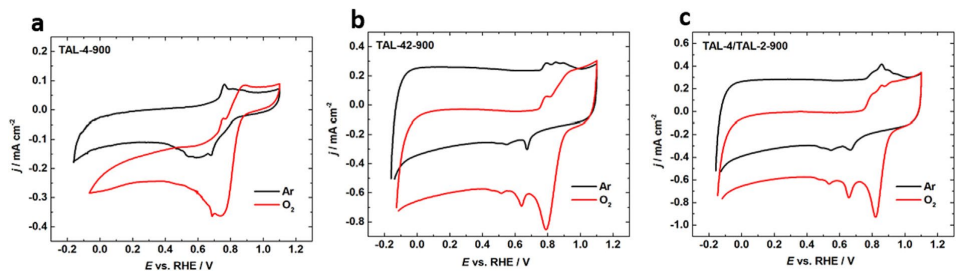

Figure 15. CV curves obtained for (a) TAL-4-900, (b) TAL-42-900, and (b) TAL-4/TAL-2-900 catalysts in O_2-saturated (red line) or Ar-saturated (black line) 0.1 M KOH solution [106].

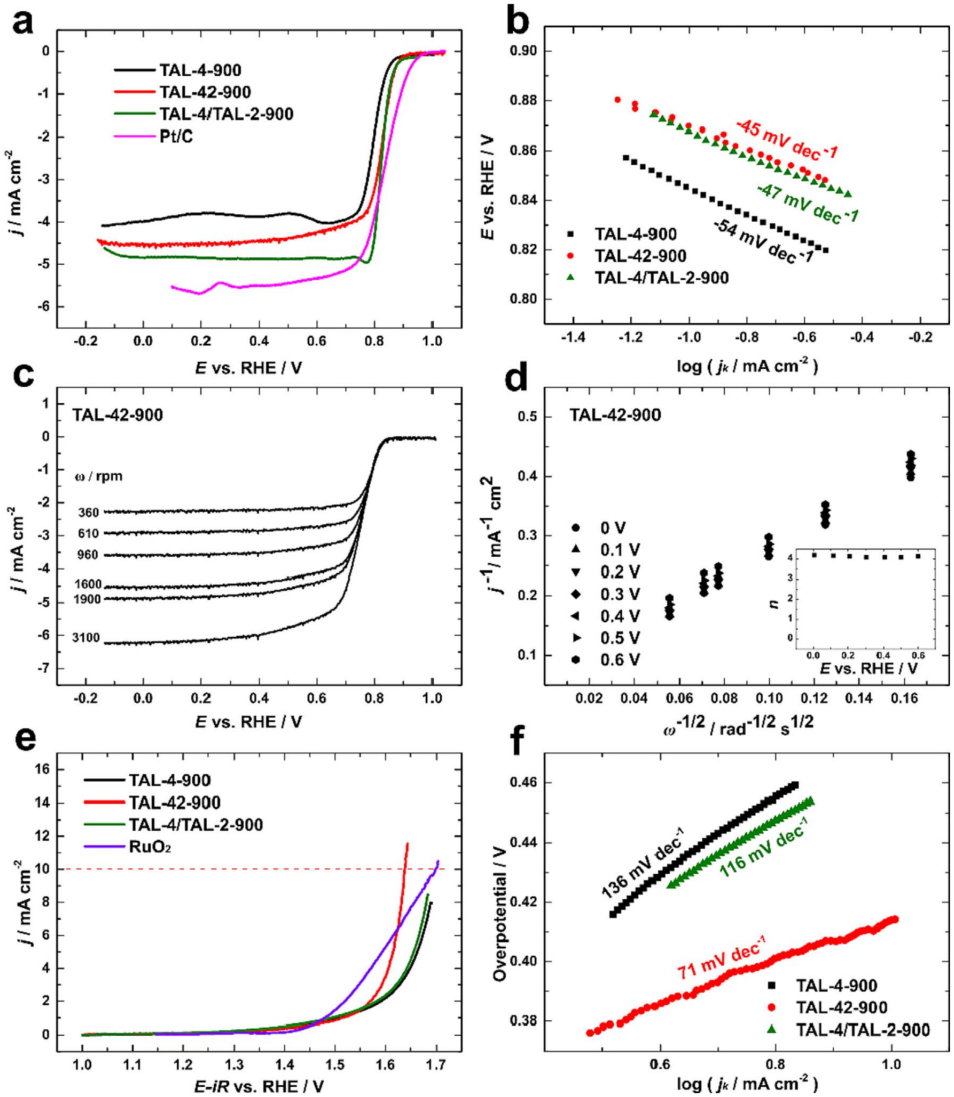

Figure 16. (a) ORR polarization curves of all catalysts recorded in O_2-saturated 0.1 M KOH at 1600 rpm; (b) Tafel plots for ORR derived from RDE data; (c) ORR polarization curves of TAL-42-900 at different rotation rates; (d) Koutecky-Levich plots obtained for TAL-42-900 (inset: electron transfer number *n* calculated via the K-L equation); (e) OER polarization curves recorded in Ar-saturated 0.1 M KOH at 1600 rpm; (f) Corresponding OER Tafel plots [106].

RDE measurements show that the ORR is kinetically controlled between 0.88–1.0 V vs. RHE and becomes diffusion-limited below 0.8 V vs. RHE. Koutecky-Levich (K-L) analysis (Figure 16c) for TAL-42-900 at varying rotation speeds was used to determine the number of electrons transferred per O_2 molecule, confirming a dominant $4e^-$ pathway. Tafel analysis (Figure 16b), with TAL-42-900 showing the lowest slope value (-45 mV dec^{-1}), indicating faster ORR kinetics, consistent with previously reported Mn-N-C and Co/Mn-N-C catalysts [99,139–141].

For OER, linear sweep voltammetry (LSV) was performed in Ar-saturated 0.1 M KOH at 1600 rpm (Figure 16e). TAL-42-900 reached 10 mA cm^{-2} at 1.64 V vs RHE, with a lower overpotential (0.41 V) than TAL-4-900, TAL-4/TAL-2-900, and RuO_2 (0.48, 0.45, and 0.46 V, respectively). A steeper current increase at higher potentials further confirmed its superior electrocatalytic activity. OER Tafel plots (Figure 16f) showed TAL-42-900 with the lowest slope, reflecting faster kinetics, characteristic of a $4e^-$ process involving OH^- adsorption followed by O_2 evolution [136,142].

Overall bifunctional performance was assessed, with TAL-42-900 exhibiting the lowest value (0.80 V), outperforming even the Pt/C + RuO_2 hybrid (Table 4). Functionally, Co in the catalyst enhances the ORR kinetics by facilitating electron transfer and acting as active sites via Co^{2+}/Co^{3+} species [96,143]. MnO primarily supports OER by promoting water oxidation [144]. The presence of both Mn^{2+} and Mn^{3+} creates oxygen vacancies, improving conductivity and intermediate adsorption, thereby enhancing bifunctional activity through Co-MnO synergy [145].

Table 4. Summary of electrochemical kinetic parameters [106].

Electrocatalyst	$E_{1/2}$ (V)	E_{on} (V)	$E_{j=10}$ OER (V)	ΔE (V)	n	η_{OER} (V)	Tafel slope ORR (mV dec^{-1})	Tafel slope OER (mV dec^{-1})
TAL-4-900	0.80	0.91	1.71	0.91	3.5	0.48	-54	136
TAL-42-900	0.84	0.93	1.64	0.80	4.1	0.41	-45	71
TAL-4/TAL-2-900	0.83	0.92	1.68	0.85	3.5	0.45	-47	116
Pt/C+ RuO_2	0.85	0.98	1.69	0.84	4.0	0.46	-60	166

Next, a Zn-air battery using TAL-42-900 or Pt-Ru/C (2 mg cm^{-2}) as air electrodes was assembled (Figure 17c). TAL-42-900 showed superior ZAB performance with a peak power density of 155 mW cm^{-2} vs 140 mW cm^{-2} for Pt-Ru/C (Figure 17a). Charge-discharge cycling at 5 mA cm^{-2} yielded 1.21 V (discharge) and 2.07 V (charge), achieving 58% efficiency and 17 h of stable operation (Figure 17b). Pt-Ru/C showed lower power density (139 mW cm^{-2}) and poorer durability [146,147]. A 1H-benzo[d]imidazole-5,6-diol ligand enabled uniform Co/Mn incorporation.

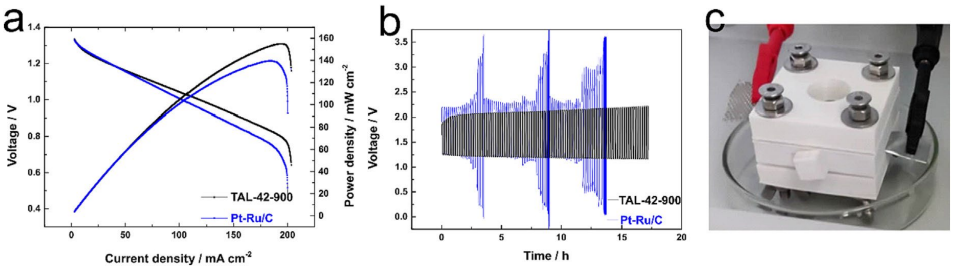

Figure 17. (a) Polarization and power density curves of the ZABs with TAL-42-900 and Pt-Ru/C air electrodes; (b) Discharge and charge voltage cycling profiles for the rechargeable ZABs; (c) Zinc-air battery assembly [106].

7.3 TAL-derived Zn-N-C electrocatalysts

7.3.1 Morphology and composition of TAL-derived Zn-N-C catalysts

Choosing the right ligand is vital in catalyst precursor design, as it influences electrocatalytic activity, selectivity, and electrochemical stability of the catalysts [102,148]. Here, 1H-benzo[d]imidazole-5,6-diol was used for its C/N-rich structure and multidirectional coordination ability. SEM showed the unpyrolyzed Zn-TAL formed hollow spheres (~140–160 nm), which shrank to 100–120 nm and then 60–100 nm upon pyrolysis (Figure 18), while retaining structural integrity. No Zn aggregation was observed, consistent with PXRD analysis.

EDS mapping (Table 5) confirmed presence Zn, O, N, and C in the Zn-TAL catalysts. With increasing pyrolysis temperature, Zn content dropped from 3.87 to 0.20 at.%, while carbon content rose from 71.44 to 94.65 at.%, aligning with reports on Zn evaporation during high-temperature pyrolysis above 1000 °C.

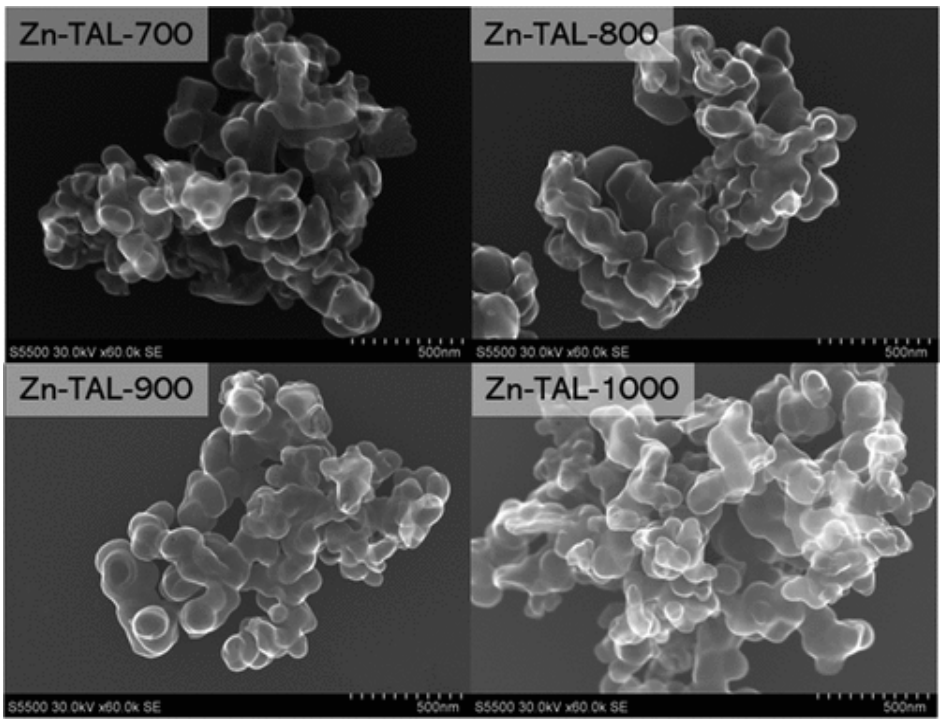

Figure 18. SEM images (secondary electrons imaging mode) of Zn-TAL-700, Zn-TAL-800, Zn-TAL-900 and Zn-TAL-1000 samples [149].

Table 5. Elemental composition (at.%) of Zn-TAL-raw, Zn-TAL-700, Zn-TAL-800, Zn-TAL-900, and Zn-TAL-1000 materials determined by SEM-EDX [149].

Electrocatalyst	**C**	**N**	**Zn**	**O**	**Cl**
Zn-TAL raw	71.44± 0.36	17.30±0.17	3.87±0.03	7.20±0.07	0.19±0.02
Zn-TAL-700	82.30±0.46	9.79±0.16	3.41±0.03	3.66±0.06	0.84±0.03
Zn-TAL-800	86.41±0.40	11.67±0.14	1.71±0.02	N/A	0.21±0.02
Zn-TAL-900	94.11±0.43	4.57±0.10	1.02±0.01	0.30±0.02	N/A
Zn-TAL-1000	94.65±0.43	5.15±0.10	0.20±0.01	N/A	N/A

X-ray diffraction analysis (Figure 19a) confirmed that all four pyrolyzed samples mainly consisted of amorphous carbon, with no detectable Zn-related peaks. This still suggests that residual Zn may be atomically dispersed and nitrogen-co-ordinated. Diffraction peaks at 26.2° and 44.2° correspond to the (002) and (100) planes of graphitic carbon (PDF 01-077-7164) [150,151]. While peak positions

were consistent, the (100) peak intensity slightly increased with pyrolysis temperature, indicating improved crystallinity, whereas the (002) peak intensity decreased, suggesting reduced crystallite size or a structural phase change due to heating.

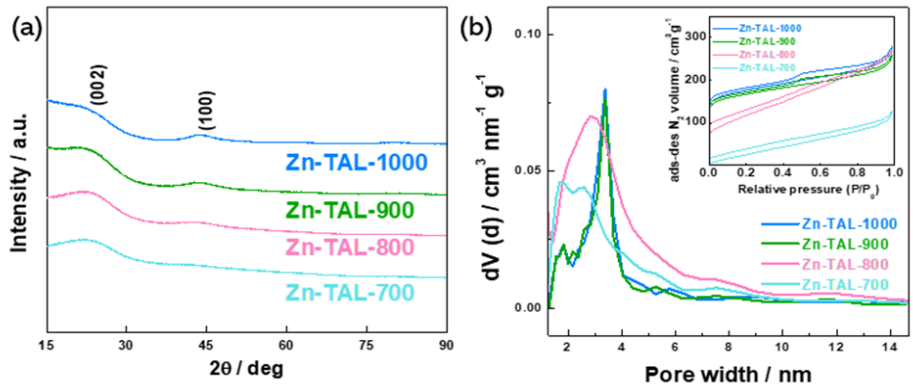

Figure 19. (a) X-ray diffraction patterns, (b) pore size distribution curves, and (inset) nitrogen adsorption–desorption isotherms for Zn-TAL samples [149]

N_2 physisorption analysis (Figure 19b) was used to determine specific surface area and pore size distribution of the synthesized electrocatalysts. All samples showed Type-IV isotherms with H4 hysteresis loops at $P/P_0 > 0.4$, indicating the presence of micro- and mesopores [152]. As pyrolysis temperature increased, a sharper N_2 uptake at low relative pressures was observed. Pore size distribution confirmed dominant microporosity and mesopores mainly between 3-4 nm. Zinc acted as a morphology-directing agent during pyrolysis [153,154], with specific surface area increasing significantly from 100 to 746 $m^2 g^{-1}$. This enhanced porosity contributed to more active sites, boosting the ORR performance. Key parameters (S_{DFT}, V_μ, V_{tot}) are listed in Table 6.

Table 6. Textural properties of Zn-TAL-derived samples.

Electrocatalyst	S_{BET} ($m^2 g^{-1}$)	S_{DFT} ($m^2 g^{-1}$)	V_{tot} ($cm^3 g^{-1}$)	V_μ ($cm^3 g^{-1}$)
Zn-TAL-700	103	100	0.17	0.03
Zn-TAL-800	414	475	0.40	0.14
Zn-TAL-900	584	715	0.37	0.23
Zn-TAL-1000	615	746	0.40	0.24

XPS analysis (Figure 20a) confirmed the presence of C, N, O, and Zn on the surface of all electrocatalysts, indicating incomplete Zn evaporation during pyrolysis. As shown in Table 7, surface Zn content decreased from 9.53 to 0.44 at.% with increasing pyrolysis temperature (700-1000 °C). Chlorine residues were

detected at 700 and 800 °C but disappeared at higher temperatures. Surface carbon content increased steadily, reaching 94.37 at.% at 1000 °C, indicating enhanced graphitization and potential for improved catalyst stability.

Deconvoluted N 1s spectra (Figures 20b) showed pyridinic (398.3 eV), pyrrolic (400.6 eV), graphitic (401.8 eV), oxidized (403.7 eV), and M-N_x (399.6 eV) nitrogen species.

Structural transformations in the carbon matrix were supported by XRD analysis, where a rise in the (1 0 0) peak and drop in (0 0 2) intensity reflected enhanced graphitization and disorder from nitrogen doping. This dual effect improves electrical conductivity, stability, and active site exposure, key for electrocatalytic performance.

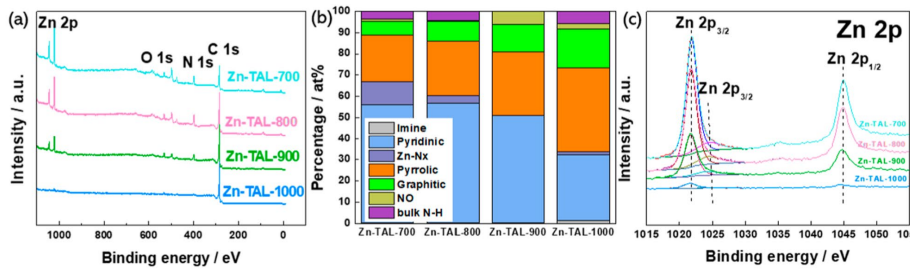

Figure 20. (a) XPS survey spectra obtained for Zn-TAL derived electrocatalysts; (b) the bar plot of the various types of nitrogen species and their atomic percentage; (c) Deconvoluted Zn 2p XPS spectra of Zn-TAL-700, Zn-TAL-800, Zn-TAL-900, and Zn-TAL-1000 samples [149].

The M-N_x XPS peak at 398.95 eV was detected only in samples pyrolyzed at 700, 800, and 1000 °C, with its surface content decreasing from 1.7 at. % to 0.04 at. % at 1000 °C. At 700-800 °C, pyridinic nitrogen dominated (~56%), but at 1000 °C, it dropped to 31%, while pyrrolic nitrogen increased from 22% to 39% (Figure 20b). Pyridinic and M-N_x species are recognized as ORR active sites [155], and studies show pyridinic and graphitic N contribute ~50% and 30% of the ORR activity, respectively [156,157].

Table 7. Surface elemental composition of Zn-TAL-700, Zn-TAL-800, Zn-TAL-900, and Zn-TAL-1000 samples (at. %) obtained from XPS analysis [149].

Electrocatalyst	C	N	O	Cl	Zn
Zn-TAL-700	68.52	94.37	5.3	1.25	9.53
Zn-TAL-800	76.66	12.82	4.42	0.42	5.68
Zn-TAL-900	85.54	8.38	3.53	0	2.55
Zn-TAL-1000	94.37	2.96	2.22	0	0.44

In Zn-TAL-900, Zn-N_x species were absent despite 2.55 at.% Zn. This may be due to Zn forming ZnO or Zn-O-N species at 900 °C, supported by the observed NO-related nitrogen peaks. Zn likely interacts with residual oxygen or matrix defects, preventing stable Zn-N_x formation. At this temperature, Zn-N_x sites may begin to destabilize before Zn evaporation becomes significant at 1000 °C.

High-resolution Zn 2p XPS spectra (Figure 20c) showed spin–orbit splitting (~23 eV) with $2p_{3/2}$ at 1021.9 eV and $2p_{1/2}$ at 1045 eV. As pyrolysis temperature increased, Zn surface content declined, aligning with MP-AES results. Zn-TAL-1000 had the lowest Zn content (0.23 wt%) compared to Zn-TAL-700, -800, and -900 (1.43, 1.10, and 0.58 wt%, respectively). This Zn loss trend was consistently observed across EDS, XPS, and MP-AES, reflecting their different analysis depths.

7.3.2 Electrocatalytic activity of TAL-derived Zn-N-C catalysts

The ORR activity of the synthesized electrocatalysts was evaluated against commercial Pt/C. Cyclic voltammetry in 0.1 M KOH (Ar or O_2-saturated, 10 mV s^{-1}) revealed clear ORR peaks for all samples, with the reduction peak shifting to 0.84 V vs RHE as pyrolysis temperature increased from 700 °C to 1000 °C, indicating improved electrocatalytic performance (Figure 21).

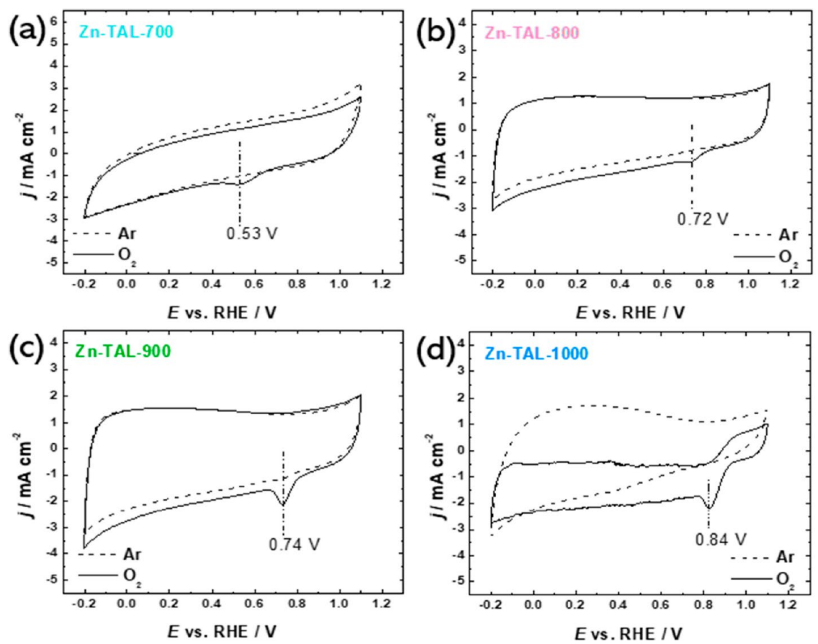

Figure 21. CV curves recorded for (a) Zn-TAL-700, (b) Zn-TAL-800, (c) Zn-TAL-900, and (d) Zn-TAL-1000 catalysts in Ar- (dashed line) and O_2-saturated (solid line) 0.1 M KOH [149].

To assess catalyst activity, the electrochemical active surface area (ECSA) was estimated by measuring the double-layer capacitance (C_{dl}) from CV scans at different sweep rates (40-200 mV s^{-1}) in an argon-saturated electrolyte at non-Faradaic potentials (0.92-1.00 V vs RHE). C_{dl} was determined from the slope of current density vs. scan rate (Figure 22e), and ECSA was calculated using the equation ECSA = C_{dl} / C_s, with C_s = 0.040 mF cm^{-2}. Zn-TAL-1000 showed the highest ECSA (57.5 cm^2), followed by Zn-TAL-900 (52.5 cm^2), Zn-TAL-700 (12.5 cm^2), and Zn-TAL-800 (10 cm^2), reflecting differences in porosity and active site accessibility.

Rotating disk electrode (RDE) tests confirmed that Zn-TAL-1000 exhibited superior ORR activity, with an onset potential of 0.98 V and a half-wave potential of 0.84 V – only 10 mV below Pt/C (Figure 22a) (Table 8). Tafel slopes (~61 mV dec^{-1}) and a high limiting current density of 5.15 mA cm^{-2} further supported this performance (Figure 22b). Koutecky–Levich plots derived from RDE polarization curves at various rotation rates (Figure 22c,d) showed good linearity, suggesting the first-order kinetics. The electron transfer number (n) was ~3.5, close to Pt/C's 4.0, indicating a dominant four-electron ORR pathway.

Table 8. ORR parameters obtained for Zn-N-C and Pt/C catalysts in 0.1 M KOH.

Electrocatalyst	$E_{1/2}$ (V)	E_{on} (V)	n	Tafel slope (mV dec^{-1})	C_{dl} (mF cm^{-2})	ECSA (cm^2)
Zn-TAL-700	0.64	0.76	1.12	-64	0.5	12.5
Zn-TAL-800	0.73	0.82	2.37	-53	0.4	10
Zn-TAL-900	0.79	0.89	2.46	-51	2.1	52.5
Zn-TAL-1000	0.84	0.98	3.45	-53	2.3	57.5
Pt/C	0.85	0.98	4.00	-61	N/A	N/A

The high ORR activity of Zn-TAL-1000 is attributed to its N-doped carbon matrix, atomically dispersed Zn, and hierarchical porosity, which enhance both intrinsic electrocatalytic activity and mass transport. XPS analysis confirmed the presence of pyridinic, pyrrolic, and graphitic N, especially pyridinic N, known for ORR activity [66,158,159]. Zn likely contributes through Zn-N_x and Zn-N_4-O sites, which facilitate *OH adsorption and lower reaction barriers [102,160]. High-temperature pyrolysis promotes Zn evaporation, forming porous structures, while residual Zn at lower temperatures may exist as ZnO or Zn-O-N (e.g., in Zn-TAL-900), potentially reducing electrocatalytic activity [161].

Stability tests over 5000 potential cycles (0.6-1.0 V vs RHE, 50 mV s^{-1}, 0.1 M KOH, O_2-saturated) showed Zn-TAL-1000 retained ORR activity (Figure 22f), supporting Zn site stability, as predicted by DFT studies citing strong Zn binding energies and N-induced electron withdrawal effects [162].

In AEMFC testing at 60 °C with a PtRu/C anode, the Zn-TAL-1000 cathode achieved a peak power density of 553 mW cm^{-2} and current density of ~1500 mA cm^{-2} (Figure 23), highlighting its promise for fuel cell applications.

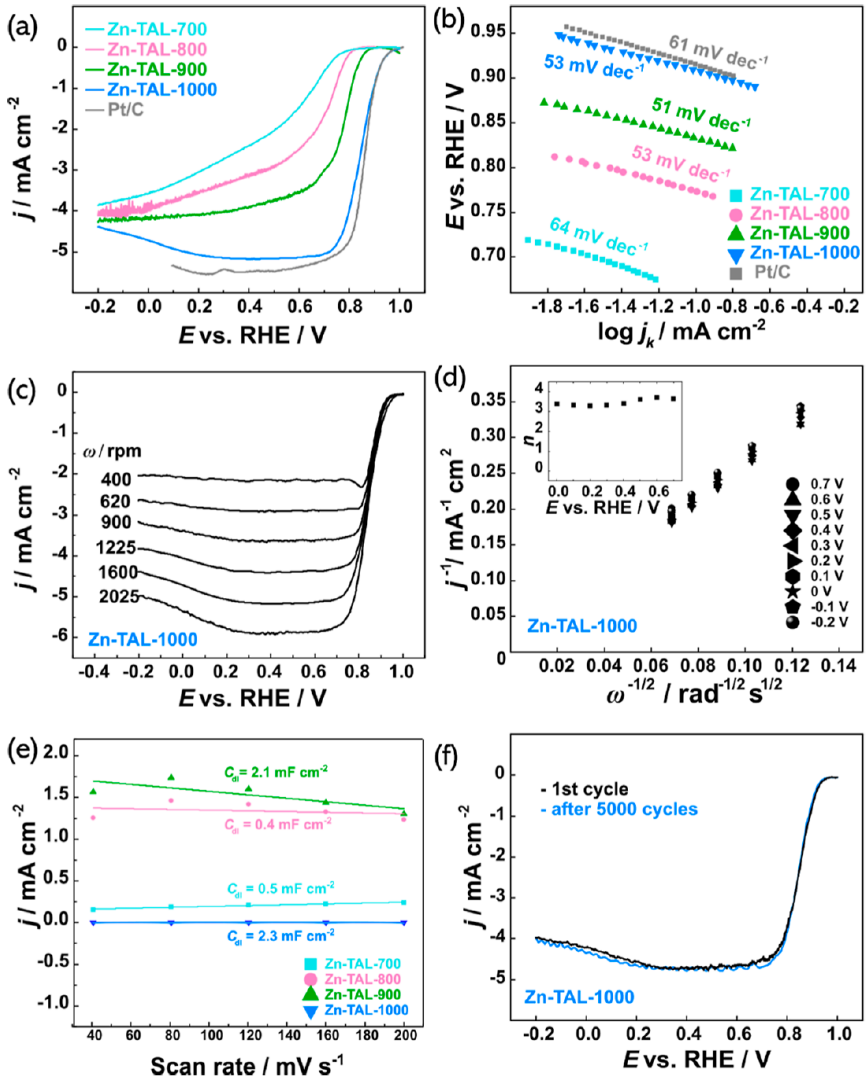

Figure 22. (a) ORR polarization curves comparing all Zn-TAL-derived catalysts with commercial Pt/C in O_2-saturated 0.1 M KOH at 1600 rpm; (b) ORR Tafel plots derived from RDE data; (c) ORR polarization curves recorded for Zn-TAL-1000 at various electrode rotation speeds; (d) Koutecky-Levich plots constructed from Zn-TAL-1000 RDE data (inset: calculated electron transfer number, *n*); (e) Charging current density versus scan rate plots for all Zn-TAL samples; (f) ORR polarization curves for Zn-TAL-1000 before and after 5000 potential cycles between 0.6 and 1.0 V vs. RHE in O_2-saturated 0.1 M KOH at a scan rate of 10 mV s^{-1} and electrode rotation speed of 1600 rpm [149].

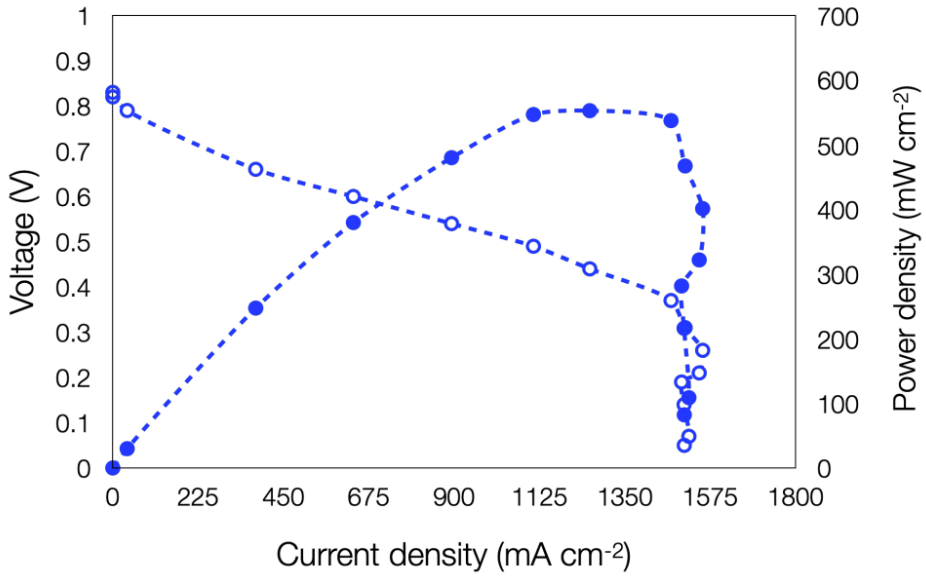

Figure 23. Polarization curve (empty symbols, Y1 axis) and power density curve (filled symbols, Y2 axis) of an H_2-O_2 AEMFC with Zn-TAL-1000 cathode catalyst [149].

8. SUMMARY

In response to the growing need for sustainable energy storage and conversion technologies, this thesis has explored the development of efficient, cost-effective, and scalable electrocatalysts derived from metal-organic frameworks (MOFs) for use in next-generation polymer electrolyte fuel cells (FCs) and metal–air batteries (MABs). These technologies rely heavily on the oxygen reduction reaction (ORR) and the oxygen evolution reaction (OER), whose sluggish kinetics present a key bottleneck. To address this, we focused on developing platinum-group metal (PGM)-free electrocatalysts based on transition metal–nitrogen–carbon (M–N–C) materials. A novel family of MOFs, referred to as TAL (TalTech–UniTartu Alliance Laboratory), was central to this work. These materials were specifically designed within our research group to serve as tunable and multifunctional precursors for M–N–C catalysts. By varying the metal centers (Co, Mn, Zn) and synthetic protocols, the TAL series enabled systematic control over porosity, electronic structure, and nitrogen coordination, allowing us to tailor catalyst properties at the molecular level. Through a combination of strategic synthesis, pyrolysis optimization, and post-synthetic treatments, we successfully developed Co–N–C, MnCo–N–C, and Zn–N–C catalysts with high ORR and OER activity in alkaline media. Co–N–C catalysts derived from TAL-2 showed bifunctional activity strongly influenced by pyrolysis temperature and acid-leaching, with Co-700L5 and Co-900L5 achieving low ΔE values and optimal structural features. The Mn/Co bimetallic system (TAL-42-900) benefited from synergistic interactions, high mesoporosity, and well-dispersed M–N_x active sites, leading to exceptional performance in both half-cell and zinc–air battery configurations. The Zn–N–C catalyst retained its hollow, porous morphology after pyrolysis, delivering a half-wave potential ($E_{1/2}$) of 0.84 V vs. RHE for ORR, comparable to commercial Pt/C, and demonstrated high durability and performance in an anion-exchange membrane fuel cell (AEMFC), achieving power densities above 550 mW cm^{-2}. Overall, this thesis establishes the TAL MOF series as a flexible platform for the rational design of high-performance M–N–C catalysts. The insights gained into structure–activity relationships, active site formation, and electrocatalytic mechanisms provide a strong foundation for further development of PGM-free catalyst materials. Results of this work contribute to the transition toward clean and efficient electrochemical energy systems by advancing the practical applicability of MOF-derived electrocatalysts in renewable energy storage and conversion devices.

9. REFERENCES

[1] H. Nazir, N. Muthuswamy, C. Louis, S. Jose, J. Prakash, M.E.M. Buan, C. Flox, S. Chavan, X. Shi, P. Kauranen, T. Kallio, G. Maia, K. Tammeveski, N. Lymperopoulos, E. Carcadea, E. Veziroglu, A. Iranzo, A.M. Kannan, Is the H2 economy realizable in the foreseeable future? Part III: H2 usage technologies, applications, and challenges and opportunities, International Journal of Hydrogen Energy 45 (2020) 28217–28239. https://doi.org/10.1016/j.ijhydene.2020.07.256.

[2] I. Staffell, D. Scamman, A.V. Abad, P. Balcombe, P.E. Dodds, P. Ekins, N. Shah, K.R. Ward, The role of hydrogen and fuel cells in the global energy system, Energy Environmental Science 12 (2019) 463–491. https://doi.org/10.1039/C8EE01157E.

[3] W.F. Pickard, A.Q. Shen, N.J. Hansing, Parking the power: Strategies and physical limitations for bulk energy storage in supply–demand matching on a grid whose input power is provided by intermittent sources, Renewable and Sustainable Energy Reviews 13 (2009) 1934–1945. https://doi.org/10.1016/j.rser.2009.03.002.

[4] H.A. Firouzjaie, W.E. Mustain, Catalytic Advantages, Challenges, and Priorities in Alkaline Membrane Fuel Cells, ACS Catalysis 10 (2020) 225–234. https://doi.org/10.1021/acscatal.9b03892.

[5] J. Fu, R. Liang, G. Liu, A. Yu, Z. Bai, L. Yang, Z. Chen, Recent Progress in Electrically Rechargeable Zinc–Air Batteries, Advanced Materials 31 (2019) 1805230. https://doi.org/10.1002/adma.201805230.

[6] R. Othman, A.L. Dicks, Z. Zhu, Non precious metal catalysts for the PEM fuel cell cathode, International Journal of Hydrogen Energy 37 (2012) 357–372. https://doi.org/10.1016/j.ijhydene.2011.08.095.

[7] Y. Liu, X. Yue, K. Li, J. Qiao, D.P. Wilkinson, J. Zhang, PEM fuel cell electrocatalysts based on transition metal macrocyclic compounds, Coordination Chemistry Reviews 315 (2016) 153–177. https://doi.org/10.1016/j.ccr.2016.02.002.

[8] Y. Kumar, M. Mooste, K. Tammeveski, Recent progress of transition metal-based bifunctional electrocatalysts for rechargeable zinc–air battery application, Current Opinion in Electrochemistry 38 (2023) 101229. https://doi.org/10.1016/j.coelec.2023.101229.

[9] Md.M. Hossen, Md.S. Hasan, Md.R.I. Sardar, J. bin Haider, Mottakin, K. Tammeveski, P. Atanassov, State-of-the-art and developmental trends in platinum group metal-free cathode catalyst for anion exchange membrane fuel cell (AEMFC), Applied Catalysis B: Environmental 325 (2023) 121733. https://doi.org/10.1016/j.apcatb.2022.121733.

[10] A. Sarapuu, J. Lilloja, S. Akula, J.H. Zagal, S. Specchia, K. Tammeveski, Recent Advances in Non-Precious Metal Single-Atom Electrocatalysts for Oxygen Reduction Reaction in Low-Temperature Polymer-Electrolyte Fuel Cells, Chem CatChem 15 (2023) e202300849. https://doi.org/10.1002/cctc.202300849.

[11] M. Luo, W. Sun, B.B. Xu, H. Pan, Y. Jiang, Interface Engineering of Air Electrocatalysts for Rechargeable Zinc–Air Batteries, Advanced Energy Materials 11 (2021) 2002762. https://doi.org/10.1002/aenm.202002762.

[12] X. Ren, Q. Lv, L. Liu, B. Liu, Y. Wang, A. Liu, G. Wu, Current progress of Pt and Pt-based electrocatalysts used for fuel cells, Sustainable Energy & Fuels 4 (2020) 15–30. https://doi.org/10.1039/C9SE00460B.

[13] Q. Shi, C. Zhu, D. Du, Y. Lin, Robust noble metal-based electrocatalysts for oxygen evolution reaction, Chemical Society Reviews 48 (2019) 3181–3192. https://doi.org/10.1039/C8CS00671G.

[14] L. Du, L. Xing, G. Zhang, S. Sun, Metal-organic framework derived carbon materials for electrocatalytic oxygen reactions: Recent progress and future perspectives, Carbon 156 (2020) 77–92. https://doi.org/10.1016/j.carbon.2019.09.029.
[15] K. Ping, R. Bhadoria, P. Starkov, N. Kongi, M–N–C materials as heterogeneous catalysts for organic transformations, Coordination Chemistry Reviews 497 (2023) 215412. https://doi.org/10.1016/j.ccr.2023.215412.
[16] Q.H. Nguyen, V.D.C. Tinh, S. Oh, T.M. Pham, T.N. Tu, D. Kim, J. Han, K. Im, J. Kim, Metal-organic framework-polymer complex-derived single-atomic oxygen reduction catalyst for anion exchange membrane fuel cells, Chemical Engineering Journal 481 (2024) 148508. https://doi.org/10.1016/j.cej.2023.148508.
[17] A. Kosimov, G. Yusibova, J. Aruväli, P. Paiste, M. Käärik, J. Leis, A. Kikas, V. Kisand, K. Šmits, N. Kongi, Liquid-assisted grinding/compression: a facile mechanosynthetic route for the production of high-performing Co–N–C electrocatalyst materials, Green Chemistry 24 (2022) 305–314. https://doi.org/10.1039/D1GC03433B.
[18] J. Lilloja, E. Kibena-Põldsepp, A. Sarapuu, A. Konovalova, M. Käärik, J. Kozlova, P. Paiste, A. Kikas, A. Treshchalov, J. Aruväli, A. Zitolo, J. Leis, A. Tamm, V. Kisand, S. Holdcroft, K. Tammeveski, Transition-Metal and Nitrogen-Doped Carbon Nanotube/Graphene Composites as Cathode Catalysts for Anion-Exchange Membrane Fuel Cells, ACS Applied Energy Materials 6 (2023) 5519–5529. https://doi.org/10.1021/acsaem.3c00613.
[19] S. Akula, M. Mooste, J. Kozlova, M. Käärik, A. Treshchalov, A. Kikas, V. Kisand, J. Aruväli, P. Paiste, A. Tamm, J. Leis, K. Tammeveski, Transition metal (Fe, Co, Mn, Cu) containing nitrogen-doped porous carbon as efficient oxygen reduction electrocatalysts for anion exchange membrane fuel cells, Chemical Engineering Journal 458 (2023) 141468. https://doi.org/10.1016/j.cej.2023.141468.
[20] D. Chen, J. Yu, Z. Cui, Q. Zhang, X. Chen, J. Sui, H. Dong, L. Yu, L. Dong, Hierarchical architecture derived from two-dimensional zeolitic imidazolate frameworks as an efficient metal-based bifunctional oxygen electrocatalyst for rechargeable Zn–air batteries, Electrochimica Acta 331 (2020) 135394. https:// doi.org/10.1016/j.electacta.2019.135394.
[21] W. Zhang, X. Yao, S. Zhou, X. Li, L. Li, Z. Yu, L. Gu, ZIF-8/ZIF-67-Derived Co-Nx-Embedded 1D Porous Carbon Nanofibers with Graphitic Carbon-Encased Co Nanoparticles as an Efficient Bifunctional Electrocatalyst, Small 14 (2018) 1800423. https://doi.org/10.1002/smll.201800423.
[22] R. Cepitis, N. Kongi, V. Grozovski, V. Ivanistsev, E. Lust, Multifunctional Electrocatalysis on Single-Site Metal Catalysts: A Computational Perspective, Catalysts 11 (2021) 1165. https://doi.org/10.3390/catal11101165.
[23] M. Moharramnejad, M. Babazadeh, A. Ehsani, S.M. Mahdian, MOF-derived carbon and transition metals as high efficient electrocatalysts and active materials in energy storage devices: an introduction and review to it in recent studies, Inorganic and Nano-Metal Chemistry 0 (2023) 1–34. https://doi.org/10.1080/24701556.2023.2267538.
[24] O.V. Kharissova, B.I. Kharisov, I.E. Ulyand, T.H. García, Catalysis using metal–organic framework-derived nanocarbons: Recent trends, Journal of Materials Research 35 (2020) 2190–2207. https://doi.org/10.1557/jmr.2020.166.
[25] H.D. Abruña, Energy in the Age of Sustainability, J. Chem. Educ. 90 (2013) 1411–1413. https://doi.org/10.1021/ed400673m.
[26] B. Pivovar, Catalysts for fuel cell transportation and hydrogen related uses, Nature Catalysis 2 (2019) 562–565. https://doi.org/10.1038/s41929-019-0320-9.

[27] C. Song, J. Zhang, Electrocatalytic Oxygen Reduction Reaction, in: J. Zhang (Ed.), PEM Fuel Cell Electrocatalysts and Catalyst Layers: Fundamentals and Applications, Springer, London, 2008: pp. 89–134. https://doi.org/10.1007/978-1-84800-936-3_2.

[28] M.K. Singla, P. Nijhawan, A.S. Oberoi, Hydrogen fuel and fuel cell technology for cleaner future: a review, Environmental Science and Pollution Research 28 (2021) 15607–15626. https://doi.org/10.1007/s11356-020-12231-8.

[29] N. Ramaswamy, S. Mukerjee, Alkaline Anion-Exchange Membrane Fuel Cells: Challenges in Electrocatalysis and Interfacial Charge Transfer, Chemical Reviews 119 (2019) 11945–11979. https://doi.org/10.1021/acs.chemrev.9b00157.

[30] P.A. Christensen, A. Hamnett, D. Linares-Moya, Oxygen reduction and fuel oxidation in alkaline solution, Physical Chemistry Chemical Physics 13 (2011) 5206–5214. https://doi.org/10.1039/C0CP02365E.

[31] Y. Yang, C.R. Peltier, R. Zeng, R. Schimmenti, Q. Li, X. Huang, Z. Yan, G. Potsi, R. Selhorst, X. Lu, W. Xu, M. Tader, A.V. Soudackov, H. Zhang, M. Krumov, E. Murray, P. Xu, J. Hitt, L. Xu, H.-Y. Ko, B.G. Ernst, C. Bundschu, A. Luo, D. Markovich, M. Hu, C. He, H. Wang, J. Fang, R.A.Jr. DiStasio, L.F. Kourkoutis, A. Singer, K.J.T. Noonan, L. Xiao, L. Zhuang, B.S. Pivovar, P. Zelenay, E. Herrero, J.M. Feliu, J. Suntivich, E.P. Giannelis, S. Hammes-Schiffer, T. Arias, M. Mavrikakis, T.E. Mallouk, J.D. Brock, D.A. Muller, F.J. DiSalvo, G.W. Coates, H.D. Abruña, Electrocatalysis in Alkaline Media and Alkaline Membrane-Based Energy Technologies, Chemical Reviews 122 (2022) 6117–6321. https://doi.org/10.1021/acs.chemrev.1c00331.

[32] T. Noor, L. Yaqoob, N. Iqbal, Recent Advances in Electrocatalysis of Oxygen Evolution Reaction using Noble-Metal, Transition-Metal, and Carbon-Based Materials, ChemElectroChem 8 (2021) 447–483. https://doi.org/10.1002/celc.202001441.

[33] K. Zhang, R. Zou, Advanced Transition Metal-Based OER Electrocatalysts: Current Status, Opportunities, and Challenges, Small 17 (2021) 2100129. https://doi.org/10.1002/smll.202100129.

[34] N.-T. Suen, S.-F. Hung, Q. Quan, N. Zhang, Y.-J. Xu, H.M. Chen, Electrocatalysis for the oxygen evolution reaction: recent development and future perspectives, Chemical Society Reviews 46 (2017) 337–365. https://doi.org/10.1039/C6CS00328A.

[35] X. Cao, Y. Gao, Y. Li, D.M. Weragoda, G. Tian, W. Zhang, Z. Zhang, X. Zhao, B. Chen, Research progress on MOFs and their derivatives as promising and efficient electrode materials for electrocatalytic hydrogen production from water, RSC Advances 13 (2023) 24393–24411. https://doi.org/10.1039/D3RA04110G.

[36] A. Damjanovic, B. Jovanovic, Anodic Oxide Films as Barriers to Charge Transfer in O 2 Evolution at Pt in Acid Solutions, Journal of The Electrochemical Society 123 (1976) 374. https://doi.org/10.1149/1.2132828.

[37] T. Binninger, R. Mohamed, K. Waltar, E. Fabbri, P. Levecque, R. Kötz, T.J. Schmidt, Thermodynamic explanation of the universal correlation between oxygen evolution activity and corrosion of oxide catalysts, Scientific Reports 5 (2015) 12167. https://doi.org/10.1038/srep12167.

[38] F. Xiao, Y.-C. Wang, Z.-P. Wu, G. Chen, F. Yang, S. Zhu, K. Siddharth, Z. Kong, A. Lu, J.-C. Li, C.-J. Zhong, Z.-Y. Zhou, M. Shao, Recent Advances in Electrocatalysts for Proton Exchange Membrane Fuel Cells and Alkaline Membrane Fuel Cells, Advanced Materials 33 (2021) 2006292. https://doi.org/10.1002/adma.202006292.

[39] K. Jiao, J. Xuan, Q. Du, Z. Bao, B. Xie, B. Wang, Y. Zhao, L. Fan, H. Wang, Z. Hou, S. Huo, N.P. Brandon, Y. Yin, M.D. Guiver, Designing the next generation of proton-exchange membrane fuel cells, Nature 595 (2021) 361–369. https://doi. org/10.1038/s41586-021-03482-7.

[40] B. Yang, Z. Cunman, Progress in constructing high-performance anion exchange Membrane: Molecular design, microphase controllability and In-device property, Chemical Engineering Journal 457 (2023) 141094. https://doi.org/10.1016/j.cej.2022.141094.

[41] M. Mandal, Recent Advancement on Anion Exchange Membranes for Fuel Cell and Water Electrolysis, ChemElectroChem 8 (2021) 36–45. https://doi.org/10.1002/celc.202001329.

[42] N. Chen, Y.M. Lee, Anion exchange polyelectrolytes for membranes and ionomers, Progress in Polymer Science 113 (2021) 101345. https://doi.org/10.1016/j.progpolymsci.2020.101345.

[43] P.C. Okonkwo, O.O. Ige, E.M. Barhoumi, P.C. Uzoma, W. Emori, A. Benamor, A.M. Abdullah, Platinum degradation mechanisms in proton exchange membrane fuel cell (PEMFC) system: A review, International Journal of Hydrogen Energy 46 (2021) 15850–15865. https://doi.org/10.1016/j.ijhydene.2021.02.078.

[44] J. Cui, Q. Chen, X. Li, S. Zhang, Recent advances in non-precious metal electrocatalysts for oxygen reduction in acidic media and PEMFCs: an activity, stability and mechanism study, Green Chemistry 23 (2021) 6898–6925. https://doi.org/10.1039/D1GC01040A.

[45] M. Hren, M. Božič, D. Fakin, K.S. Kleinschek, S. Gorgieva, Alkaline membrane fuel cells: anion exchange membranes and fuels, Sustainable Energy Fuels 5 (2021) 604–637. https://doi.org/10.1039/D0SE01373K.

[46] J. Zhang, W. Zhu, T. Huang, C. Zheng, Y. Pei, G. Shen, Z. Nie, D. Xiao, Y. Yin, M.D. Guiver, Recent Insights on Catalyst Layers for Anion Exchange Membrane Fuel Cells, Advanced Science 8 (2021) 2100284. https://doi.org/10.1002/advs.202100284.

[47] J. Masa, W. Xia, M. Muhler, W. Schuhmann, On the Role of Metals in Nitrogen-Doped Carbon Electrocatalysts for Oxygen Reduction, Angewandte Chemie International Edition 54 (2015) 10102–10120. https://doi.org/10.1002/anie.201500569.

[48] C. Zúñiga, C. Candia-Onfray, R. Venegas, K. Muñoz, J. Urra, M. Sánchez-Arenillas, J.F. Marco, J.H. Zagal, F.J. Recio, Elucidating the mechanism of the oxygen reduction reaction for pyrolyzed Fe-N-C catalysts in basic media, Electrochemistry Communications 102 (2019) 78–82. https://doi.org/10.1016/j.elecom.2019.04.005.

[49] R. Gutru, Z. Turtayeva, F. Xu, G. Maranzana, B. Vigolo, A. Desforges, A comprehensive review on water management strategies and developments in anion exchange membrane fuel cells, International Journal of Hydrogen Energy 45 (2020) 19642–19663. https://doi.org/10.1016/j.ijhydene.2020.05.026.

[50] W.E. Mustain, Understanding how high-performance anion exchange membrane fuel cells were achieved: Component, interfacial, and cell-level factors, Current Opinion in Electrochemistry 12 (2018) 233–239. https://doi.org/10.1016/j.coelec.2018.11.010.

[51] Louis maiche, US243454A, 1881. https://patents.google.com/patent/US243454A/en (accessed April 1, 2025).

[52] J.-N. Liu, C.-X. Zhao, J. Wang, D. Ren, B.-Q. Li, Q. Zhang, A brief history of zinc–air batteries: 140 years of epic adventures, Energy Environmental Science 15 (2022) 4542–4553. https://doi.org/10.1039/D2EE02440C.

[53] J. Pan, Y.Y. Xu, H. Yang, Z. Dong, H. Liu, B.Y. Xia, Advanced Architectures and Relatives of Air Electrodes in Zn–Air Batteries, Advanced Science 5 (2018) 1700691. https://doi.org/10.1002/advs.201700691.

[54] L. Wei, E.H. Ang, Y. Yang, Y. Qin, Y. Zhang, M. Ye, Q. Liu, C.C. Li, Recent advances of transition metal based bifunctional electrocatalysts for rechargeable zinc-air batteries, Journal of Power Sources 477 (2020) 228696. https://doi.org/10.1016/j.jpowsour.2020.228696.

[55] K.W. Leong, Y. Wang, M. Ni, W. Pan, S. Luo, D.Y.C. Leung, Rechargeable Zn-air batteries: Recent trends and future perspectives, Renewable and Sustainable Energy Reviews 154 (2022) 111771. https://doi.org/10.1016/j.rser.2021.111771.

[56] M.T. Tsehaye, F. Alloin, C. Iojoiu, R.A. Tufa, D. Aili, P. Fischer, S. Velizarov, Membranes for zinc-air batteries: Recent progress, challenges and perspectives, Journal of Power Sources 475 (2020) 228689. https://doi.org/10.1016/j.jpowsour.2020.228689.

[57] W. Shao, R. Yan, M. Zhou, L. Ma, C. Roth, T. Ma, S. Cao, C. Cheng, B. Yin, S. Li, Carbon-Based Electrodes for Advanced Zinc-Air Batteries: Oxygen-Catalytic Site Regulation and Nanostructure Design, Electrochemical Energy Reviews 6 (2023) 11. https://doi.org/10.1007/s41918-023-00181-x.

[58] G. Nazir, A. Rehman, J.-H. Lee, C.-H. Kim, J. Gautam, K. Heo, S. Hussain, M. Ikram, A.A. AlObaid, S.-Y. Lee, S.-J. Park, A Review of Rechargeable Zinc–Air Batteries: Recent Progress and Future Perspectives, Nano-Micro Letters 16 (2024) 138. https://doi.org/10.1007/s40820-024-01328-1.

[59] Y. Wang, X. Zheng, D. Wang, Design concept for electrocatalysts, Nano Research 15 (2022) 1730–1752. https://doi.org/10.1007/s12274-021-3794-0.

[60] K. Zeng, X. Zheng, C. Li, J. Yan, J.-H. Tian, C. Jin, P. Strasser, R. Yang, Recent Advances in Non-Noble Bifunctional Oxygen Electrocatalysts toward Large-Scale Production, Advanced Functional Materials 30 (2020) 2000503. https://doi.org/10.1002/adfm.202000503.

[61] C.-X. Zhao, B.-Q. Li, J.-N. Liu, Q. Zhang, Intrinsic Electrocatalytic Activity Regulation of M–N–C Single-Atom Catalysts for the Oxygen Reduction Reaction, Angewandte Chemie International Edition 60 (2021) 4448–4463. https://doi.org/10.1002/anie.202003917.

[62] W.-C. Chen, G. Yang, Y. Zhao, G.-Q. Yuan, J.-S. Ye, H.-Y. Liu, X.-Y. Xiao, Porous carbon polyhedrons with exclusive Metal-NX moieties for efficient oxygen reduction reaction, International Journal of Hydrogen Energy 46 (2021) 39882–39891. https://doi.org/10.1016/j.ijhydene.2021.09.244.

[63] Z. Shi, W. Yang, Y. Gu, T. Liao, Z. Sun, Metal-Nitrogen-Doped Carbon Materials as Highly Efficient Catalysts: Progress and Rational Design, Advanced Science 7 (2020) 2001069. https://doi.org/10.1002/advs.202001069.

[64] Q. Cheng, H. Ding, L. Chen, J. Dong, H. Yu, S. Yan, H. Wang, Modification of NiSe2 Nanoparticles by ZIF-8-Derived NC for Boosting H2O2 Production from Electrochemical Oxygen Reduction in Acidic Media, Catalysts 14 (2024) 364. https://doi.org/10.3390/catal14060364.

[65] S. Kattel, P. Atanassov, B. Kiefer, Catalytic activity of Co–Nx/C electrocatalysts for oxygen reduction reaction: a density functional theory study, Physical Chemistry Chemical Physics 15 (2012) 148–153. https://doi.org/10.1039/C2CP42609A.

[66] M. Skorupska, A. Ilnicka, J.P. Lukaszewicz, The effect of nitrogen species on the catalytic properties of N-doped graphene, Scientific Reports 11 (2021) 23970. https://doi.org/10.1038/s41598-021-03403-8.

[67] X. Ning, Y. Li, J. Ming, Q. Wang, H. Wang, Y. Cao, F. Peng, Y. Yang, H. Yu, Electronic synergism of pyridinic- and graphitic-nitrogen on N-doped carbons for the oxygen reduction reaction, Chemical Science 10 (2019) 1589–1596. https://doi.org/10.1039/C8SC04596H.

[68] M. Zerner, M. Gouterman, Porphyrins, Theoretica Chimica Acta 4 (1966) 44–63. https://doi.org/10.1007/BF00526010.

[69] L. Osmieri, A.H.A. Monteverde Videla, P. Ocón, S. Specchia, Kinetics of Oxygen Electroreduction on Me–N–C (Me = Fe, Co, Cu) Catalysts in Acidic Medium: Insights on the Effect of the Transition Metal, Journal of Physical Chemistry C 121 (2017) 17796–17817. https://doi.org/10.1021/acs.jpcc.7b02455.

[70] A. Kumar, S. Ibraheem, T. Anh Nguyen, R.K. Gupta, T. Maiyalagan, G. Yasin, Molecular-MN4 vs atomically dispersed M−N4−C electrocatalysts for oxygen reduction reaction, Coordination Chemistry Reviews 446 (2021) 214122. https://doi.org/10.1016/j.ccr.2021.214122.

[71] P. Song, Y. Zhang, J. Pan, L. Zhuang, W. Xu, Cheap carbon black-based high-performance electrocatalysts for oxygen reduction reaction, Chemical Communications 51 (2015) 1972–1975. https://doi.org/10.1039/C4CC07677J.

[72] H. Ren, Y. Wang, Y. Yang, X. Tang, Y. Peng, H. Peng, L. Xiao, J. Lu, H.D. Abruña, L. Zhuang, Fe/N/C Nanotubes with Atomic Fe Sites: A Highly Active Cathode Catalyst for Alkaline Polymer Electrolyte Fuel Cells, ACS Catalysis 7 (2017) 6485–6492. https://doi.org/10.1021/acscatal.7b02340.

[73] K. Khan, A.K. Tareen, M. Aslam, Q. Khan, S.A. Khan, Q.U. Khan, A.S. Saleemi, R. Wang, Y. Zhang, Z. Guo, H. Zhang, Z. Ouyang, Novel Two-Dimensional Carbon–Chromium Nitride-Based Composite as an Electrocatalyst for Oxygen Reduction Reaction, Frontiers in Chemistry 7 (2019). https://doi.org/10.3389/fchem.2019.00738.

[74] J. Lilloja, E. Kibena-Põldsepp, A. Sarapuu, J.C. Douglin, M. Käärik, J. Kozlova, P. Paiste, A. Kikas, J. Aruväli, J. Leis, V. Sammelselg, D.R. Dekel, K. Tammeveski, Transition-Metal- and Nitrogen-Doped Carbide-Derived Carbon/Carbon Nanotube Composites as Cathode Catalysts for Anion-Exchange Membrane Fuel Cells, ACS Catalysis 11 (2021) 1920–1931. https://doi.org/10.1021/acscatal.0c03511.

[75] J. Woo, S.Y. Yang, Y.J. Sa, W.-Y. Choi, M.-H. Lee, H.-W. Lee, T.J. Shin, T.-Y. Kim, S.H. Joo, Promoting Oxygen Reduction Reaction Activity of Fe–N/C Electrocatalysts by Silica-Coating-Mediated Synthesis for Anion-Exchange Membrane Fuel Cells, Chemistry of Materials 30 (2018) 6684–6701. https://doi.org/10.1021/acs.chemmater.8b02117.

[76] A. Carlson, P. Shapturenka, B. Eriksson, G. Lindbergh, C. Lagergren, R. Wreland Lindström, Electrode parameters and operating conditions influencing the performance of anion exchange membrane fuel cells, Electrochimica Acta 277 (2018) 151–160. https://doi.org/10.1016/j.electacta.2018.04.137.

[77] X. Zhang, J. Luo, H.-F. Lin, P. Tang, J.R. Morante, J. Arbiol, K. Wan, B.-W. Mao, L.-M. Liu, J. Fransaer, Tailor-made metal-nitrogen-carbon bifunctional electrocatalysts for rechargeable Zn-air batteries via controllable MOF units, Energy Storage Materials 17 (2019) 46–61. https://doi.org/10.1016/j.ensm.2018.11.034.

[78] M. Zhang, Q. Dai, H. Zheng, M. Chen, L. Dai, Novel MOF-Derived Co@N-C Bifunctional Catalysts for Highly Efficient Zn–Air Batteries and Water Splitting, Advanced Materials 30 (2018) 1705431. https://doi.org/10.1002/adma.201705431.
[79] X. Duan, S. Ren, N. Pan, M. Zhang, H. Zheng, MOF-derived Fe,Co@N–C bi-functional oxygen electrocatalysts for Zn–air batteries, Journal of Materials Chemistry A 8 (2020) 9355–9363. https://doi.org/10.1039/D0TA02825H.
[80] H.-F. Wang, L. Chen, H. Pang, S. Kaskel, Q. Xu, MOF-derived electrocatalysts for oxygen reduction, oxygen evolution and hydrogen evolution reactions, Chemical Society Reviews 49 (2020) 1414–1448. https://doi.org/10.1039/C9CS00906J.
[81] Z. Song, L. Zhang, K. Doyle-Davis, X. Fu, J.-L. Luo, X. Sun, Recent Advances in MOF-Derived Single Atom Catalysts for Electrochemical Applications, Advanced Energy Materials 10 (2020) 2001561. https://doi.org/10.1002/aenm.202001561.
[82] Q. Wang, D. Astruc, State of the Art and Prospects in Metal–Organic Framework (MOF)-Based and MOF-Derived Nanocatalysis, Chemical Reviews 120 (2020) 1438–1511. https://doi.org/10.1021/acs.chemrev.9b00223.
[83] S. Chen, M. Cui, Z. Yin, J. Xiong, L. Mi, Y. Li, Single-Atom and Dual-Atom Electrocatalysts Derived from Metal Organic Frameworks: Current Progress and Perspectives, ChemSusChem 14 (2021) 73–93. https://doi.org/10.1002/cssc.202002098.
[84] H. Tang, S. Cai, S. Xie, Z. Wang, Y. Tong, M. Pan, X. Lu, Metal–Organic-Framework-Derived Dual Metal- and Nitrogen-Doped Carbon as Efficient and Robust Oxygen Reduction Reaction Catalysts for Microbial Fuel Cells, Advanced Science 3 (2016) 1500265. https://doi.org/10.1002/advs.201500265.
[85] T. Wang, Z. Kou, S. Mu, J. Liu, D. He, I.S. Amiinu, W. Meng, K. Zhou, Z. Luo, S. Chaemchuen, F. Verpoort, 2D Dual-Metal Zeolitic-Imidazolate-Framework-(ZIF)-Derived Bifunctional Air Electrodes with Ultrahigh Electrochemical Properties for Rechargeable Zinc–Air Batteries, Advanced Functional Materials 28 (2018) 1705048. https://doi.org/10.1002/adfm.201705048.
[86] Y. Huang, Y. Chen, M. Xu, A. Ly, A. Gili, E. Murphy, T. Asset, Y. Liu, V. De Andrade, C.U. Segre, A.L. Deriy, F. De Carlo, M. Kunz, A. Gurlo, X. Pan, P. Atanassov, I.V. Zenyuk, Catalysts by pyrolysis: Transforming metal-organic frameworks (MOFs) precursors into metal-nitrogen-carbon (M-N-C) materials, Materials Today 69 (2023) 66–78. https://doi.org/10.1016/j.mattod.2023.08.007.
[87] Y.-F. Xia, B. Liu, P. Guo, F.-D. Tu, L.-X. Shen, M. Ma, Y.-K. Dai, J. Liu, B. Xu, Y.-L. Zhang, L. Zhao, Y. Wang, Z.-B. Wang, Residual ZnNx moieties in ZIF-8 derived catalysts: Protective and synergistic effects for oxygen reduction, Journal of Catalysis 429 (2024) 115296. https://doi.org/10.1016/j.jcat.2024.115296.
[88] R. Cepitis, N. Kongi, J. Rossmeisl, V. Ivaništšev, Surface Curvature Effect on Dual-Atom Site Oxygen Electrocatalysis, ACS Energy Letters 8 (2023) 1330–1335. https://doi.org/10.1021/acsenergylett.3c00068.
[89] R. Cepitis, V. Ivaništšev, J. Rossmeisl, N. Kongi, Bypassing the scaling relations in oxygen electrocatalysis with geometry-adaptive catalysts, Catalysis Science and Technology 14 (2024) 2105–2113. https://doi.org/10.1039/D4CY00036F.
[90] J. Li, M. Chen, D.A. Cullen, S. Hwang, M. Wang, B. Li, K. Liu, S. Karakalos, M. Lucero, H. Zhang, C. Lei, H. Xu, G.E. Sterbinsky, Z. Feng, D. Su, K.L. More, G. Wang, Z. Wang, G. Wu, Atomically dispersed manganese catalysts for oxygen reduction in proton-exchange membrane fuel cells, Nature Catalysis 1 (2018) 935–945. https://doi.org/10.1038/s41929-018-0164-8.

[91] Y. Dessie, S. Tadesse, R. Eswaramoorthy, B. Abebe, Recent developments in manganese oxide based nanomaterials with oxygen reduction reaction functionalities for energy conversion and storage applications: A review, Journal of Science: Advanced Materials and Devices 4 (2019) 353–369. https://doi.org/10.1016/j.jsamd.2019.07.001.
[92] Q. Huang, X. Zhong, Q. Zhang, X. Wu, M. Jiao, B. Chen, J. Sheng, G. Zhou, Co3O4/Mn3O4 hybrid catalysts with heterointerfaces as bifunctional catalysts for Zn-air batteries, Journal of Energy Chemistry 68 (2022) 679–687. https://doi.org/10.1016/j.jechem.2021.12.032.
[93] M. Dong, X. Liu, L. Jiang, Z. Zhu, Y. Shu, S. Chen, Y. Dou, P. Liu, H. Yin, H. Zhao, Cobalt-doped Mn3O4 nanocrystals embedded in graphene nanosheets as a high-performance bifunctional oxygen electrocatalyst for rechargeable Zn–Air batteries, Green Energy & Environment 5 (2020) 499–505. https://doi.org/10.1016/j.gee.2020.06.022.
[94] Y. Wang, Y. Yang, S. Jia, X. Wang, K. Lyu, Y. Peng, H. Zheng, X. Wei, H. Ren, L. Xiao, J. Wang, D.A. Muller, H.D. Abruña, B.J. Hwang, J. Lu, L. Zhuang, Synergistic Mn-Co catalyst outperforms Pt on high-rate oxygen reduction for alkaline polymer electrolyte fuel cells, Nature Communications 10 (2019) 1506. https://doi.org/10.1038/s41467-019-09503-4.
[95] A.R. Mainar, L.C. Colmenares, O. Leonet, F. Alcaide, J.J. Iruin, S. Weinberger, V. Hacker, E. Iruin, I. Urdanpilleta, J.A. Blazquez, Manganese oxide catalysts for secondary zinc air batteries: from electrocatalytic activity to bifunctional air electrode performance, Electrochimica Acta 217 (2016) 80–91. https://doi.org/10.1016/j.electacta.2016.09.052.
[96] B. Chen, H. Miao, R. Hu, M. Yin, X. Wu, S. Sun, Q. Wang, S. Li, J. Yuan, Efficiently optimizing the oxygen catalytic properties of the birnessite type manganese dioxide for zinc-air batteries, Journal of Alloys and Compounds 852 (2021) 157012. https://doi.org/10.1016/j.jallcom.2020.157012.
[97] D. Ji, J. Sun, L. Tian, A. Chinnappan, T. Zhang, W.A.D.M. Jayathilaka, R. Gosh, C. Baskar, Q. Zhang, S. Ramakrishna, Engineering of the Heterointerface of Porous Carbon Nanofiber–Supported Nickel and Manganese Oxide Nanoparticle for Highly Efficient Bifunctional Oxygen Catalysis, Advanced Functional Materials 30 (2020) 1910568. https://doi.org/10.1002/adfm.201910568.
[98] A. Mathur, A. Halder, One-step synthesis of bifunctional iron-doped manganese oxide nanorods for rechargeable zinc–air batteries, Catalysis Science and Technology 9 (2019) 1245–1254. https://doi.org/10.1039/C8CY02498G.
[99] X.F. Lu, Y. Chen, S. Wang, S. Gao, X.W. (David) Lou, Interfacing Manganese Oxide and Cobalt in Porous Graphitic Carbon Polyhedrons Boosts Oxygen Electrocatalysis for Zn–Air Batteries, Advanced Materials 31 (2019) 1902339. https://doi.org/10.1002/adma.201902339.
[100] X. Liu, M. Park, M.G. Kim, S. Gupta, X. Wang, G. Wu, J. Cho, High-performance non-spinel cobalt–manganese mixed oxide-based bifunctional electrocatalysts for rechargeable zinc–air batteries, Nano Energy 20 (2016) 315–325. https://doi.org/10.1016/j.nanoen.2015.11.030.
[101] Y. Sugawara, H. Kobayashi, I. Honma, T. Yamaguchi, Effect of Metal Coordination Fashion on Oxygen Electrocatalysis of Cobalt–Manganese Oxides, ACS Omega 5 (2020) 29388–29397. https://doi.org/10.1021/acsomega.0c04254.
[102] Q. Jin, C. Wang, Y. Guo, Y. Xiao, X. Tan, J. Chen, W. He, Y. Li, H. Cui, C. Wang, Axial Oxygen Ligands Regulating Electronic and Geometric Structure of

Zn-N-C Sites to Boost Oxygen Reduction Reaction, Advanced Science 10 (2023) 2302152. https://doi.org/10.1002/advs.202302152.
[103] L. Ye, G. Chai, Z. Wen, Zn-MOF-74 Derived N-Doped Mesoporous Carbon as pH-Universal Electrocatalyst for Oxygen Reduction Reaction, Advanced Functional Materials 27 (2017) 1606190. https://doi.org/10.1002/adfm.201606190.
[104] Y. Pan, K. Sun, S. Liu, X. Cao, K. Wu, W.-C. Cheong, Z. Chen, Y. Wang, Y. Li, Y. Liu, D. Wang, Q. Peng, C. Chen, Y. Li, Core–Shell ZIF-8@ZIF-67-Derived CoP Nanoparticle-Embedded N-Doped Carbon Nanotube Hollow Polyhedron for Efficient Overall Water Splitting, Journal of American Chemical Society 140 (2018) 2610–2618. https://doi.org/10.1021/jacs.7b12420.
[105] J. Liu, J. Yu, X. Wang, M. Cheng, S. Sun, S. Hu, C. Li, Z. Wang, Core–Shell ZIF-8@ZIF-67-Derived Cobalt Nanoparticle-Embedded Nanocage Electrocatalyst with Excellent Oxygen Reduction Performance for Zn–Air Batteries, ACS Applied Materials & Interfaces 15 (2023) 59482–59493. https://doi.org/10.1021/acsami.3c14231.
[106] G. Yusibova, J.-M. Assafrei, K. Ping, J. Aruväli, P. Paiste, M. Käärik, J. Leis, H.-M. Piirsoo, A. Tamm, A. Kikas, V. Kisand, P. Starkov, N. Kongi, Bimetallic metal-organic-framework-derived porous cobalt manganese oxide bifunctional oxygen electrocatalyst, Journal of Electroanalytical Chemistry 930 (2023) 117161. https://doi.org/10.1016/j.jelechem.2023.117161.
[107] K. Ping, A. Braschinsky, M. Alam, R. Bhadoria, V. Mikli, A. Mere, J. Aruväli, P. Paiste, S. Vlassov, M. Kook, M. Rähn, V. Sammelselg, K. Tammeveski, N. Kongi, P. Starkov, Fused Hybrid Linkers for Metal–Organic Framework-Derived Bifunctional Oxygen Electrocatalysts, ACS Applied Energy Materials 3 (2020) 152–157. https://doi.org/10.1021/acsaem.9b02039.
[108] K. Ping, M. Alam, S. Ray Kahnert, R. Bhadoria, A. Mere, V. Mikli, M. Käärik, J. Aruväli, P. Paiste, A. Kikas, V. Kisand, I. Järving, J. Leis, N. Kongi, P. Starkov, Multi-purpose heterogeneous catalyst material from an amorphous cobalt metal–organic framework, Materials Advances 2 (2021) 4009–4015. https://doi.org/10.1039/D1MA00414J.
[109] G. Yusibova, K. Ping, M. Käärik, J. Leis, J. Aruväli, K. Šmits, T. Käämbre, V. Kisand, Y. Karpichev, K. Tammeveski, N. Kongi, Optimizing post-treatment strategies for enhanced oxygen reduction/evolution activity in Co–N–C electrocatalyst, International Journal of Hydrogen Energy 82 (2024) 398–406. https://doi.org/10.1016/j.ijhydene.2024.07.388.
[110] Y. Huang, Y. Chen, M. Xu, T. Asset, P. Tieu, A. Gili, D. Kulkarni, V. De Andrade, F. De Carlo, H.S. Barnard, A. Doran, D.Y. Parkinson, X. Pan, P. Atanassov, I.V. Zenyuk, Catalysts by pyrolysis: Direct observation of chemical and morphological transformations leading to transition metal-nitrogen-carbon materials, Materials Today 47 (2021) 53–68. https://doi.org/10.1016/j.mattod.2021.02.006.
[111] Y. Chen, Y. Huang, M. Xu, T. Asset, X. Yan, K. Artyushkova, M. Kodali, E. Murphy, A. Ly, X. Pan, I.V. Zenyuk, P. Atanassov, Catalysts by pyrolysis: Direct observation of transformations during re-pyrolysis of transition metal-nitrogen-carbon materials leading to state-of-the-art platinum group metal-free electrocatalyst, Materials Today 53 (2022) 58–70. https://doi.org/10.1016/j.mattod.2022.01.016.
[112] A.J. Bard, L.R. Faulkner, Electrochemical Methods: Fundamentals and Applications, New York: Wiley, 2nd ed., 2001.

[113] E.R. Cohen, B.N. Taylor, The 1986 adjustment of the fundamental physical constants, Reviews of Modern Physics 59 (1987) 1121–1148. https://doi.org/10.1103/RevModPhys.59.1121.
[114] J. Wu, Z. Meng, R. Zhang, T. Tian, R. Wang, H. Tang, Boosting Oxygen Reduction Catalysis with Hierarchically Porous Fe-Doped Carbon by Chemical Vapor Deposition in Zn–Air Batteries, Energy & Fuels 36 (2022) 4006–4014. https://doi.org/10.1021/acs.energyfuels.2c00099.
[115] W. Zhu, Y. Pei, J.C. Douglin, J. Zhang, H. Zhao, J. Xue, Q. Wang, R. Li, Y. Qin, Y. Yin, D.R. Dekel, M.D. Guiver, Multi-scale study on bifunctional Co/Fe–N–C cathode catalyst layers with high active site density for the oxygen reduction reaction, Applied Catalysis B: Environmental 299 (2021) 120656. https://doi.org/10.1016/j.apcatb.2021.120656.
[116] Y. Kumar, E. Kibena-Põldsepp, J. Kozlova, M. Rähn, A. Treshchalov, A. Kikas, V. Kisand, J. Aruväli, A. Tamm, J.C. Douglin, S.J. Folkman, I. Gelmetti, F.A. Garcés-Pineda, J.R. Galán-Mascarós, D.R. Dekel, K. Tammeveski, Bifunctional Oxygen Electrocatalysis on Mixed Metal Phthalocyanine-Modified Carbon Nanotubes Prepared via Pyrolysis, ACS Applied Materials & Interfaces 13 (2021) 41507–41516. https://doi.org/10.1021/acsami.1c06737.
[117] D. Zhang, P. Sun, Q. Zhou, B. Li, Y. Wei, T. Gong, N. Huang, X. Lv, L. Fang, X. Sun, Enhanced oxygen reduction and evolution in N-doped carbon anchored with Co nanoparticles for rechargeable Zn-air batteries, Applied Surface Science 542 (2021) 148700. https://doi.org/10.1016/j.apsusc.2020.148700.
[118] B.J. Ferraz, J. Kong, B. Li, N. Neng Tham, C. Blackman, Z. Liu, Co/N nanoparticles supported on a C3N4/polydopamine framework as a bifunctional electrocatalyst for rechargeable zinc-air batteries, Journal of Electroanalytical Chemistry 921 (2022) 116702. https://doi.org/10.1016/j.jelechem.2022.116702.
[119] O.Y. Bisen, R. Nandan, G. Raj, A.K. Yadav, K.K. Nanda, Rational Designing of Co–N–C Electrocatalysts for Comprehensive Elucidation of Intrinsic and Extrinsic Activities in the Oxygen Reduction Reaction, ACS Applied Energy Materials 5 (2022) 14019–14034. https://doi.org/10.1021/acsaem.2c02606.
[120] J. Zhu, T. Qu, F. Su, Y. Wu, Y. Kang, K. Chen, Y. Yao, W. Ma, B. Yang, Y. Dai, F. Liang, D. Xue, Highly dispersed Co nanoparticles decorated on a N-doped defective carbon nano-framework for a hybrid Na–air battery, Dalton Transactions 49 (2020) 1811–1821. https://doi.org/10.1039/C9DT04073K.
[121] D. Yan, Y. Li, J. Huo, R. Chen, L. Dai, S. Wang, Defect Chemistry of Nonprecious-Metal Electrocatalysts for Oxygen Reactions, Advanced Materials 29 (2017) 1606459. https://doi.org/10.1002/adma.201606459.
[122] Q. Xu, X. Peng, Z. Zhu, K. Luo, Y. Liu, D. Yuan, Co2P nanoparticles supported on cobalt-embedded N-doped carbon materials as a bifunctional electrocatalyst for rechargeable Zn-air batteries, International Journal of Hydrogen Energy 47 (2022) 16518–16527. https://doi.org/10.1016/j.ijhydene.2022.03.142.
[123] H. Zhong, Y. Luo, S. He, P. Tang, D. Li, N. Alonso-Vante, Y. Feng, Electrocatalytic Cobalt Nanoparticles Interacting with Nitrogen-Doped Carbon Nanotube in Situ Generated from a Metal–Organic Framework for the Oxygen Reduction Reaction, ACS Applied Materials & Interfaces 9 (2017) 2541–2549. https://doi.org/10.1021/acsami.6b14942.

[124] J. Qin, Z. Liu, D. Wu, J. Yang, Optimizing the electronic structure of cobalt via synergized oxygen vacancy and Co-N-C to boost reversible oxygen electrocatalysis for rechargeable Zn-air batteries, Applied Catalysis B: Environmental 278 (2020) 119300. https://doi.org/10.1016/j.apcatb.2020.119300.
[125] X. Peng, L. Wei, Y. Liu, T. Cen, Z. Ye, Z. Zhu, Z. Ni, D. Yuan, Cobalt Nanoparticles Embedded in N-Doped Carbon Nanotubes on Reduced Graphene Oxide as Efficient Oxygen Catalysts for Zn-Air Batteries, Energy & Fuels 34 (2020) 8931–8938. https://doi.org/10.1021/acs.energyfuels.0c01167.
[126] R. Wang, J. Cao, S. Cai, X. Yan, J. Li, W.M. Yourey, W. Tong, H. Tang, MOF@Cellulose Derived Co–N–C Nanowire Network as an Advanced Reversible Oxygen Electrocatalyst for Rechargeable Zinc–Air Batteries, ACS Applied Energy Materials 1 (2018) 1060–1068. https://doi.org/10.1021/acsaem.7b00204.
[127] D. Ding, K. Shen, X. Chen, H. Chen, J. Chen, T. Fan, R. Wu, Y. Li, Multi-Level Architecture Optimization of MOF-Templated Co-Based Nanoparticles Embedded in Hollow N-Doped Carbon Polyhedra for Efficient OER and ORR, ACS Catalysis 8 (2018) 7879–7888. https://doi.org/10.1021/acscatal.8b02504.
[128] H. Jin, J. Wang, D. Su, Z. Wei, Z. Pang, Y. Wang, In situ Cobalt–Cobalt Oxide/N-Doped Carbon Hybrids As Superior Bifunctional Electrocatalysts for Hydrogen and Oxygen Evolution, Journal of American Chemical Society 137 (2015) 2688–2694. https://doi.org/10.1021/ja5127165.
[129] H.B. Yang, J. Miao, S.-F. Hung, J. Chen, H.B. Tao, X. Wang, L. Zhang, R. Chen, J. Gao, H.M. Chen, L. Dai, B. Liu, Identification of catalytic sites for oxygen reduction and oxygen evolution in N-doped graphene materials: Development of highly efficient metal-free bifunctional electrocatalyst, Science Advances 2 (2016) e1501122. https://doi.org/10.1126/sciadv.1501122.
[130] S. Mao, Z. Wen, T. Huang, Y. Hou, J. Chen, High-performance bi-functional electrocatalysts of 3D crumpled graphene–cobalt oxide nanohybrids for oxygen reduction and evolution reactions, Energy & Environmental Science 7 (2014) 609–616. https://doi.org/10.1039/C3EE42696C.
[131] J. Li, Z. Zhou, K. Liu, F. Li, Z. Peng, Y. Tang, H. Wang, Co3O4/Co-N-C modified ketjenblack carbon as an advanced electrocatalyst for Al-air batteries, Journal of Power Sources 343 (2017) 30–38. https://doi.org/10.1016/j.jpowsour.2017.01.018.
[132] Y. Wang, J. Fu, Y. Zhang, M. Li, F.M. Hassan, G. Li, Z. Chen, Continuous fabrication of a MnS/Co nanofibrous air electrode for wide integration of rechargeable zinc–air batteries, Nanoscale 9 (2017) 15865–15872. https://doi.org/ 10.1039/C7NR05728H.
[133] J. Lilloja, E. Kibena-Põldsepp, A. Sarapuu, M. Käärik, J. Kozlova, P. Paiste, A. Kikas, A. Treshchalov, J. Leis, A. Tamm, V. Kisand, S. Holdcroft, K. Tammeveski, Transition metal and nitrogen-doped mesoporous carbons as cathode catalysts for anion-exchange membrane fuel cells, Applied Catalysis B: Environmental 306 (2022) 121113. https://doi.org/10.1016/j.apcatb.2022.121113.
[134] S. Kabir, K. Artyushkova, A. Serov, P. Atanassov, Role of Nitrogen Moieties in N-Doped 3D-Graphene Nanosheets for Oxygen Electroreduction in Acidic and Alkaline Media, ACS Applied Materials and Interfaces 10 (2018) 11623–11632. https://doi.org/10.1021/acsami.7b18651.
[135] Y. Kumar, E. Kibena-Põldsepp, J. Kozlova, A. Kikas, M. Käärik, J. Aruväli, V. Kisand, J. Leis, A. Tamm, K. Tammeveski, Bimetal Phthalocyanine-Modified Carbon Nanotube-Based Bifunctional Catalysts for Zinc-Air Batteries, Chem ElectroChem 8 (2021) 2662–2670. https://doi.org/10.1002/celc.202100498.

[136] Y.P. Zhu, T.Y. Ma, M. Jaroniec, S.Z. Qiao, Self-Templating Synthesis of Hollow Co_3O_4 Microtube Arrays for Highly Efficient Water Electrolysis, Angewandte Chemie International Edition 56 (2017) 1324–1328. https://doi.org/10.1002/anie.201610413.

[137] T. Meng, B. Mao, M. Cao, *In Situ* Coupling of MnO and Co@N-Doped Graphite Carbon Derived from Prussian Blue Analogous Achieves High-Performance Reversible Oxygen Electrocatalysis for Zn–Air Batteries, Inorganic Chemistry 60 (2021) 10340–10349. https://doi.org/10.1021/acs.inorgchem.1c00807.

[138] D. Wang, X. Pan, P. Yang, R. Li, H. Xu, Y. Li, F. Meng, J. Zhang, M. An, Transition Metal and Nitrogen Co-Doped Carbon-based Electrocatalysts for the Oxygen Reduction Reaction: From Active Site Insights to the Rational Design of Precursors and Structures, ChemSusChem 14 (2021) 33–55. https://doi.org/10.1002/cssc.202002137.

[139] A. Qaseem, F. Chen, C. Qiu, A. Mahmoudi, X. Wu, X. Wang, R.L. Johnston, Reduced Graphene Oxide decorated with Manganese Cobalt Oxide as Multifunctional Material for Mechanically Rechargeable and Hybrid Zinc–Air Batteries, Particle & Particle Systems Characterization 34 (2017) 1700097. https://doi.org/10.1002/ppsc.201700097.

[140] C. Zhang, F. Kong, Y. Qiao, Q. Zhao, A. Kong, Y. Shan, 3D Graphene-Carbon Nanotube Hybrid Supported Coupled Co-MnO Nanoparticles as Highly Efficient Bifunctional Electrocatalyst for Rechargeable Zn-Air Batteries, Chemistry – An Asian Journal 15 (2020) 3535–3541. https://doi.org/10.1002/asia.202000913.

[141] H. Shang, W. Sun, R. Sui, J. Pei, L. Zheng, J. Dong, Z. Jiang, D. Zhou, Z. Zhuang, W. Chen, J. Zhang, D. Wang, Y. Li, Engineering Isolated Mn–N2C2 Atomic Interface Sites for Efficient Bifunctional Oxygen Reduction and Evolution Reaction, Nano Letters 20 (2020) 5443–5450. https://doi.org/10.1021/acs.nanolett.0c01925.

[142] Y. Yang, H. Fei, G. Ruan, J.M. Tour, Porous Cobalt-Based Thin Film as a Bifunctional Catalyst for Hydrogen Generation and Oxygen Generation, Advanced Materials 27 (2015) 3175–3180. https://doi.org/10.1002/adma.201500894.

[143] Z. Zhang, H. Sun, J. Li, Z. Shi, M. Fan, H. Bian, T. Wang, D. Gao, S-doped CoMn2O4 with more high valence metallic cations and oxygen defects for zinc-air batteries, Journal of Power Sources 491 (2021) 229584. https://doi.org/10.1016/j.jpowsour.2021.229584.

[144] J. Bian, Z. Li, N. Li, C. Sun, Oxygen Deficient LaMn0.75Co0.25O3−δ Nanofibers as an Efficient Electrocatalyst for Oxygen Evolution Reaction and Zinc–Air Batteries, Inorganic Chemistry 58 (2019) 8208–8214. https://doi.org/10.1021/acs.inorgchem.9b01034.

[145] Y. Wang, T. Hu, Y. Chen, H. Yuan, Y. Qiao, Crystal facet-dependent activity of α-Mn2O3 for oxygen reduction and oxygen evolution reactions, International Journal of Hydrogen Energy 45 (2020) 22744–22751. https://doi.org/10.1016/j.ijhydene.2020.06.085.

[146] P. Moni, M. Mooste, K. Tammeveski, K. Rezwan, M. Wilhelm, One-dimensional polymer-derived ceramic nanowires with electrocatalytically active metallic silicide tips as cathode catalysts for Zn–air batteries, RSC Advances 11 (2021) 39707–39717. https://doi.org/10.1039/D1RA05688C.

[147] Y. Zhong, J. Dai, X. Xu, C. Su, Z. Shao, Facilitating Oxygen Redox on Manganese Oxide Nanosheets by Tuning Active Species and Oxygen Defects for Zinc-Air Batteries, ChemElectroChem 7 (2020) 4949–4955. https://doi.org/10.1002/celc.202001419.

[148] A. Heuer-Jungemann, N. Feliu, I. Bakaimi, M. Hamaly, A. Alkilany, I. Chakraborty, A. Masood, M.F. Casula, A. Kostopoulou, E. Oh, K. Susumu, M.H. Stewart, I.L. Medintz, E. Stratakis, W.J. Parak, A.G. Kanaras, The Role of Ligands in the Chemical Synthesis and Applications of Inorganic Nanoparticles, Chemical Reviews 119 (2019) 4819–4880. https://doi.org/10.1021/acs.chemrev. 8b00733.

[149] G. Yusibova, J.C. Douglin, I. Vetik, J. Pozdnjakova, K. Ping, J. Aruväli, A. Kikas, V. Kisand, M. Käärik, J. Leis, T. Kaljuvee, P. Paaver, S. Oras, Ł. Ciupiński, T. Plocinski, M. Konuhova, A.I. Popov, D.R. Dekel, V. Ivaništšev, N. Kongi, Pyrolytic Transformation of Zn-TAL Metal–Organic Framework into Hollow Zn–N–C Spheres for Improved Oxygen Reduction Reaction Catalysis, ACS Omega 10 (2025) 15280–15291. https://doi.org/10.1021/acsomega.4c11318.

[150] F. Ma, X. Liu, X. Wang, J. Liang, J. Huang, C. Priest, J. Liu, S. Jiao, T. Wang, G. Wu, Y. Huang, Q. Li, Atomically dispersed Zn-Co-N-C catalyst boosting efficient and robust oxygen reduction catalysis in acid via stabilizing Co-N bonds, Fundamental Research 3 (2023) 909–917. https://doi.org/10.1016/j.fmre.2022.03.008.

[151] W. Li, C. Min, F. Tan, Z. Li, B. Zhang, R. Si, M. Xu, W. Liu, L. Zhou, Q. Wei, Y. Zhang, X. Yang, Bottom-Up Construction of Active Sites in a Cu–N4–C Catalyst for Highly Efficient Oxygen Reduction Reaction, ACS Nano 13 (2019) 3177–3187. https://doi.org/10.1021/acsnano.8b08692.

[152] J. Ding, H.-F. Wang, X. Yang, W. Ju, K. Shen, L. Chen, Y. Li, A Janus heteroatom-doped carbon electrocatalyst for hydrazine oxidation, National Science Review 10 (2023) nwac231. https://doi.org/10.1093/nsr/nwac231.

[153] J. Hou, C. Cao, F. Idrees, X. Ma, Hierarchical Porous Nitrogen-Doped Carbon Nanosheets Derived from Silk for Ultrahigh-Capacity Battery Anodes and Supercapacitors, ACS Nano 9 (2015) 2556–2564. https://doi.org/10.1021/nn506394r.

[154] Y. Zhang, Y. Jia, M. Li, L. Hou, Influence of the 2-methylimidazole/zinc nitrate hexahydrate molar ratio on the synthesis of zeolitic imidazolate framework-8 crystals at room temperature, Scientific Reports 8 (2018) 9597. https://doi.org/10.1038/s41598-018-28015-7.

[155] D. Wei, L. Chen, L. Tian, S. Ramakrishna, D. Ji, Zn Single Atoms/Clusters/Nanoparticles Embedded in the Hybrid Carbon Aerogels for High-Performance ORR Electrocatalysis, Inorganic Chemistry 62 (2023) 16547–16553. https://doi.org/10.1021/acs.inorgchem.3c02417.

[156] R.K. Singh, J.C. Douglin, V. Kumar, P. Tereshchuk, P.G. Santori, E.B. Ferreira, G. Jerkiewicz, P.J. Ferreira, A. Natan, F. Jaouen, D.R. Dekel, Metal-free advanced energy materials for the oxygen reduction reaction in anion-exchange membrane fuel cells, Applied Catalysis B: Environment and Energy 357 (2024) 124319. https://doi.org/10.1016/j.apcatb.2024.124319.

[157] A.B. Jorge, R. Jervis, A.P. Periasamy, M. Qiao, J. Feng, L.N. Tran, M.-M. Titirici, 3D Carbon Materials for Efficient Oxygen and Hydrogen Electrocatalysis, Advanced Energy Materials 10 (2020) 1902494. https://doi.org/10.1002/aenm.201902494.

[158] Z. Huang, Z. Liao, W. Yang, H. Zhou, C. Fu, Y. Gong, L. Chen, Y. Kuang, Different types of nitrogen species in nitrogen-doped carbon material: The formation mechanism and catalytic role on oxygen reduction reaction, Electrochimica Acta 245 (2017) 957–966. https://doi.org/10.1016/j.electacta.2017.06.026.

[159] U. Tylus, Q. Jia, K. Strickland, N. Ramaswamy, A. Serov, P. Atanassov, S. Mukerjee, Elucidating Oxygen Reduction Active Sites in Pyrolyzed Metal–Nitrogen

Coordinated Non-Precious-Metal Electrocatalyst Systems, Journal of Physical Chemistry C 118 (2014) 8999–9008. https://doi.org/10.1021/jp500781v.
[160] J. Li, S. Chen, N. Yang, M. Deng, S. Ibraheem, J. Deng, J. Li, L. Li, Z. Wei, Ultrahigh-Loading Zinc Single-Atom Catalyst for Highly Efficient Oxygen Reduction in Both Acidic and Alkaline Media, Angewandte Chemie International Edition 58 (2019) 7035–7039. https://doi.org/10.1002/anie.201902109.
[161] L. Hu, F. Yu, F. Wang, S. Yang, B. Peng, L. Chen, G. Wang, J. Hou, B. Dai, Z.-Q. Tian, Overwhelming electrochemical oxygen reduction reaction of zinc-nitrogen-carbon from biomass resource chitosan *via* a facile carbon bath method, Chinese Chemical Letters 31 (2020) 1207–1212. https://doi.org/10.1016/j.cclet.2019.06.041.
[162] L. Jin, K. Wu, M. Liao, D. Wang, B. Jayaraman, S.G. Peera, C. Liu, Theoretical analysis of single Zn atoms with N/C on graphene promoting oxygen redox in alkaline medium, Molecular Catalysis 553 (2024) 113799. https://doi.org/10.1016/j.mcat.2023.113799.

10. SUMMARY IN ESTONIAN

TAL MOF-põhised M-N-C elektrokatalüsaatorid hapniku redutseerumis- ja eraldumisreaktsioonideks

Kuna vajadus jätkusuutlike energiasalvestus- ja muundamistehnoloogiate järele järjest kasvab, keskendub käesolev doktoritöö tõhusate, kuluefektiivsete ja skaleeritavate elektrokatalüsaatorite arendamisele, mis on saadud metall-orgaaniliste raamistike (MOF) põhjal ja mõeldud uue põlvkonna kütuseelementide (FC) ning metall-õhk akude (MAB) jaoks. Need tehnoloogiad sõltuvad suuresti hapniku redutseerumis- (ORR) ja eraldumisreaktsioonidest (OER), mille peamine piirav tegur on aeglane kineetika. Selle probleemi ületamiseks keskenduti väärismetallivabade elektrokatalüsaatorite väljatöötamisele, mis põhinevad siirdemetall–lämmastik–süsinik (M–N–C) materjalidel. Töö keskmes on uudne MOF-perekond nimega TAL (*TalTech–UniTartu Alliance Laboratory*), mis töötati välja meie uurimisrühmas spetsiaalselt disainitud ja multifunktsionaalsete M–N–C katalüsaatori lähteainete loomiseks. Siirdemetallide (Co, Mn, Zn) ja sünteetiliste meetodite varieerimine võimaldas TAL-seeria materjalide süsteemset kontrolli poorse struktuuri, elektrooniliste omaduste ja lämmastikusideme konfiguratsiooni üle ning katalüsaatorite omaduste täppishäälestust molekulaarsel tasemel. Strateegilise sünteesi, pürolüüsi optimeerimise ja järeltöötluse kombineerimisel õnnestus välja töötada kõrge ORR-i ja OER-i aktiivsusega Co–N–C, MnCo–N–C ja Zn–N–C katalüsaatorid aluselise keskkonna jaoks. TAL-2-st saadud Co–N–C materjalid näitasid kõrget bifunktsionaalset elektrokatalüütilist aktiivsust, mida mõjutas tugevalt pürolüüsitemperatuur ja happetöötlemine; parimateks osutusid Co-700L5 ja Co-900L5 materjalid, millel olid madal ΔE väärtus ja optimeeritud struktuursed omadused. Mn/Co bimetalse materjali (TAL-42-900) suurepäraseid omadusi põhjustasid metallide sünergiline toime, kõrge mesopoorsus ja dispergeeritud M–N_x aktiivsed tsentrid, saavutades silmapaistvaid tulemusi nii poolrakus kui ka tsink–õhk akus. Zn-N-C katalüsaator säilitas pärast pürolüüsi oma õõnsa, poorse morfoloogia ja näitas ORR-i puhul poollainepotentsiaali ($E_{1/2}$) 0,84 V, mis on võrreldav kommertsiaalse Pt/C-ga. Lisaks ilmnes selle katalüsaatori puhul suurepärane vastupidavus ja jõudlus anioonivahetusmembraaniga kütuseelemendis (AEMFC), saavutades suure võimsustiheduse (550 mW cm^{-2}). Kokkuvõttes kinnitab doktoritöö TAL-MOF-seeria sobivust kui paindlikku platvormi kõrge jõudlusega M-N-C katalüsaatorite ratsionaalseks disainiks. Saadud teadmised struktuuri ja aktiivsuse seoste, aktiivsete tsentrite moodustumise ja elektrokatalüütiliste mehhanismide kohta loovad tugeva aluse väärismetallivabade katalüsaatormaterjalide edasiseks arendamiseks. Doktoritöö tulemused toetavad üleminekut puhastele ja tõhusatele elektrokeemilistele energiasüsteemidele, edendades MOF-põhiste elektrokatalüsaatorite praktilist kasutuselevõttu taastuvenergia salvestamise ja muundamise seadmetes.

11. ACKNOWLEDGEMENTS

First and foremost, I would like to express my deepest gratitude to my supervisor, Assoc. Prof. Nadežda Kongi, for her support, guidance, and encouragement throughout this journey. Your expertise and insights have been invaluable to the development of this thesis. I am also profoundly grateful to Prof. Kaido Tammeveski for his constant support and constructive feedback. I am thankful to my colleagues and friends at the University of Tartu, who have provided a stimulating and enjoyable environment.

Furthermore, I would like to express my sincere gratitude to my colleagues and collaborators for contributing to the development of the TAL MOF catalysts. More specifically, I am grateful to the University of Tartu collaborators for conducting PXRD (Dr. Jaan Aruväli), MP-AES (Dr. Päärn Paiste, Dr. Peeter Paaver), electron microscopy (Dr. Sergei Vlassov), N_2 physisorption (Dr. Maike Käärik, Dr. Jaan Leis) and XPS (Dr. Arvo Kikas, Dr. Vambola Kisand) measurements. Moreover, I would like to thank external collaborators for performing electron microscopy (Dr. Krišjānis Šmits – University of Latvia), and TGA measurements (Dr. Tiit Kaljuvee – Tallinn Technical University). Additionally, I am grateful to my colleagues and students at KongiLab for their support, and deeply thankful to my friend and partner for their emotional encouragement.

PUBLICATIONS

CURRICULUM VITAE

Name: Gulnara Yusibova
Date of birth: May 27, 1996
Citizenship: Azerbaijani
Address: Ravila 14a, 50411 Tartu, Estonia
E-mail: gulnara.yusibova@ut.ee

Education:

2021–…	University of Tartu, Faculty of Science and Technology, PhD studies, Chemistry
2021–2023	EIT Manufacturing Doctoral School
2019–2021	University of Tartu, Faculty of Science and Technology, MSc studies, Materials Science and Technology
2013–2018	Baku Engineering University, Baku, Azerbaijan, BSc studies, Chemistry Education

Professional experience:

2021–…	University of Tartu, Institute of Chemistry, Junior Research Fellow

Major scientific publications:

1. **G. Yusibova**, K. Ping, M. Käärik, J. Leis, J. Aruväli, K. Šmits, T. Käämbre, V. Kisand, Y. Karpichev, K. Tammeveski, N. Kongi, Optimizing post-treatment strategies for enhanced oxygen reduction/evolution activity in Co–N–C electrocatalyst, International Journal of Hydrogen Energy 82 (2024) 398–406. https://doi.org/10.1016/j.ijhydene.2024.07.388.
2. **G. Yusibova**, J.-M. Assafrei, K. Ping, J. Aruväli, P. Paiste, M. Käärik, J. Leis, H.-M. Piirsoo, A. Tamm, A. Kikas, V. Kisand, P. Starkov, N. Kongi, Bimetallic metal-organic-framework-derived porous cobalt manganese oxide bifunctional oxygen electrocatalyst, Journal of Electroanalytical Chemistry 930 (2023) 117161. https://doi.org/10.1016/j.jelechem.2023.117161.
3. **G. Yusibova**, J.C. Douglin, I. Vetik, J. Pozdnjakova, K. Ping, J. Aruväli, A. Kikas, V. Kisand, M. Käärik, J. Leis, T. Kaljuvee, P. Paaver, S. Oras, Ł. Ciupiński, T. Plocinski, M. Konuhova, A.I. Popov, D.R. Dekel, V. Ivaništšev, N. Kongi, Pyrolytic Transformation of Zn-TAL Metal–Organic Framework into Hollow Zn–N–C Spheres for Improved Oxygen Reduction Reaction Catalysis, ACS Omega 10 (2025) 15280–15291. https://doi.org/10.1021/acsomega. 4c11318.
4. Kosimov, A.; **Yusibova, G.**; Aruväli, J.; Paiste, P.; Käärik, M.; Leis, J.; Kikas, A.; Kisand, V.; Šmits, K.; Kongi, N. Liquid-Assisted Grinding/ Compression: A Facile Mechanosynthetic Route for the Production of High-Performing Co–

N–C Electrocatalyst Materials. Green Chem. 2022, 24 (1), 305–314. https://doi.org/10.1039/D1GC03433B.

5. Kosimov, A.; Alimbekova, A.; Assafrei, J.-M.; **Yusibova, G.**; Aruväli, J.; Käärik, M.; Leis, J.; Paiste, P.; Ahmadi, M.; Roohi, K.; Taheri, P.; Pinto, S. M.; Cepitis, R.; Baptista, A. J.; Teppor, P.; Lust, E.; Kongi, N. Template-Assisted Mechanosynthesis Leading to Benchmark Energy Efficiency and Sustainability in the Production of Bifunctional Fe–N–C Electrocatalysts. ACS Sustainable Chem. Eng. 2023, 11 (29), 10825–10834. https://doi.org/10.1021/acssuschemeng.3c02077.
6. Kosimov, A.; **Yusibova, G.**; Wojsiat, I. T.; Aruväli, J.; Käärik, M.; Leis, J.; Paaver, P.; Vlassov, S.; Kikas, A.; Kisand, V.; Piirsoo, H.-M.; Kukli, K.; Heinmaa, I.; Kaljuvee, T.; Kongi, N. Mechanosynthesis of a Bifunctional FeNi–N–C Oxygen Electrocatalyst via Facile Mixed-Phase Templating and Pre-heating-Pyrolysis. J. Mater. Chem. A 2023, 12 (1), 335–342. https://doi.org/10.1039/D3TA04580C.

ELULOOKIRJELDUS

Nimi: Gulnara Yusibova
Sünniaeg: 27. mai 1996
Kodakondsus: Aserbaidžaani
Aadress: Ravila 14a, 50411 Tartu, Eesti
E-post: gulnara.yusibova@ut.ee

Hariduskäik:

2021–…	Tartu Ülikool, Loodus- ja täppisteaduste valdkond, doktoriõpe, keemia
2021–2023	EIT Manufacturing doktorikool
2019–2021	Tartu Ülikool, Loodus- ja täppisteaduste valdkond, magistriõpe, keemia eriala, Materjaliteaduse ja tehnoloogia programm
2013–2018	Bakuu Tehnikaülikool, Bakuu, Aserbaidžaan, BSc keemiahariduse eriala

Töökogemus:

2021–…	Tartu Ülikool, Keemia instituut, nooremteadur

Publikatsioonide loetelu:

1. **G. Yusibova**, K. Ping, M. Käärik, J. Leis, J. Aruväli, K. Šmits, T. Käämbre, V. Kisand, Y. Karpichev, K. Tammeveski, N. Kongi, Optimizing post-treatment strategies for enhanced oxygen reduction/evolution activity in Co–N–C electrocatalyst, International Journal of Hydrogen Energy 82 (2024) 398–406. https://doi.org/10.1016/j.ijhydene.2024.07.388.
2. **G. Yusibova**, J.-M. Assafrei, K. Ping, J. Aruväli, P. Paiste, M. Käärik, J. Leis, H.-M. Piirsoo, A. Tamm, A. Kikas, V. Kisand, P. Starkov, N. Kongi, Bimetallic metal-organic-framework-derived porous cobalt manganese oxide bifunctional oxygen electrocatalyst, Journal of Electroanalytical Chemistry 930 (2023) 117161. https://doi.org/10.1016/j.jelechem.2023.117161.
3. **G. Yusibova**, J.C. Douglin, I. Vetik, J. Pozdnjakova, K. Ping, J. Aruväli, A. Kikas, V. Kisand, M. Käärik, J. Leis, T. Kaljuvee, P. Paaver, S. Oras, Ł. Ciupiński, T. Plocinski, M. Konuhova, A.I. Popov, D.R. Dekel, V. Ivaništšev, N. Kongi, Pyrolytic Transformation of Zn-TAL Metal–Organic Framework into Hollow Zn–N–C Spheres for Improved Oxygen Reduction Reaction Catalysis, ACS Omega 10 (2025) 15280–15291. https://doi.org/10.1021/acsomega.4c11318.
4. Kosimov, A.; **Yusibova, G.**; Aruväli, J.; Paiste, P.; Käärik, M.; Leis, J.; Kikas, A.; Kisand, V.; Šmits, K.; Kongi, N. Liquid-Assisted Grinding/ Compression: A Facile Mechanosynthetic Route for the Production of High-Performing Co–

N–C Electrocatalyst Materials. Green Chem. 2022, 24 (1), 305–314. https://doi.org/10.1039/D1GC03433B.

5. Kosimov, A.; Alimbekova, A.; Assafrei, J.-M.; **Yusibova, G.**; Aruväli, J.; Käärik, M.; Leis, J.; Paiste, P.; Ahmadi, M.; Roohi, K.; Taheri, P.; Pinto, S. M.; Cepitis, R.; Baptista, A. J.; Teppor, P.; Lust, E.; Kongi, N. Template-Assisted Mechanosynthesis Leading to Benchmark Energy Efficiency and Sustainability in the Production of Bifunctional Fe–N–C Electrocatalysts. ACS Sustainable Chem. Eng. 2023, 11 (29), 10825–10834. https://doi.org/10.1021/acssuschemeng.3c02077.
6. Kosimov, A.; **Yusibova, G.**; Wojsiat, I. T.; Aruväli, J.; Käärik, M.; Leis, J.; Paaver, P.; Vlassov, S.; Kikas, A.; Kisand, V.; Piirsoo, H.-M.; Kukli, K.; Heinmaa, I.; Kaljuvee, T.; Kongi, N. Mechanosynthesis of a Bifunctional FeNi–N–C Oxygen Electrocatalyst via Facile Mixed-Phase Templating and Preheating-Pyrolysis. J. Mater. Chem. A 2023, 12 (1), 335–342. https://doi.org/10.1039/D3TA04580C.

DISSERTATIONES CHIMICAE UNIVERSITATIS TARTUENSIS

1. **Toomas Tamm.** Quantum-chemical simulation of solvent effects. Tartu, 1993, 110 p.
2. **Peeter Burk.** Theoretical study of gas-phase acid-base equilibria. Tartu, 1994, 96 p.
3. **Victor Lobanov.** Quantitative structure-property relationships in large descriptor spaces. Tartu, 1995, 135 p.
4. **Vahur Mäemets.** The ^{17}O and ^{1}H nuclear magnetic resonance study of H_2O in individual solvents and its charged clusters in aqueous solutions of electrolytes. Tartu, 1997, 140 p.
5. **Andrus Metsala.** Microcanonical rate constant in nonequilibrium distribution of vibrational energy and in restricted intramolecular vibrational energy redistribution on the basis of slater's theory of unimolecular reactions. Tartu, 1997, 150 p.
6. **Uko Maran.** Quantum-mechanical study of potential energy surfaces in different environments. Tartu, 1997, 137 p.
7. **Alar Jänes.** Adsorption of organic compounds on antimony, bismuth and cadmium electrodes. Tartu, 1998, 219 p.
8. **Kaido Tammeveski.** Oxygen electroreduction on thin platinum films and the electrochemical detection of superoxide anion. Tartu, 1998, 139 p.
9. **Ivo Leito.** Studies of Brønsted acid-base equilibria in water and non-aqueous media. Tartu, 1998, 101 p.
10. **Jaan Leis.** Conformational dynamics and equilibria in amides. Tartu, 1998, 131 p.
11. **Toonika Rinken.** The modelling of amperometric biosensors based on oxidoreductases. Tartu, 2000, 108 p.
12. **Dmitri Panov.** Partially solvated Grignard reagents. Tartu, 2000, 64 p.
13. **Kaja Orupõld.** Treatment and analysis of phenolic wastewater with microorganisms. Tartu, 2000, 123 p.
14. **Jüri Ivask.** Ion Chromatographic determination of major anions and cations in polar ice core. Tartu, 2000, 85 p.
15. **Lauri Vares.** Stereoselective Synthesis of Tetrahydrofuran and Tetrahydropyran Derivatives by Use of Asymmetric Horner-Wadsworth-Emmons and Ring Closure Reactions. Tartu, 2000, 184 p.
16. **Martin Lepiku.** Kinetic aspects of dopamine D_2 receptor interactions with specific ligands. Tartu, 2000, 81 p.
17. **Katrin Sak.** Some aspects of ligand specificity of P2Y receptors. Tartu, 2000, 106 p.
18. **Vello Pällin.** The role of solvation in the formation of iotsitch complexes. Tartu, 2001, 95 p.
19. **Katrin Kollist.** Interactions between polycyclic aromatic compounds and humic substances. Tartu, 2001, 93 p.

20. **Ivar Koppel.** Quantum chemical study of acidity of strong and superstrong Brønsted acids. Tartu, 2001, 104 p.
21. **Viljar Pihl.** The study of the substituent and solvent effects on the acidity of OH and CH acids. Tartu, 2001, 132 p.
22. **Natalia Palm.** Specification of the minimum, sufficient and significant set of descriptors for general description of solvent effects. Tartu, 2001, 134 p.
23. **Sulev Sild.** QSPR/QSAR approaches for complex molecular systems. Tartu, 2001, 134 p.
24. **Ruslan Petrukhin.** Industrial applications of the quantitative structure-property relationships. Tartu, 2001, 162 p.
25. **Boris V. Rogovoy.** Synthesis of (benzotriazolyl)carboximidamides and their application in relations with *N*- and *S*-nucleophyles. Tartu, 2002, 84 p.
26. **Koit Herodes.** Solvent effects on UV-vis absorption spectra of some solvatochromic substances in binary solvent mixtures: the preferential solvation model. Tartu, 2002, 102 p.
27. **Anti Perkson.** Synthesis and characterisation of nanostructured carbon. Tartu, 2002, 152 p.
28. **Ivari Kaljurand.** Self-consistent acidity scales of neutral and cationic Brønsted acids in acetonitrile and tetrahydrofuran. Tartu, 2003, 108 p.
29. **Karmen Lust.** Adsorption of anions on bismuth single crystal electrodes. Tartu, 2003, 128 p.
30. **Mare Piirsalu.** Substituent, temperature and solvent effects on the alkaline hydrolysis of substituted phenyl and alkyl esters of benzoic acid. Tartu, 2003, 156 p.
31. **Meeri Sassian.** Reactions of partially solvated Grignard reagents. Tartu, 2003, 78 p.
32. **Tarmo Tamm.** Quantum chemical modelling of polypyrrole. Tartu, 2003. 100 p.
33. **Erik Teinemaa.** The environmental fate of the particulate matter and organic pollutants from an oil shale power plant. Tartu, 2003. 102 p.
34. **Jaana Tammiku-Taul.** Quantum chemical study of the properties of Grignard reagents. Tartu, 2003. 120 p.
35. **Andre Lomaka.** Biomedical applications of predictive computational chemistry. Tartu, 2003. 132 p.
36. **Kostyantyn Kirichenko.** Benzotriazole – Mediated Carbon–Carbon Bond Formation. Tartu, 2003. 132 p.
37. **Gunnar Nurk.** Adsorption kinetics of some organic compounds on bismuth single crystal electrodes. Tartu, 2003, 170 p.
38. **Mati Arulepp.** Electrochemical characteristics of porous carbon materials and electrical double layer capacitors. Tartu, 2003, 196 p.
39. **Dan Cornel Fara.** QSPR modeling of complexation and distribution of organic compounds. Tartu, 2004, 126 p.
40. **Riina Mahlapuu.** Signalling of galanin and amyloid precursor protein through adenylate cyclase. Tartu, 2004, 124 p.

41. **Mihkel Kerikmäe.** Some luminescent materials for dosimetric applications and physical research. Tartu, 2004, 143 p.
42. **Jaanus Kruusma.** Determination of some important trace metal ions in human blood. Tartu, 2004, 115 p.
43. **Urmas Johanson.** Investigations of the electrochemical properties of polypyrrole modified electrodes. Tartu, 2004, 91 p.
44. **Kaido Sillar.** Computational study of the acid sites in zeolite ZSM-5. Tartu, 2004, 80 p.
45. **Aldo Oras.** Kinetic aspects of dATPαS interaction with $P2Y_1$ receptor. Tartu, 2004, 75 p.
46. **Erik Mölder.** Measurement of the oxygen mass transfer through the air-water interface. Tartu, 2005, 73 p.
47. **Thomas Thomberg.** The kinetics of electroreduction of peroxodisulfate anion on cadmium (0001) single crystal electrode. Tartu, 2005, 95 p.
48. **Olavi Loog.** Aspects of condensations of carbonyl compounds and their imine analogues. Tartu, 2005, 83 p.
49. **Siim Salmar.** Effect of ultrasound on ester hydrolysis in aqueous ethanol. Tartu, 2006, 73 p.
50. **Ain Uustare.** Modulation of signal transduction of heptahelical receptors by other receptors and G proteins. Tartu, 2006, 121 p.
51. **Sergei Yurchenko.** Determination of some carcinogenic contaminants in food. Tartu, 2006, 143 p.
52. **Kaido Tämm.** QSPR modeling of some properties of organic compounds. Tartu, 2006, 67 p.
53. **Olga Tšubrik.** New methods in the synthesis of multisubstituted hydrazines. Tartu. 2006, 183 p.
54. **Lilli Sooväli.** Spectrophotometric measurements and their uncertainty in chemical analysis and dissociation constant measurements. Tartu, 2006, 125 p.
55. **Eve Koort.** Uncertainty estimation of potentiometrically measured ph and pK_a values. Tartu, 2006, 139 p.
56. **Sergei Kopanchuk.** Regulation of ligand binding to melanocortin receptor subtypes. Tartu, 2006, 119 p.
57. **Silvar Kallip.** Surface structure of some bismuth and antimony single crystal electrodes. Tartu, 2006, 107 p.
58. **Kristjan Saal.** Surface silanization and its application in biomolecule coupling. Tartu, 2006, 77 p.
59. **Tanel Tätte.** High viscosity $Sn(OBu)_4$ oligomeric concentrates and their applications in technology. Tartu, 2006, 91 p.
60. **Dimitar Atanasov Dobchev**. Robust QSAR methods for the prediction of properties from molecular structure. Tartu, 2006, 118 p.
61. **Hannes Hagu**. Impact of ultrasound on hydrophobic interactions in solutions. Tartu, 2007, 81 p.
62. **Rutha Jäger.** Electroreduction of peroxodisulfate anion on bismuth electrodes. Tartu, 2007, 142 p.

63. **Kaido Viht.** Immobilizable bisubstrate-analogue inhibitors of basophilic protein kinases: development and application in biosensors. Tartu, 2007, 88 p.
64. **Eva-Ingrid Rõõm.** Acid-base equilibria in nonpolar media. Tartu, 2007, 156 p.
65. **Sven Tamp.** DFT study of the cesium cation containing complexes relevant to the cesium cation binding by the humic acids. Tartu, 2007, 102 p.
66. **Jaak Nerut.** Electroreduction of hexacyanoferrate(III) anion on Cadmium (0001) single crystal electrode. Tartu, 2007, 180 p.
67. **Lauri Jalukse.** Measurement uncertainty estimation in amperometric dissolved oxygen concentration measurement. Tartu, 2007, 112 p.
68. **Aime Lust.** Charge state of dopants and ordered clusters formation in CaF_2:Mn and CaF_2:Eu luminophors. Tartu, 2007, 100 p.
69. **Iiris Kahn**. Quantitative Structure-Activity Relationships of environmentally relevant properties. Tartu, 2007, 98 p.
70. **Mari Reinik.** Nitrates, nitrites, N-nitrosamines and polycyclic aromatic hydrocarbons in food: analytical methods, occurrence and dietary intake. Tartu, 2007, 172 p.
71. **Heili Kasuk.** Thermodynamic parameters and adsorption kinetics of organic compounds forming the compact adsorption layer at Bi single crystal electrodes. Tartu, 2007, 212 p.
72. **Erki Enkvist.** Synthesis of adenosine-peptide conjugates for biological applications. Tartu, 2007, 114 p.
73. **Svetoslav Hristov Slavov**. Biomedical applications of the QSAR approach. Tartu, 2007, 146 p.
74. **Eneli Härk.** Electroreduction of complex cations on electrochemically polished Bi(*hkl*) single crystal electrodes. Tartu, 2008, 158 p.
75. **Priit Möller.** Electrochemical characteristics of some cathodes for medium temperature solid oxide fuel cells, synthesized by solid state reaction technique. Tartu, 2008, 90 p.
76. **Signe Viggor.** Impact of biochemical parameters of genetically different pseudomonads at the degradation of phenolic compounds. Tartu, 2008, 122 p.
77. **Ave Sarapuu.** Electrochemical reduction of oxygen on quinone-modified carbon electrodes and on thin films of platinum and gold. Tartu, 2008, 134 p.
78. **Agnes Kütt.** Studies of acid-base equilibria in non-aqueous media. Tartu, 2008, 198 p.
79. **Rouvim Kadis.** Evaluation of measurement uncertainty in analytical chemistry: related concepts and some points of misinterpretation. Tartu, 2008, 118 p.
80. **Valter Reedo.** Elaboration of IVB group metal oxide structures and their possible applications. Tartu, 2008, 98 p.
81. **Aleksei Kuznetsov.** Allosteric effects in reactions catalyzed by the cAMP-dependent protein kinase catalytic subunit. Tartu, 2009, 133 p.

82. **Aleksei Bredihhin.** Use of mono- and polyanions in the synthesis of multisubstituted hydrazine derivatives. Tartu, 2009, 105 p.
83. **Anu Ploom.** Quantitative structure-reactivity analysis in organosilicon chemistry. Tartu, 2009, 99 p.
84. **Argo Vonk.** Determination of adenosine A_{2A}- and dopamine D_1 receptor-specific modulation of adenylate cyclase activity in rat striatum. Tartu, 2009, 129 p.
85. **Indrek Kivi.** Synthesis and electrochemical characterization of porous cathode materials for intermediate temperature solid oxide fuel cells. Tartu, 2009, 177 p.
86. **Jaanus Eskusson.** Synthesis and characterisation of diamond-like carbon thin films prepared by pulsed laser deposition method. Tartu, 2009, 117 p.
87. **Marko Lätt.** Carbide derived microporous carbon and electrical double layer capacitors. Tartu, 2009, 107 p.
88. **Vladimir Stepanov.** Slow conformational changes in dopamine transporter interaction with its ligands. Tartu, 2009, 103 p.
89. **Aleksander Trummal.** Computational Study of Structural and Solvent Effects on Acidities of Some Brønsted Acids. Tartu, 2009, 103 p.
90. **Eerold Vellemäe.** Applications of mischmetal in organic synthesis. Tartu, 2009, 93 p.
91. **Sven Parkel.** Ligand binding to 5-HT_{1A} receptors and its regulation by Mg^{2+} and Mn^{2+}. Tartu, 2010, 99 p.
92. **Signe Vahur.** Expanding the possibilities of ATR-FT-IR spectroscopy in determination of inorganic pigments. Tartu, 2010, 184 p.
93. **Tavo Romann**. Preparation and surface modification of bismuth thin film, porous, and microelectrodes. Tartu, 2010, 155 p.
94. **Nadežda Aleksejeva.** Electrocatalytic reduction of oxygen on carbon nanotube-based nanocomposite materials. Tartu, 2010, 147 p.
95. **Marko Kullapere.** Electrochemical properties of glassy carbon, nickel and gold electrodes modified with aryl groups. Tartu, 2010, 233 p.
96. **Liis Siinor.** Adsorption kinetics of ions at Bi single crystal planes from aqueous electrolyte solutions and room-temperature ionic liquids. Tartu, 2010, 101 p.
97. **Angela Vaasa.** Development of fluorescence-based kinetic and binding assays for characterization of protein kinases and their inhibitors. Tartu 2010, 101 p.
98. **Indrek Tulp.** Multivariate analysis of chemical and biological properties. Tartu 2010, 105 p.
99. **Aare Selberg.** Evaluation of environmental quality in Northern Estonia by the analysis of leachate. Tartu 2010, 117 p.
100. **Darja Lavõgina.** Development of protein kinase inhibitors based on adenosine analogue-oligoarginine conjugates. Tartu 2010, 248 p.
101. **Laura Herm.** Biochemistry of dopamine D_2 receptors and its association with motivated behaviour. Tartu 2010, 156 p.

102. **Terje Raudsepp.** Influence of dopant anions on the electrochemical properties of polypyrrole films. Tartu 2010, 112 p.
103. **Margus Marandi.** Electroformation of Polypyrrole Films: *In-situ* AFM and STM Study. Tartu 2011, 116 p.
104. **Kairi Kivirand.** Diamine oxidase-based biosensors: construction and working principles. Tartu, 2011, 140 p.
105. **Anneli Kruve.** Matrix effects in liquid-chromatography electrospray mass-spectrometry. Tartu, 2011, 156 p.
106. **Gary Urb.** Assessment of environmental impact of oil shale fly ash from PF and CFB combustion. Tartu, 2011, 108 p.
107. **Nikita Oskolkov.** A novel strategy for peptide-mediated cellular delivery and induction of endosomal escape. Tartu, 2011, 106 p.
108. **Dana Martin.** The QSPR/QSAR approach for the prediction of properties of fullerene derivatives. Tartu, 2011, 98 p.
109. **Säde Viirlaid.** Novel glutathione analogues and their antioxidant activity. Tartu, 2011, 106 p.
110. **Ülis Sõukand.** Simultaneous adsorption of Cd^{2+}, Ni^{2+}, and Pb^{2+} on peat. Tartu, 2011, 124 p.
111. **Lauri Lipping.** The acidity of strong and superstrong Brønsted acids, an outreach for the "limits of growth": a quantum chemical study. Tartu, 2011, 124 p.
112. **Heisi Kurig.** Electrical double-layer capacitors based on ionic liquids as electrolytes. Tartu, 2011, 146 p.
113. **Marje Kasari.** Bisubstrate luminescent probes, optical sensors and affinity adsorbents for measurement of active protein kinases in biological samples. Tartu, 2012, 126 p.
114. **Kalev Takkis.** Virtual screening of chemical databases for bioactive molecules. Tartu, 2012, 122 p.
115. **Ksenija Kisseljova**. Synthesis of aza-β^3-amino acid containing peptides and kinetic study of their phosphorylation by protein kinase A. Tartu, 2012, 104 p.
116. **Riin Rebane.** Advanced method development strategy for derivatization LC/ESI/MS. Tartu, 2012, 184 p.
117. **Vladislav Ivaništšev.** Double layer structure and adsorption kinetics of ions at metal electrodes in room temperature ionic liquids. Tartu, 2012, 128 p.
118. **Irja Helm.** High accuracy gravimetric Winkler method for determination of dissolved oxygen. Tartu, 2012, 139 p.
119. **Karin Kipper.** Fluoroalcohols as Components of LC-ESI-MS Eluents: Usage and Applications. Tartu, 2012, 164 p.
120. **Arno Ratas.** Energy storage and transfer in dosimetric luminescent materials. Tartu, 2012, 163 p.
121. **Reet Reinart-Okugbeni**. Assay systems for characterisation of subtype-selective binding and functional activity of ligands on dopamine receptors. Tartu, 2012, 159 p.

122. **Lauri Sikk.** Computational study of the Sonogashira cross-coupling reaction. Tartu, 2012, 81 p.
123. **Karita Raudkivi.** Neurochemical studies on inter-individual differences in affect-related behaviour of the laboratory rat. Tartu, 2012, 161 p.
124. **Indrek Saar.** Design of GalR2 subtype specific ligands: their role in depression-like behavior and feeding regulation. Tartu, 2013, 126 p.
125. **Ann Laheäär.** Electrochemical characterization of alkali metal salt based non-aqueous electrolytes for supercapacitors. Tartu, 2013, 127 p.
126. **Kerli Tõnurist.** Influence of electrospun separator materials properties on electrochemical performance of electrical double-layer capacitors. Tartu, 2013, 147 p.
127. **Kaija Põhako-Esko.** Novel organic and inorganic ionogels: preparation and characterization. Tartu, 2013, 124 p.
128. **Ivar Kruusenberg.** Electroreduction of oxygen on carbon nanomaterial-based catalysts. Tartu, 2013, 191 p.
129. **Sander Piiskop.** Kinetic effects of ultrasound in aqueous acetonitrile solutions. Tartu, 2013, 95 p.
130. **Ilona Faustova**. Regulatory role of L-type pyruvate kinase N-terminal domain. Tartu, 2013, 109 p.
131. **Kadi Tamm.** Synthesis and characterization of the micro-mesoporous anode materials and testing of the medium temperature solid oxide fuel cell single cells. Tartu, 2013, 138 p.
132. **Iva Bozhidarova Stoyanova-Slavova.** Validation of QSAR/QSPR for regulatory purposes. Tartu, 2013, 109 p.
133. **Vitali Grozovski**. Adsorption of organic molecules at single crystal electrodes studied by *in situ* STM method. Tartu, 2014, 146 p.
134. **Santa Veikšina**. Development of assay systems for characterisation of ligand binding properties to melanocortin 4 receptors. Tartu, 2014, 151 p.
135. **Jüri Liiv.** PVDF (polyvinylidene difluoride) as material for active element of twisting-ball displays. Tartu, 2014, 111 p.
136. **Kersti Vaarmets.** Electrochemical and physical characterization of pristine and activated molybdenum carbide-derived carbon electrodes for the oxygen electroreduction reaction. Tartu, 2014, 131 p.
137. **Lauri Tõntson**. Regulation of G-protein subtypes by receptors, guanine nucleotides and Mn^{2+}. Tartu, 2014, 105 p.
138. **Aiko Adamson.** Properties of amine-boranes and phosphorus analogues in the gas phase. Tartu, 2014, 78 p.
139. **Elo Kibena**. Electrochemical grafting of glassy carbon, gold, highly oriented pyrolytic graphite and chemical vapour deposition-grown graphene electrodes by diazonium reduction method. Tartu, 2014, 184 p.
140. **Teemu Näykki.** Novel Tools for Water Quality Monitoring – From Field to Laboratory. Tartu, 2014, 202 p.
141. **Karl Kaupmees.** Acidity and basicity in non-aqueous media: importance of solvent properties and purity. Tartu, 2014, 128 p.

142. **Oleg Lebedev**. Hydrazine polyanions: different strategies in the synthesis of heterocycles. Tartu, 2015, 118 p.
143. **Geven Piir.** Environmental risk assessment of chemicals using QSAR methods. Tartu, 2015, 123 p.
144. **Olga Mazina.** Development and application of the biosensor assay for measurements of cyclic adenosine monophosphate in studies of G protein-coupled receptor signalinga. Tartu, 2015, 116 p.
145. **Sandip Ashokrao Kadam.** Anion receptors: synthesis and accurate binding measurements. Tartu, 2015, 116 p.
146. **Indrek Tallo.** Synthesis and characterization of new micro-mesoporous carbide derived carbon materials for high energy and power density electrical double layer capacitors. Tartu, 2015, 148 p.
147. **Heiki Erikson.** Electrochemical reduction of oxygen on nanostructured palladium and gold catalysts. Tartu, 2015, 204 p.
148. **Erik Anderson.** *In situ* Scanning Tunnelling Microscopy studies of the interfacial structure between Bi(111) electrode and a room temperature ionic liquid. Tartu, 2015, 118 p.
149. **Girinath G. Pillai.** Computational Modelling of Diverse Chemical, Biochemical and Biomedical Properties. Tartu, 2015, 140 p.
150. **Piret Pikma.** Interfacial structure and adsorption of organic compounds at Cd(0001) and Sb(111) electrodes from ionic liquid and aqueous electrolytes: an *in situ* STM study. Tartu, 2015, 126 p.
151. **Ganesh babu Manoharan.** Combining chemical and genetic approaches for photoluminescence assays of protein kinases. Tartu, 2016, 126 p.
152. **Carolin Siimenson**. Electrochemical characterization of halide ion adsorption from liquid mixtures at Bi(111) and pyrolytic graphite electrode surface. Tartu, 2016, 110 p.
153. **Asko Laaniste.** Comparison and optimisation of novel mass spectrometry ionisation sources. Tartu, 2016, 156 p.
154. **Hanno Evard.** Estimating limit of detection for mass spectrometric analysis methods. Tartu, 2016, 224 p.
155. **Kadri Ligi.** Characterization and application of protein kinase-responsive organic probes with triplet-singlet energy transfer. Tartu, 2016, 122 p.
156. **Margarita Kagan.** Biosensing penicillins' residues in milk flows. Tartu, 2016, 130 p.
157. **Marie Kriisa.** Development of protein kinase-responsive photoluminescent probes and cellular regulators of protein phosphorylation. Tartu, 2016, 106 p.
158. **Mihkel Vestli.** Ultrasonic spray pyrolysis deposited electrolyte layers for intermediate temperature solid oxide fuel cells. Tartu, 2016, 156 p.
159. **Silver Sepp**. Influence of porosity of the carbide-derived carbon on the properties of the composite electrocatalysts and characteristics of polymer electrolyte fuel cells. Tartu, 2016, 137 p.
160. **Kristjan Haav**. Quantitative relative equilibrium constant measurements in supramolecular chemistry. Tartu, 2017, 158 p.

161. **Anu Teearu**. Development of MALDI-FT-ICR-MS methodology for the analysis of resinous materials. Tartu, 2017, 205 p.
162. **Taavi Ivan**. Bifunctional inhibitors and photoluminescent probes for studies on protein complexes. Tartu, 2017, 140 p.
163. **Maarja-Liisa Oldekop**. Characterization of amino acid derivatization reagents for LC-MS analysis. Tartu, 2017, 147 p.
164. **Kristel Jukk**. Electrochemical reduction of oxygen on platinum- and palladium-based nanocatalysts. Tartu, 2017, 250 p.
165. **Siim Kukk**. Kinetic aspects of interaction between dopamine transporter and *N*-substituted nortropane derivatives. Tartu, 2017, 107 p.
166. **Birgit Viira**. Design and modelling in early drug development in targeting HIV-1 reverse transcriptase and Malaria. Tartu, 2017, 172 p.
167. **Rait Kivi**. Allostery in cAMP dependent protein kinase catalytic subunit. Tartu, 2017, 115 p.
168. **Agnes Heering**. Experimental realization and applications of the unified acidity scale. Tartu, 2017, 123 p.
169. **Delia Juronen**. Biosensing system for the rapid multiplex detection of mastitis-causing pathogens in milk. Tartu, 2018, 85 p.
170. **Hedi Rahnel.** ARC-inhibitors: from reliable biochemical assays to regulators of physiology of cells. Tartu, 2018, 176 p.
171. **Anton Ruzanov.** Computational investigation of the electrical double layer at metal–aqueous solution and metal–ionic liquid interfaces. Tartu, 2018, 129 p.
172. **Katrin Kestav.** Crystal Structure-Guided Development of Bisubstrate-Analogue Inhibitors of Mitotic Protein Kinase Haspin. Tartu, 2018, 166 p.
173. **Mihkel Ilisson.** Synthesis of novel heterocyclic hydrazine derivatives and their conjugates. Tartu, 2018, 101 p.
174. **Anni Allikalt.** Development of assay systems for studying ligand binding to dopamine receptors. Tartu, 2018, 160 p.
175. **Ove Oll.** Electrical double layer structure and energy storage characteristics of ionic liquid based capacitors. Tartu, 2018, 187 p.
176. **Rasmus Palm.** Carbon materials for energy storage applications. Tartu, 2018, 114 p.
177. **Jörgen Metsik.** Preparation and stability of poly(3,4-ethylenedioxythiophene) thin films for transparent electrode applications. Tartu, 2018, 111 p.
178. **Sofja Tšepelevitš.** Experimental studies and modeling of solute-solvent interactions. Tartu, 2018, 109 p.
179. **Märt Lõkov.** Basicity of some nitrogen, phosphorus and carbon bases in acetonitrile. Tartu, 2018, 104 p.
180. **Anton Mastitski**. Preparation of α-aza-amino acid precursors and related compounds by novel methods of reductive one-pot alkylation and direct alkylation. Tartu, 2018, 155 p.
181. **Jürgen Vahter**. Development of bisubstrate inhibitors for protein kinase CK2. Tartu, 2019, 186 p.

182. **Piia Liigand.** Expanding and improving methodology and applications of ionization efficiency measurements. Tartu, 2019, 189 p.
183. **Sigrid Selberg.** Synthesis and properties of lipophilic phosphazene-based indicator molecules. Tartu, 2019, 74 p.
184. **Jaanus Liigand.** Standard substance free quantification for LC/ESI/MS analysis based on the predicted ionization efficiencies. Tartu, 2019, 254 p.
185. **Marek Mooste.** Surface and electrochemical characterisation of aryl film and nanocomposite material modified carbon and metal-based electrodes. Tartu, 2019, 304 p.
186. **Mare Oja.** Experimental investigation and modelling of pH profiles for effective membrane permeability of drug substances. Tartu, 2019, 306 p.
187. **Sajid Hussain.** Electrochemical reduction of oxygen on supported Pt catalysts. Tartu, 2019, 220 p.
188. **Ronald Väli.** Glucose-derived hard carbon electrode materials for sodium-ion batteries. Tartu, 2019, 180 p.
189. **Ester Tee.** Analysis and development of selective synthesis methods of hierarchical micro- and mesoporous carbons. Tartu, 2019, 210 p.
190. **Martin Maide.** Influence of the microstructure and chemical composition of the fuel electrode on the electrochemical performance of reversible solid oxide fuel cell. Tartu, 2020, 144 p.
191. **Edith Viirlaid.** Biosensing Pesticides in Water Samples. Tartu, 2020, 102 p.
192. **Maike Käärik.** Nanoporous carbon: the controlled nanostructure, and structure-property relationships. Tartu, 2020, 162 p.
193. **Artur Gornischeff.** Study of ionization efficiencies for derivatized compounds in LC/ESI/MS and their application for targeted analysis. Tartu, 2020, 124 p.
194. **Reet Link.** Ligand binding, allosteric modulation and constitutive activity of melanocortin-4 receptors. Tartu, 2020, 108 p.
195. **Pilleriin Peets.** Development of instrumental methods for the analysis of textile fibres and dyes. Tartu, 2020, 150 p.
196. **Larisa Ivanova.** Design of active compounds against neurodegenerative diseases. Tartu, 2020, 152 p.
197. **Meelis Härmas.** Impact of activated carbon microstructure and porosity on electrochemical performance of electrical double-layer capacitors. Tartu, 2020, 122 p.
198. **Ruta Hecht.** Novel Eluent Additives for LC-MS Based Bioanalytical Methods. Tartu, 2020, 202 p.
199. **Max Hecht.** Advances in the Development of a Point-of-Care Mass Spectrometer Test. Tartu, 2020, 168 p.
200. **Ida Rahu.** Bromine formation in inorganic bromide/nitrate mixtures and its application for oxidative aromatic bromination. Tartu, 2020, 116 p.
201. **Sander Ratso**. Electrocatalysis of oxygen reduction on non-precious metal catalysts. Tartu, 2020, 371 p.
202. **Astrid Darnell.** Computational design of anion receptors and evaluation of host-guest binding. Tartu, 2021, 150 p.

203. **Ove Korjus.** The development of ceramic fuel electrode for solid oxide cells. Tartu, 2021, 150 p.
204. **Merit Oss.** Ionization efficiency in electrospray ionization source and its relations to compounds' physico-chemical properties. Tartu, 2021, 124 p.
205. **Madis Lüsi**. Electroreduction of oxygen on nanostructured palladium catalysts. Tartu, 2021, 180 p.
206. **Eliise Tammekivi.** Derivatization and quantitative gas-chromatographic analysis of oils. Tartu, 2021, 122 p.
207. **Simona Selberg.** Development of Small-Molecule Regulators of Epi-transcriptomic Processes. Tartu, 2021, 122 p.
208. **Olivier Etebe Nonga.** Inhibitors and photoluminescent probes for in vitro studies on protein kinases PKA and PIM. Tartu, 2021, 189 p.
209. **Riinu Härmas.** The structure and H2 diffusion in porous carbide-derived carbon particles. Tartu, 2022, 123 p.
210. **Maarja Paalo.** Synthesis and characterization of novel carbon electrodes for high power density electrochemical capacitors. Tartu, 2022, 144 p.
211. **Jinfeng Zhao.** Electrochemical characteristics of Bi(hkl) and micro-meso-porous carbon electrodes in ionic liquid based electrolytes. Tartu, 2022, 134 p.
212. **Alar Heinsaar.** Investigation of oxygen electrode materials for high-temperature solid oxide cells in natural conditions. Tartu, 2022, 120 p.
213. **Jaana Lilloja.** Transition metal and nitrogen doped nanocarbon cathode catalysts for anion exchange membrane fuel cells. Tartu, 2022, 202 p.
214. **Maris-Johanna Tahk.** Novel fluorescence-based methods for illuminating transmembrane signal transduction by G-protein coupled receptors. Tartu, 2022, 200 p.
215. **Eerik Jõgi.** Development and Applications of E. coli Immunosensor. Tartu, 2022, 103 p.
216. **Alo Rüütel.** Design principles of synthetic molecular receptors for anion-selective electrodes. Tartu, 2022, 109 p.
217. **Tanel Sõrmus.** Development of stimuli-responsive and covalent bisubstrate inhibitors of protein kinases. Tartu, 2022, 148 p.
218. **Oleg Artemchuk.** Autotrophic nitrogen removal processes for nutrient removal from sidestream and mainstream wastewater. Tartu, 2022, 115 p.
219. **Andre Leesment.** Quantitative studies of Brønsted acidity in biphasic systems and gas-phase. Tartu, 2023, 83 p.
220. **Meeli Arujõe-Sado.** Structural effects in aza-peptide bond formation reaction. Tartu, 2023, 83 p.
221. **Jonas Mart Linge.** Electrochemical reduction of oxygen on silver-based catalysts. Tartu, 2023, 269 p.
222. **Tõnis Laasfeld.** Integrating Image Analysis and Quantitative Modeling for a Holistic View of GPCR Ligand Binding Dynamics. Tartu, 2023, 226 p.
223. **Ernesto de Jesus Zapata Flores.** Derivatization Reagents used in negative mode electrospray LC-MS. Tartu, 2023, 107 p.

224. **Patrick Teppor.** Obtaining platinum-free oxygen reduction catalysts through biomass valorization: a case study of peat. Tartu, 2023, 161 p.
225. **Peeter Valk.** Methanol Oxidation on Platinum-Rare-Earth Metal Oxide Activated Catalysts. Tartu, 2023, 162 p.
226. **Shidong Chen.** Unravelling prehistoric plant exploitation in eastern Baltic: organic residue analysis of plant-based materials by multi-method approach. Tartu, 2023, 245 p.
227. **Yogesh Kumar.** M-N_4 macrocycle-based catalysts for electrocatalysis of oxygen reduction and oxygen evolution. Tartu, 2023, 224 p.
228. **Kerli Martin.** Recognition of carboxylates by synthetic receptors – from structure-affinity studies to solid-contact anion-selective electrode prototyping. Tartu, 2024, 130 p.
229. **Huy Quí Vinh Nguyen.** Development of Carbon Supported Pt–CeO_2 Catalysts for Proton Exchange Membrane Fuel Cells. Tartu, 2024, 198 p.
230. **Heigo Ers**. Adsorption and Structuring Processes at Single Crystal Electrode – Ionic Liquid Interface – Insights from Simulations and *in situ* Studies. Tartu, 2024, 137 p.
231. **Ritums Cepitis.** Modelling Structural and Geometrical Effects in Carbon Dioxide and Oxygen Electrocatalysis. Tartu, 2024, 99 p.
232. **Kaarel Kisand.** Resorcinol-derived carbon-based catalysts for polymer electrolyte fuel cell cathodes. Tartu, 2024, 205 p.
233. **Akmal Kosimov**. Template-assisted Mechanosynthesis (TAMS) for the production of bifunctional transition metal-based catalysts. Tartu, 2024, 123 p.
234. **Larissa Silva Macieli.** Derivatization-targeted LC-MS analysis of compounds containing amino group. Tartu, 2024, 157 p.
235. **Silvester Jürjo.** Separation of rare earth elements from Estonian phosphorite ore using liquid extraction followed by electrochemical reduction. Tartu, 2024, 99 p.
236. **Jan-Michael C. Cayme.** Organic-inorganic interactions in experimental and archaeological ceramics. Tartu, 2025, 156 p.
237. **Miriam Koppel.** The diffusion of H2 adsorbed in carbide-derived carbons: a quasi-elastic neutron scattering study. Tartu, 2025, 138 p.
238. **Kenneth Tuul.** Evaluating lithium-ion pouch cells and hydrogen storage materials under extreme conditions using advanced techniques. Tartu, 2025, 188 p.
239. **Marta-Lisette Pikma.** Exploring the basicity of phosphanes and related compounds. Tartu, 2025, 100 p.
240. **Indrek Saar.** Development of novel on-site chemical analysis tests – from alternative materials and technologies to functional prototypes. Tartu, 2025, 214 p.